Design of Wheelchair Robot for Active Postural Support (WRAPS) for Users with Trunk Impairments

Chawin Ophaswongse

Submitted in partial fulfillment of the
requirements for the degree of
Doctor of Philosophy
under the Executive Committee
of the Graduate School of Arts and Sciences

COLUMBIA UNIVERSITY

2021

Abstract

Design of Wheelchair Robot for Active Postural Support (WRAPS)
for Users with Trunk Impairments

Chawin Ophaswongse

People with severe trunk impairments cannot maintain or control upright posture during sitting or reaching out with the upper body. Passive orthoses are clinically available to support the trunk and promote the use of upper extremities in this population. However, these orthoses only rigidly position the torso on a wheelchair but do not facilitate movement of the trunk.

In this dissertation, we introduce a novel active-assistive torso brace system for upper body movements by a subject while seated. We have named this system as Wheelchair Robot for Active Postural Support (WRAPS). We propose designs of two robots, one for the pelvis and the other for the trunk. Each of the two devices has a parallel chain architecture to accommodate the range of motion (ROM), respectively for the pelvic and thoracic segments. The first thoracic robot was designed for the upper trunk motion relative to the pelvis. It has a 2[RP]S-2UPS architecture which provides four degrees-of-freedom (DOFs) to the end-effector placed on the upper trunk. The second is a pelvic robot which is designed to orient the pelvic segment relative to the seat. It has a 3-DOF [RRR]U-2[RR]S architecture, coupled with translation to accommodate pelvic movements relative to the seat. These robot architectures are synthesized based on human movement data.

WRAPS can modulate the displacement of both the pelvic and the thoracic segments. Additionally, the forces can be applied on the torso through the end-effectors of these robots. Each of the robot prototypes was evaluated with able-bodied subjects to assess the device wearability, kinematic performances, and control system.

Table of Contents

List of Figures

List of Tables

Acknowledgements

Foremost, I would like to express my sincere gratitude to my advisor Prof. Sunil K. Agrawal for his wonderful guidance, motivation, and immense knowledge. It has been my privilege to work with him as a doctoral student. Besides my advisor, I would like to thank my dissertation committee: Dr. Richard Longman, Dr. Yevgeniy Yesilevskiy, Dr. Nicolas Chbat, and Dr. Victoria Lent, MD, for providing valuable inputs that has helped me further improve my dissertation.

I would like to thank every member of the RObotics and Rehabilitation Laboratory (ROAR Lab) and staff in the Mechanical Engineering Department, for all the fun, encouragement, assistance, and support throughout my time in the lab at Columbia University. In addition, I would like to thank all the researchers whose work I was able to build upon in order to continue pushing the frontier of robotics for the benefit of mankind.

I would like to acknowledge with utmost gratitude the support and love from of my family - my parents, Choochai and Luckana, and my younger brothers, Sirawit and Chayapol.

Finally, it is the greatest honor of my life to be the recipient of the Anandamahidol Foundation Doctoral Scholarship, under the Patronage of His Majesty King Bhumibol Adulyadej the Great of Thailand.

Dedication

In Memory of His Majesty King Bhumibol Adulyadej The Great of Thailand,

The Founder of Anandamahidol Foundation Scholarship

To my precious family for their tremendous support and unconditional love

Chapter 1: Introduction

For most people, sitting up independently and performing everyday tasks do not require a second thought. However, for wheelchair users with some severe neurological conditions, most of their day-to-day tasks are extremely challenging, due to their limited trunk control and diminished stability in the seated position. Particularly, this is true for people with spinal cord injury (SCI) in the cervical and high-thoracic regions, and among those with other pathologies such as spina bifida, neuromuscular diseases, or cerebral palsy (CP).

1.1 Trunk Impairments

Postural control is required for typical activity of daily living, including those on wheelchairs. The ability to remain stable in an upright sitting position and return back to this body position after performing a dynamic movement is an essential skill to acquire and maintain for activities of daily living (ADL) [1]. In the seated position, maintaining balance uses a complex array of signals from motor cortex, somatosensory systems, and frontal and parietal areas [2]. However, people with specific neurological disorders (e.g., SCI, CP) lack synergistic control of key postural muscles as well as sensory inputs. This results in poor voluntary trunk control and movement compensation by non-postural muscles [3].

1.1.1 Spinal Cord Injury

According to the National Spinal Cord Injury Statistical Center, the number of people in the U.S. in 2021 living with SCI is estimated to be approximately 296,000 persons, with a range from 252,000 to 373,000 persons. Of those, 59.8%[1] have complete or incomplete injuries to the cervical

[1] https://www.nscisc.uab.edu, data collected since 2015

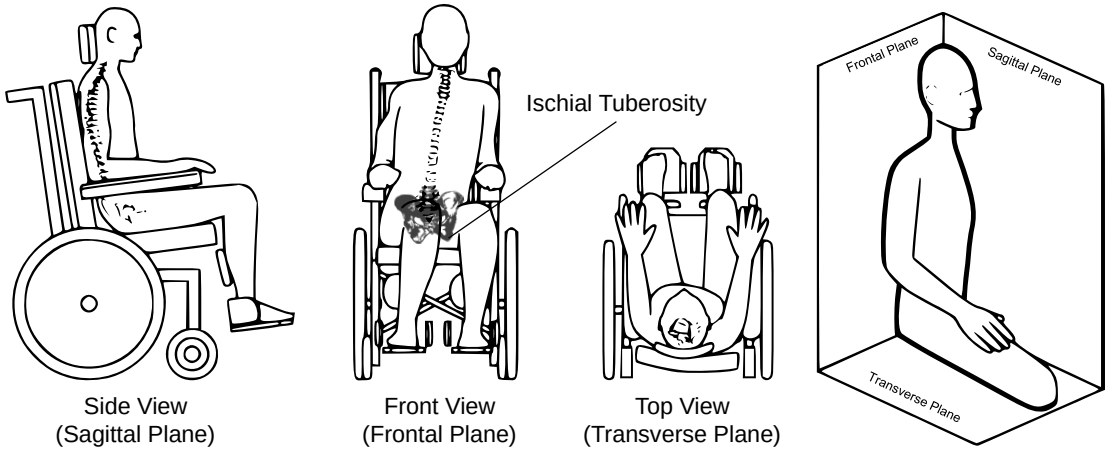

Figure 1.1: Anatomical planes and the ischial tuberosity

spine, which leads to tetraplegia and impaired trunk control [4]. These individuals use a wheelchair as their primary means of mobility and often face difficulties in performing ADL, such as eating, working on a desk, opening a door, and reaching for an object on a shelf or on the floor, due to their limited trunk control and stability in the seated position. Impaired trunk control and muscle spasms also limit their ability to functionally perform upper extremity tasks within arm's distance or beyond maximum arm's extension [5]. Additionally, people with profoundly poor trunk control are always at risk for falling from the wheelchair during reaching and as a result may choose to avoid these activities due to fear of potential injuries [6, 7].

The impaired trunk muscle control and the lack of sensorimotor capacity also greatly limit their ability to perform weight shifts and relieve pressure between the sitting surface and the skin, especially in the area close to ischial tuberosities. People with SCI at level T6 or higher struggle to shift their body weight within their base of support (BOS) to prevent vascular stasis and often develop comorbidities such as pressure ulcers, deep vein thrombosis and life-threatening complications such as autonomic dysreflexia [8]. Upper extremity pain is also a common issue among SCI patients due to overuse of upper limb to compensate for the lack of trunk control during functional activities, including pressure relief maneuvers, transfers, and wheelchair mobility, regardless of patient's age, neurologic level and time since injury [9, 10].

(a) (b) (c)

Figure 1.2: Current technologies for wheelchair users with sitting balance problems: (a) rigid TLSOs, belts, straps, and lateral supports, (b) a tilt wheelchair, and (c) an inflatable cushion.

1.1.2 Cerebral Palsy

Cerebral palsy affects 3.1 per 1000 third graders. Of those affected, 32% have Gross Motor Function Classification System (GMFCS) levels of IV or V, which indicates severely limited self-mobility [11]. Constant leaning on a seat can put the spine at risk for for the development of scoliosis, particularly if the spine is still growing. Children with GMFCS level IV or V have a 50% chance of developing moderate or severe scoliosis[2] by age of 18, whereas children with GMFCS levels of I and II (capable of independent sitting) have almost no risk [12]. The lateral tilt of the pelvis on the seat to one side, or pelvic obliquity, is commonly associated with neuromuscular scoliosis, resulting in asymmetric hip alignment on the seat and imbalanced sitting postures [13]. Consequently, uneven pressure distribution on the ischial tuberosity (shown in Fig. 1.1) also occurs and contributes to pressure sores in this population. To counteract these problems, an assistive device capable of supporting users through a range of seated postures is needed.

1.2 Current Technologies

Current solutions to these sitting balance problems consist of a variety of passive and generally static devices, such as cushions, straps, thoracolumbosacral orthoses (TLSOs), tilt wheelchairs, and inflatable cushions, as shown in Fig. 1.2 (a), (b), and (c) respectively. Cushions help promote

[2]Scoliosis is a spinal deformity condition where the spine has a side curvature. The spine may also rotate or twist in addition to side curving.

good static posture and pressure distribution, but do not provide dynamic assistance and can be difficult to position consistently. Straps can help prevent falling, but also constrain the trunk to only reach within arm's distance, inhibiting reaching and performing functional tasks. TLSOs do not affect the natural history of neuromuscular scoliosis [14], but may make it possible to delay surgery in adolescents. However, they are extremely restrictive and result in muscle atrophy. Furthermore, the workspace surrounding these individuals and their motor flexibility in reaching is highly restricted and their functional independence is substantially compromised as a result. Also, from a rehabilitation standpoint, this situation is not ideal because the person has limited use of the arms within the peripersonal space and limited opportunity to move the trunk further from the BOS.

Wheelchairs with recline and tilt-in-space features can help distribute pressure [15], but do not allow one to lean forward effectively and cannot easily be incorporated into dynamic movements that involve upper extremities and postural control of the trunk. These systems may even have negative impact on breathing and muscle spasms [16]. Cushioning systems are commercially available but dynamic and periodic rotations of the pelvis and the trunk are still essential to prevent development of pressure ulcers regardless of the cushion being used [17, 16, 18, 19]. Caregivers can also assist individuals to shift their posture and center of pressure to prevent vascular-related events, but this can put strain on the caregiver and limit patient independence.

1.3 State of the Art

Since in this dissertation, we focus on assistive devices that support the spinal posture in the sitting position, systems for assisting the upper or lower limbs will not be considered. Other torso exoskeletons designed to facilitate standing will also be excluded since they cannot suit these individual needs. A few proposed assistive systems in the literature were designed to enhance functional independence of the wheelchair users while still maintaining postural stability. In recent years, new passive orthotic systems provide greater range of motion to the upper body while sitting [20, 24], as shown in Fig. 1.3 (a). A dynamic pelvic stabilization device was developed to enhance the posterior and anterior range of motion (ROM) of the pelvis through variable resistance from the

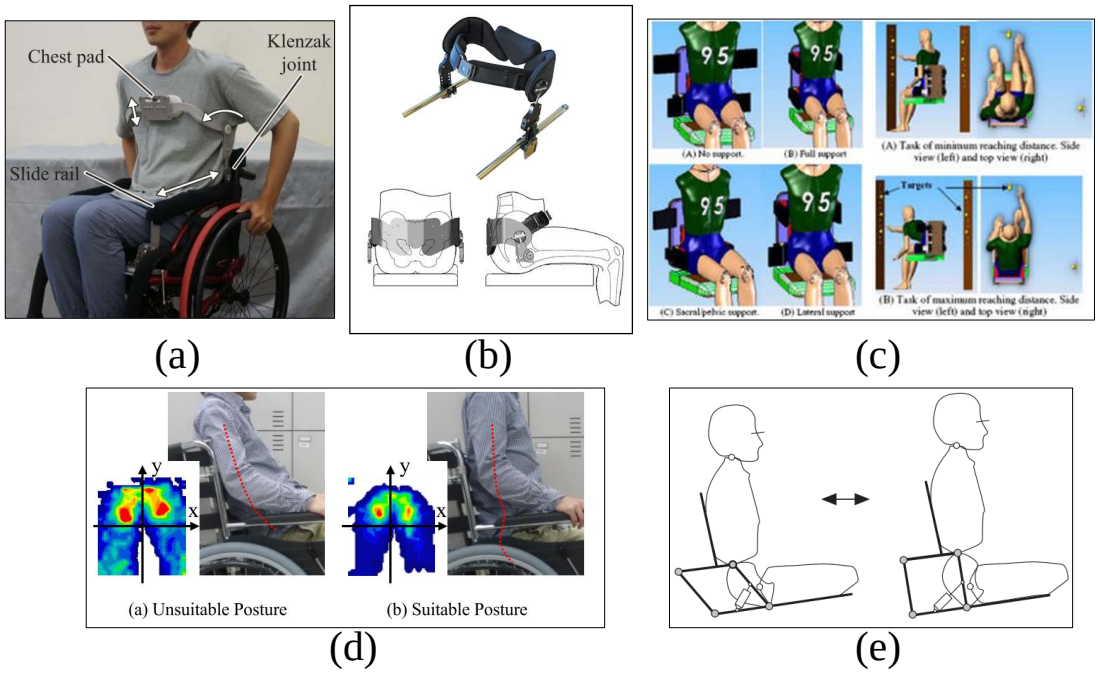

Figure 1.3: State of the art: (a) an assistance device to maintain the user's posture [20], (b) Hip Grip® Pelvic Stabilizer (Body Point, Seattle, WA, USA), (c) Adjustable Lumbar-Pelvic-Thoracic Support System (ALPTS) [21], (d) a depressurization assistance system [22], and (e) a parallelogram that rotates the pelvis on a seat [23].

neutral posture, shown in Fig. 1.3 (b). This device was shown to improve reaching posture of the upper body in SCI patients and children with cerebral palsy (CP) [25, 26]. However, these devices were not designed to actively assist in the control of rotation and translation of the torso during seated functional tasks.

Some active/semi-active postural control devices have also been proposed. Makhsous et al. proposed a system of adjustable ischial and back supports which can reduce ischial-sacral pressure load during sitting while not interfering with reaching performance of wheelchair users with SCI [27, 28]. An Adjustable Lumbar-Pelvic-Thoracic Support System (ALPTS) was also developed to improve reaching stability of wheelchair users with cervical level SCI by user-controlled, flexible air bladders that adjust lateral supports [21], shown in Fig. 1.3 (c). Automated pressure relieving procedures by using air-bladders to periodically adjust contours on the seat were proposed [22, 29], Shown in Fig. 1.3 (d). Additionally, a parallelogram mechanism device was proposed to adjust the

pelvic angle independently from the trunk and the seat support in the sagittal and frontal planes [30, 23], shown in Fig. 1.3 (e). The quasi-statically actuated decoupled pelvis rotations provided by this device has shown to regulate buttlock load in able-bodied individuals. In addition, the postural actuation by this device showed an improvement in cutaneous and subcuteneous tissue oxygenation of individuals with spinal cord disorders [31].

Some novel robotic devices were developed in RObotics And Rehabilitation Laboratory (ROAR Lab) for postural assistance or motor training of the trunk. A cable-driven device called Trunk Support Trainer (TruST) was developed. The system provides an assist-as-needed force strategy to support the trunk during reaching training at and beyond individual's point of stability [32, 33]. This stationary robotic system can expand the active workspace of volitional trunk movements by people with SCI [34]. Robotic Spine Exoskeleton (RoSE) based on a Stewart platform architecture was developed to dynamically control the spinal posture of the upper trunk [35].

However, each of the systems mentioned above is dedicated to only a subset of the capabilities needed by the wheelchair users with neurological degenerative conditions. Combining these devices on the wheelchair may not always be feasible and can additionally cause functional interference. Furthermore, none of the existing devices can accommodate pelvic rotation in all directions and simultaneously adjust the upper trunk posture to modulate the spinal posture on the seat. Some of these devices also require external laboratory instruments to estimate the posture relative to the seat, which is not ideal if the system will be mounted on the wheelchair for future activities. Hence, a single robotic system capable of repositioning the pelvis and/or the trunk in all orientations, estimating the position and rotation of the pelvis relative to the seat in real-time, and addressing most of the postural issues on wheelchair is lacking in the literature.

1.4 Proposed Work and Significance

There is a need for new devices that provide sitting stability, comfort, and functional independence/mobility, while preventing spinal deformities from prolonged static postures on the seat. A new approach to fill this research gap is to design a robotic exoskeleton which simultaneously

addresses all the needs required by wheelchair users with trunk impairment. In order to assist the upper body within and beyond the reachable workspace and regulate pressure between the wheelchair seat and the gluteal area, the system must be capable of estimating the position and orientation of the upper body segments relative to the seat in real-time as well as dynamically re-position the overall spinal posture on the wheelchair.

Here, we describe the first of its kind robotic system named Wheelchair Robot for Active Postural Support (WRAPS). This new exoskeleton is designed to be mounted on a wheelchair or on a bench. The robot will be able to actively assist the torso in order to adjust the spinal posture relative to the seat. Another advantage of robotic systems is that they are equipped with sensors, which allows precise control of the posture and acquisition of biomechanical data for more quantitative clinical assessment and further development of the human-robot interface.

1.5 Outline of the Dissertation

This dissertation is organized as follows: first, we propose a design of the WRAPS for upper trunk motion relative to the pelvis, starting with a mechanism design conceptualization and optimization for kinematic performances. A fabricated hardware prototype is described, and a human experiment conducted with able-bodied subjects is presented. Next, another WRAPS design for pelvis motion on the seat is proposed. Motion capture data of human movement on the seat are mainly used for synthesizing and optimizing its mechanism architecture. A prototype of the pelvic WRAPS is presented along with the results from an evaluation with able-bodied subjects. Finally, we summarize the key contributions, limitations, and future works of the projects in this dissertation.

Chapter 2: WRAPS Design for Upper Trunk Motion

The architecture of the underlying mechanism is a primary design aspect of a robotic system used in a new application. The primary goal of the WRAPS design was to create a device that would aid those with trunk motor impairments in their activities of daily living. Some secondary considerations for this group are: to avoid postures which encourage the progression of scoliosis, to promote deep breathing, to distribute pressure evenly on the skin while sitting, and to keep the device low profile to be compatible with the wheelchair and to avoid social stigma.

2.1 Design Requirements

Activities of daily living were determined through literature review and through user interviews. We interviewed three teenagers with cerebral palsy GMFCS level IV. All of these children wore a rigid TLSO and also used belts in their wheelchair. All three indicated that they wanted to be able to reach further forward and downward without fear of falling, such that they would be able to pet a dog. Other activities included getting things off a shelf independently and changing their resting position independently. We also interviewed an adult with a spinal cord injury, who expressed his wish to change his under-seat pressure distribution more easily and more often to prevent pressure sores.

The requested activities were translated into degrees-of-freedom using a motion capture (Vicon Motion Systems, Oxford, UK) experiment. During this experiment, a single subject would pick up an object from a shelf located in front at four different heights. For retrieving light objects, three degrees-of-freedom in the sagittal plane were sufficient. For heavier objects, a small amount of lateral bending was also employed. Therefore, it was possible to achieve forward reaching tasks with a limited range of motion consisting of four degrees-of-freedom. While lateral bending tasks might

be beneficial to some users, providing the lateral translation and axial rotation degree-of-freedoms would create a greater stability challenge, and could encourage a prolonged unhealthy sitting posture that may promote the progression of a scoliotic spine, i.e., with twisting and leaning on one side. Limiting the degrees-of-freedom could also potentially make the device simpler and less obtrusive, leading to wider social acceptance.

2.2 Mechanism Design for Pelvic-Thoracic Segment

2.2.1 Proposed Architecture

The mechanism design, shown in Fig. 2.1, was chosen to achieve the desired degrees-of-freedom while meeting the unique needs of this group [36]. The two brace design provides necessary support at the pelvis and thorax without restricting breathing from the belly. The two braces fit around the torso. The base brace shown (pelvic brace) rests just above the iliac crests of the wearer and the top brace shown (thoracic brace) would be at sternum level. To make the device low-profile, a parallel mechanism was preferred in comparison to a serial mechanism. The legs of the parallel mechanism can be placed around the body, while a serial chain could cause interference with the wheelchair.

The platforms are connected with two planar Rotational-Prismatic-Spherical ([RP]S) and two Universal-Prismatic-Spherical (UPS) kinematic chains to achieve the four desired DOF [37, 38]. The two [RP]S limbs are located in the sagittal plane, with the revolute (R) joints connected to the pelvic brace and the spherical (S) joints connected to the thoracic brace. The UPS limbs are located outside the sagittal plane, with the universal (U) joints connected to the pelvic brace and the S joints connecting to the thoracic brace. All four prismatic (P) joints are actuated. By orienting the axes of the R joints perpendicular to the sagittal plane, lateral translation and axial rotation are prevented. The end-effector has four remaining degrees-of-freedom and is fully actuated.

2.2.2 Joint Placement Optimization

The range of motion and the force capability of a parallel mechanism are very sensitive to the joint placement. Hence, an optimization was needed to maximize the force capability and the torso

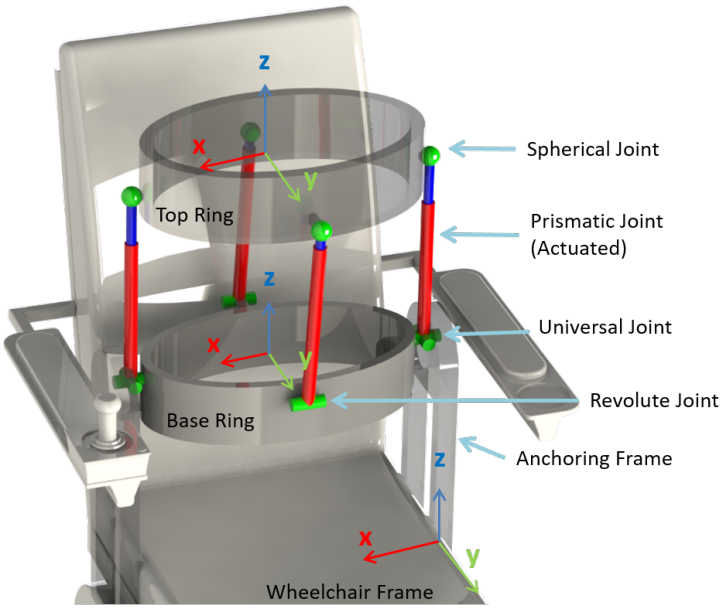

Figure 2.1: 2[RP]S-2UPS schematic

range of motion in the sagittal plane. To simplify the optimization routine, the spatial parallel mechanism can be seen as a planar 3-RPR mechanism in the sagittal plane as shown in Fig. 2.2, given that the universal joint positions are symmetrically placed along the sagittal plane. Note that in this design, there are no singularities of the the rotation around the y-axis.

The torso was modeled as an inverted pendulum with the center of mass at the endpoint. The torso was assumed to bear all axial load from the weight. As the device is intended for use by individuals with torso motor impairments, it is expected that the dominant force on the WRAPS will be the weight of the user's torso, rather than user-generated force. In addition, given that the device is intended for those with substantial motor impairments, it is meant to provide slow, smooth movements rather than rapid, jerky ones, so a quasi-static analysis of the force is appropriate. The torso was modeled as an inverted pendulum with a pivot at the pelvis, shown in Fig. 2.4. The torso is considered a rigid link and is assumed to bear all of the axial load from its weight. It was assigned a mass of 50 kg and a COM height of 0.25 m, following ISO 7176-11 standard for a 75 kg wheelchair rider. The maximum bending degree was determined to be approximately 1 radian [20]. The optimization is based on the Generalized Pattern Search Algorithm (GPSA) [39]. The

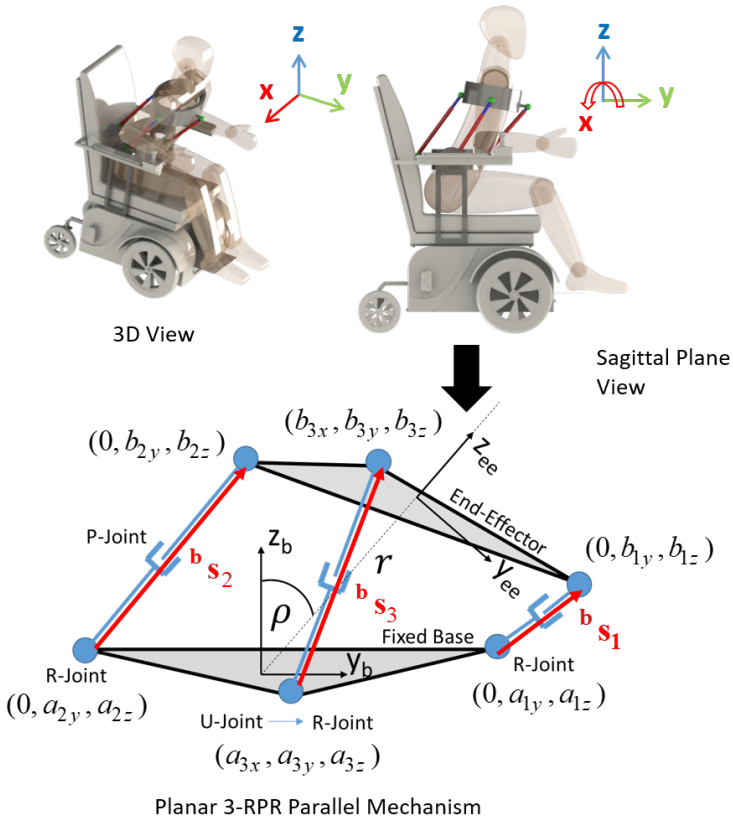

Figure 2.2: Model of a 2[RP]S-2UPS mechanism simplified to planar a 3-RPR mechanism in the sagittal plane

algorithm is implemented with the MATLAB® Genetic Algorithm and Direct Search Toolbox. This optimization method does not require a gradient. Thus, it can be used with functions that are not continuous or differentiable.

Fig. 2.2 shows the 12 parameters to be optimized: $(a_{iy}, a_{iz}, b_{iy}, b_{iz},\ i = 1, 2, 3)$, which are the R, U, and S joint locations in the sagittal plane. In this case, $a_{1x} = a_{2x} = b_{1x} = b_{2x} = 0$ because the anterior and posterior limbs are in the sagittal plane and a_{3x}, b_{3x} are constant because of the width of the torso. Further constraints resulting from the length and stroke of candidate linear actuators are shown in Tab. 2.1.

First, we normalized these parameters to the same scale. For example, $a_{1y} \in [a_{1y}^{min}, a_{1y}^{max}]$ is converted to $\eta_1 \in [0, 12]$. The acceptable ranges for these parameters are based on the dimensions of the torso and the acceptable amount of offset from the body. They are shown in Tab. 2.2. Then,

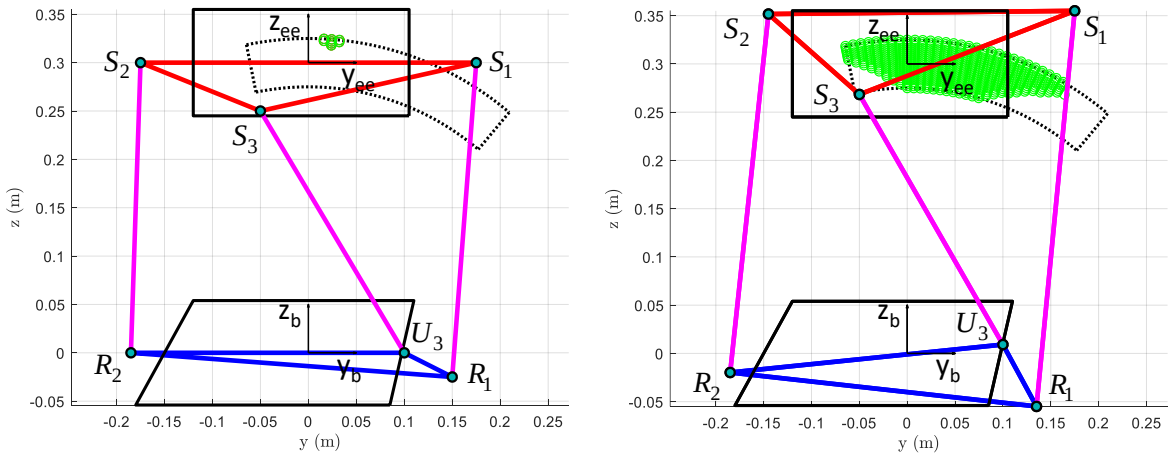

(a) $F(\boldsymbol{\eta}) = 0.9914$ (b) $F(\boldsymbol{\eta}) = 0.2757$

Figure 2.3: Comparison between the fitness function values of the initial set of parameter (a) and the final solution (b)

Table 2.1: Optimization parameters

Workspace		Constraints	
r	[0.275, 0.325] m	$\left\|{}^{b}\hat{\mathbf{s}}_1\right\|$	[0.332, 0.472] m
Δr	0.0020833 m	$\left\|{}^{b}\hat{\mathbf{s}}_2\right\|$	[0.332, 0.472] m
ρ	[-0.2, 0.7] rad	$\left\|{}^{b}\hat{\mathbf{s}}_3\right\|$	[0.244, 0.344] m
$\Delta\rho$	0.025 rad	κ_{max}	8
N_{sample}	925	a_{3x}, b_{3x}	0.2 m

all 12 normalized parameters η_i are used to calculate a fitness value of a set of input parameters. The fitness function $F(\boldsymbol{\eta})$ is evaluated in the following steps:

1. The algorithm samples a configuration of the end-effector in polar coordinates in the sagittal plane (ρ, r) approximating the forward/backward bending motion of the torso. The parameters of the workspace sample are given in Tab. 2.1.

2. The vectors of three limb lengths are calculated based on the current end-effector orientation

Table 2.2: Optimization results of joint positions

Base	Range (m)	Initial Guess (m)	Optimized (m)
a_{1y}	[0.135, 0.2]	0.15	0.1351
a_{1z}	[-0.055, 0.055]	-0.025	-0.0549
a_{2y}	[-0.225, -0.185]	-0.185	-0.185
a_{2z}	[-0.055, 0.1]	0	-0.0198
a_{3y}	[-0.15, 0.1]	0.1	0.1
a_{3z}	[-0.055, 0.055]	0	0.0092

End-Effector	Range (m)	Initial Guess (m)	Optimized (m)
b_{1y}	[0.115, 0.175]	0.175	0.175
b_{1z}	[-0.055, 0.055]	0	0.055
b_{2y}	[-0.175, 0.130]	-0.175	-0.145
b_{2z}	[-0.1, 0.055]	0	0.0517
b_{3y}	[-0.1, 0.1]	-0.05	-0.05
b_{3z}	[-0.055, 0.055]	-0.05	-0.0317

with respect to the base frame, namely

$$ {}^{b}\mathbf{s}_i = \begin{bmatrix} s_{ix} \\ s_{iy} \\ s_{iz} \end{bmatrix} = \begin{bmatrix} b_{ix} - a_{ix} \\ -a_{iy} + b_{iy}\cos\rho + (b_{iz} + r)\sin\rho \\ -a_{iz} + (b_{iz} + r)\cos\rho - b_{iy}\sin\rho \end{bmatrix} \tag{2.1} $$

3. The dimensionally homogeneous Jacobian, $\tilde{\mathbf{J}}$, modified from the Jacobian mapping between the joint forces to the end-effector wrench of the equivalent 3-R$\underline{\text{P}}$R mechanism in the sagittal plane, is calculated as follows [40, 41]:

$$ \tilde{\mathbf{J}} = \begin{bmatrix} {}^{b}\mathbf{w}_1 & {}^{b}\mathbf{w}_2 & {}^{b}\mathbf{w}_3 \end{bmatrix}_{3\times 3} \tag{2.2} $$

where ${}^{b}\mathbf{w}_i = \begin{bmatrix} \frac{1}{L}w_{ix} & \hat{s}_{iy} & \hat{s}_{iz} \end{bmatrix}^T$, $L = \sqrt{\frac{1}{3}\sum_{i=1}^{3}|w_{ix}|^2}$ (characteristic length),
$w_{ix} = (b_{iy}\cos\rho - b_{iz}\cos\rho)\hat{s}_{iy} - (b_{iy}\sin\rho + b_{iz}\cos\rho)\hat{s}_{iz}$,

$\hat{s}_{iy} = \frac{s_{iy}}{\sqrt{s_{iy}^2+s_{iz}^2}}$, $\hat{s}_{iz} = \frac{s_{iz}}{\sqrt{s_{iy}^2+s_{iz}^2}}$, and ${}^b\hat{\mathbf{s}}_i = \frac{{}^b\hat{\mathbf{s}}_i}{\left\|{}^b\hat{\mathbf{s}}_i\right\|} = \begin{bmatrix} \hat{s}_{ix} & \hat{s}_{iy} & \hat{s}_{iz} \end{bmatrix}^T$.

4. Each sampled point is tested by two conditions. First, all required limb lengths must be feasible. The allowable range on each limb is determined by the stroke length of the linear actuator and dimensions in CAD. The condition is

$$\left\|{}^b\hat{\mathbf{s}}_i\right\| \in \left[{s_i}^{\min}, {s_i}^{\max}\right], i = 1, 2, 3 \tag{2.3}$$

The second condition is that the condition number (κ) of the Jacobian $\tilde{\mathbf{J}}$ is less than a specified value to avoid singularities, namely

$$\kappa(\tilde{\mathbf{J}}) = \frac{\sigma_{\max}(\tilde{\mathbf{J}})}{\sigma_{\min}(\tilde{\mathbf{J}})} < \kappa_{max} \tag{2.4}$$

where $\sigma_{\max}(\tilde{\mathbf{J}})$ and $\sigma_{\min}(\tilde{\mathbf{J}})$ are maximal and minimal singular values of the matrix $\tilde{\mathbf{J}}$, respectively. If both of the conditions in Eqn. (2.3) and (2.4) are met, the current sampled point will be marked as feasible.

5. Once the algorithm has gone through all points in the workspace, the fitness function output is

$$F(\eta) = 1 - \frac{N_{feasible}}{N_{sample}} \tag{2.5}$$

where $N_{feasible}$ and N_{sample} are the number of all feasible points in the workspace and the total number of points in sampled workspace respectively.

The optimization results are shown in Tab. 2.2 and illustrated in Fig. 2.3. The initial set of joint position parameters in Fig. 2.3 (a) provides only a small number of feasible points in the sampled workspace, enclosed by dotted lines. The GPSA algorithm outputs an optimized set of joint positions in Fig. 2.3 (b) with a significantly higher number of feasible points.

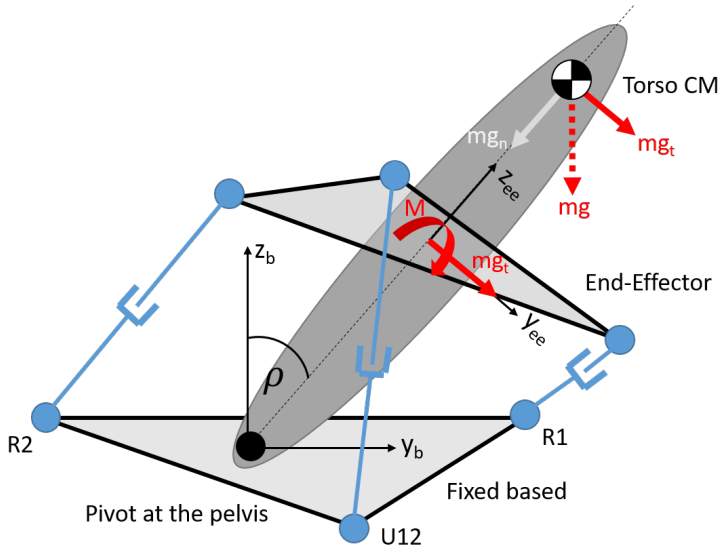

Figure 2.4: Forces applied to WRAPS by the torso weight

Joint Force Requirements

After the joint positions had been optimized to provide the desired workspace, the required joint forces were determined. In the most extreme flexion position, the forces in the prismatic joints are 133.95 N on the front limb ([RP]S 1), 253.82 N on the back limb ([RP]S 2), and 230.81 N in the two side limbs (UPS). The gear ratio of the linear actuators were selected based on this specification.

2.3 Mathematical Models

The kinematic diagram of the 2[RP]S-2UPS parallel mechanism is shown in Fig. 2.5. The line formed by the centers of the two revolute joints (R_1 and R_2) and the origin of the fixed base coordinate frame $\{O_b\}$ is selected to be the sagittal plane (y_b-z_b plane). The origin of a coordinate frame $\{O_s\}$ on the end-effector is inside the line connecting the centers of the two spherical joints (S_1 and S_2) of the two [RP]S limbs. Since the revolute joints constrain the line S_1S_2 in the sagittal plane, the y_s axis that is parallel to this line is also kept in the the sagittal plane. $\mathbf{a}_i$ are the vectors of joint positions with respect to the base frame, while $\mathbf{b}_i$ are the vectors of the spherical joint positions with respect to the local frame $\{O_s\}$.

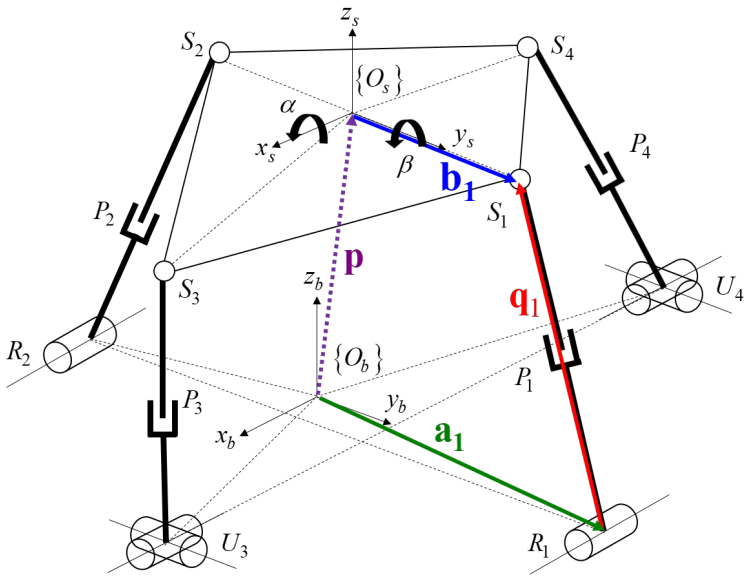

Figure 2.5: Kinematic diagram of a 2[RP]S-2UPS parallel actuated platform

2.3.1 Inverse Kinematics

A configuration of the robot is determined by a set of four variables (y, z, α, β). The variables y and z are the origin position of the end-effector frame $\{O_s\}$ relative to the origin of the base frame $\{O_b\}$ and α and β are the Euler angles in the current X-Y sequence.

Given the position and orientation of the end-effector frame $\{O_s\}$ relative to the base frame $\{O_b\}$, we have to find the required four limb lengths to achieve this configuration. The commanded position and orientation from the four input variables (y, z, α, β) can be transformed into all four limb lengths q_i $(i = 1, 2, 3, 4)$ by using the close-loop kinematic constraints as shown in Fig. 2.5:

$$\begin{aligned} \mathbf{q}_i &= \mathbf{p} + \mathbf{R}\mathbf{b}_i - \mathbf{a}_i \quad (i = 1, 2, 3, 4) \\ q_i &= \|\mathbf{q}_i\| = \left[(\mathbf{p} + \mathbf{R}\mathbf{b}_i - \mathbf{a}_i)^T (\mathbf{p} + \mathbf{R}\mathbf{b}_i - \mathbf{a}_i)\right]^{1/2} \end{aligned} \tag{2.6}$$

where $\mathbf{p} = [0, y, z]^T$, $\mathbf{R} = \begin{bmatrix} c\beta & 0 & s\beta \\ s\alpha s\beta & c\alpha & -s\alpha c\beta \\ -c\alpha s\beta & s\alpha & c\alpha c\beta \end{bmatrix}$, $(s\theta := \sin\theta;\ c\theta := \cos\theta)$.

2.3.2 Forward Kinematics

An analytical solution to the forward kinematics has been found for a special case of this 2[RP]S-2UPS structure in which the joints on each platform lie in the same plane [38]. Thus, we use the Newton-Raphson algorithm to calculate the iterative solution from a given set of limb lengths [42]. The Newton-Raphson formula in the vector form is

$$\mathbf{X}_{n+1} = \mathbf{X}_n + \mathbf{J}_f^{-1}(\mathbf{X}_n)\mathbf{d}_n \tag{2.7}$$

where $\mathbf{X} = \begin{bmatrix} x & y & \alpha & \beta \end{bmatrix}^T$, and subscript n denotes the solution at iteration step n, and $\mathbf{d}_n$ is a vector consisting of $d_{n,i} = -f_i(\mathbf{X}_n),\ i = 1, 2, 3, 4$. The scalar function f_i is derived from Eqn. (2.6):

$$f_i(\mathbf{X}_n) = (\mathbf{p} + \mathbf{R}\mathbf{b}_i - \mathbf{a}_i)^T(\mathbf{p} + \mathbf{R}\mathbf{b}_i - \mathbf{a}_i) - {q_i}^2 = 0. \tag{2.8}$$

The forward kinematics by the Newton-Raphson algorithm is described in Algorithm 1. The solution $\mathbf{X}_n$ is used as the initial guess in the next time step, when we obtain a new set of limb lengths q_i, to reduce the computational time and obtain continuous solutions. The first time step uses the neutral configuration as the initial guess. The derivation of iterative Newton-Raphson Jacobian $\mathbf{J}_f$ of the robot is in Appendix A.

2.3.3 Kinematics of an Arbitrary End-Effector Frame

In Sections 2.3.1 and 2.3.2, we used an end-effector coordinate frame $\{O_s\}$ that is properly aligned within the robot architecture such that position and orientation of the frame in 3D space can be described by exactly four independent variables (y, z, α, β). However, in real implementations, the prescribed end-effector frame $\{O_{ee}\}$, which is the position of the upper trunk from the optimization in Section 2.2.2, has an arbitrary offset of both position and orientation from the frame $\{O_s\}$ in the local y_s-z_s plane. Nevertheless, we can employ homogeneous transformation matrices to find the position and orientation of the actual end-effector frame in terms of the four variables (y, z, α, β) obtained from the forward kinematics solution, as shown in Fig. 2.6.

Algorithm 1: Forward kinematics Newton-Raphson algorithm

Input: $n_{max} \geq 1$, $\varepsilon_b > 0$: tolerance sum of $\left|d_{n,i}\right|$, and $\varepsilon_x > 0$: tolerance size of $\delta\mathbf{X}_n$
Output: $\mathbf{X}_n$
$n \leftarrow 1$;
$\mathbf{X}_n \leftarrow$ initial guess;
while $n \leq n_{max}$ **do**
  Compute the Newton-Raphson Jacobian $\mathbf{J}_f(\mathbf{X}_n)$ (see Appendix A);
  Compute the vector $\mathbf{d}_n$ from scalar functions in (2.8);
  if $\sum_{i=1}^{4}\left|d_{n,i}\right| < \varepsilon_b$ **then**
    Break and return $\mathbf{X}_n$ as the solution;
  else
    $\delta\mathbf{X}_n \leftarrow \mathbf{J}_f^{-1}(\mathbf{X}_n)\mathbf{d}_n$;
    if $\|\delta\mathbf{X}_n\| < \varepsilon_x$ **then**
      Break and return $\mathbf{X}_n$ as the solution;
    else
      $\mathbf{X}_{n+1} \leftarrow \mathbf{X}_n + \delta\mathbf{X}_n$;
      $n \leftarrow n + 1$;
    end
  end
end

We know the local transformation matrix from the end-effector frame $\{O_{ee}\}$ to frame $\{O_s\}$. For simplicity, we can define the origin of the frame $\{O_s\}$ to be always coincide with the center of the spherical joint S_1, and thus we get a transformation matrix in terms of the parameters obtained from the optimization, namely

$$ {}^{ee}\mathbf{T}_s = \left[\begin{array}{ccc|c} 1 & 0 & 0 & 0 \\ 0 & c\psi_s & -s\psi_s & b_{1y} \\ 0 & s\psi_s & c\psi_s & b_{1z} \\ \hline 0 & 0 & 0 & 1 \end{array}\right] \tag{2.9} $$

where $\psi_s = \arctan 2(\Delta z_{ee}, \Delta y_{ee}) = \arctan 2(b_{1z} - b_{2z}, b_{1y} - b_{2y})$.

The transformation matrix from the base frame $\{O_b\}$ to the frame $\{O_s\}$ which is defined by

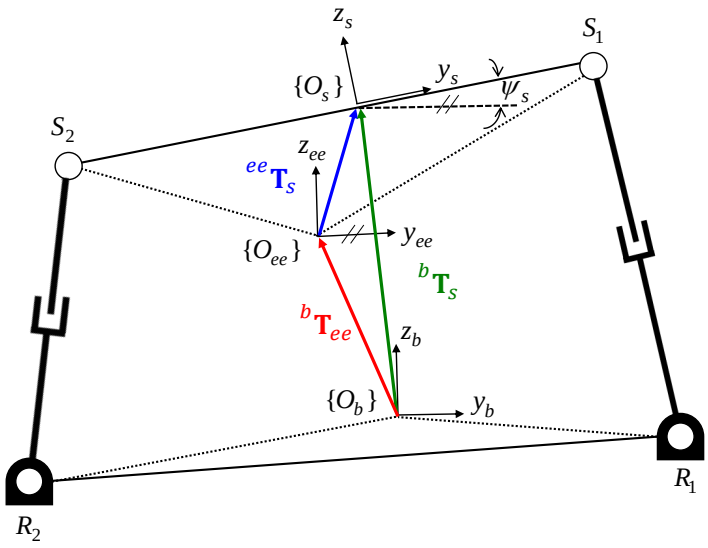

Figure 2.6: Transformations between coordinate frames in sagittal plane

four variables (y, z, α, β) is

$$ {}^{b}\mathbf{T}_s = \left[\begin{array}{ccc|c} c\beta & 0 & s\beta & 0 \\ s\alpha s\beta & c\alpha & -s\alpha c\beta & y \\ -c\alpha s\beta & s\alpha & c\alpha c\beta & z \\ \hline 0 & 0 & 0 & 1 \end{array}\right]. \tag{2.10} $$

Hence, the transformation matrix from the base coordinate frame $\{O_b\}$ to the actual end-effector frame $\{O_{ee}\}$ using Eqn. (2.9) and (2.10) is

$$ \begin{aligned} {}^{b}\mathbf{T}_{ee} &= {}^{b}\mathbf{T}_s \, {}^{ee}\mathbf{T}_s{}^{-1} \\ &= \left[\begin{array}{ccc|c} c\beta & -s\psi_s s\beta & c\psi_s s\beta & Z_s s\beta \\ s\alpha s\beta & u_{22} & u_{23} & y + Y_s c\alpha - Z_s s\alpha c\beta \\ -c\alpha s\beta & u_{32} & u_{33} & z + Y_s s\alpha + Z_s c\alpha c\beta \\ \hline 0 & 0 & 0 & 1 \end{array}\right] \end{aligned} \tag{2.11} $$

where $u_{22} = c\psi_s c\alpha + s\psi_s s\alpha c\beta$, $u_{23} = s\psi_s c\alpha - c\psi_s s\alpha c\beta$, $u_{32} = c\psi_s s\alpha - s\psi_s c\alpha c\beta$, $u_{33} = s\psi_s s\alpha + c\psi_s c\alpha c\beta$, $Y_s = -b_{1y} c\psi_s - b_{1z} s\psi_s$, and $Z_s = b_{1y} s\psi_s - b_{1z} c\psi_s$.

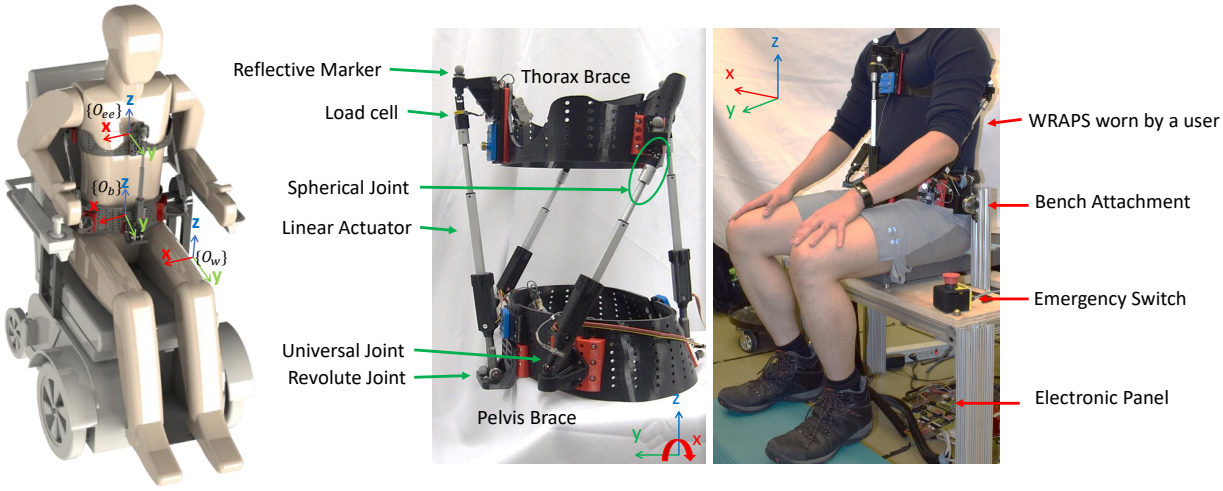

Figure 2.7: CAD design of WRAPS mounted on wheelchair and the real prototype

2.3.4 Output Force and Moment

The forces and moments in six degrees-of-freedom $\mathbf{W}$ at the origin of the end-effector with respect to the base frame can be calculated from the vector of joint forces $\mathbf{f}$ as follows

$$\mathbf{W} = \mathbf{J}_s^T \mathbf{f} \tag{2.12}$$

where $\mathbf{J}_s$ is the screw-based velocity Jacobian, derived by taking the orthogonal product of each selected reciprocal screw and the instantaneous twist of its respective limb. The selected reciprocal screw is reciprocal to all passive joint screws in the instantaneous twist equation, except for its respective actuated joint screw [43]. For a 2[RP]S-2UPS mechanism, the Jacobian is in the following form [38]:

$$\mathbf{J}_s = \begin{bmatrix} \hat{\mathbf{q}}_1^T & (\mathbf{R}\mathbf{b}_1 \times \hat{\mathbf{q}}_1)^T \\ \vdots & \vdots \\ \hat{\mathbf{q}}_4^T & (\mathbf{R}\mathbf{b}_4 \times \hat{\mathbf{q}}_4)^T \\ \hat{\mathbf{x}}^T & (\mathbf{R}\mathbf{b}_1 \times \hat{\mathbf{x}})^T \\ \hat{\mathbf{x}}^T & (\mathbf{R}\mathbf{b}_2 \times \hat{\mathbf{x}})^T \end{bmatrix}_{6\times 6} \tag{2.13}$$

where $\hat{\mathbf{x}} = \begin{bmatrix} 1 & 0 & 0 \end{bmatrix}^T$.

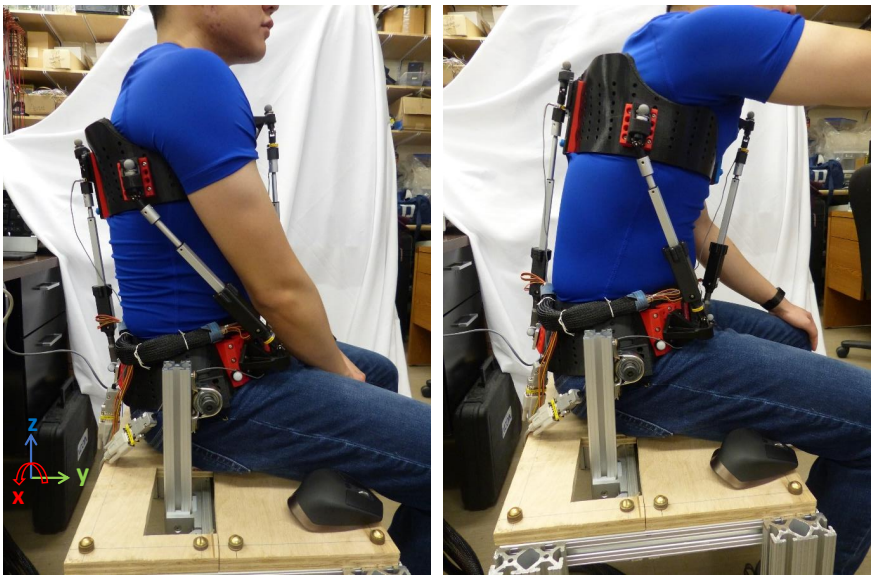

Figure 2.8: Subject wearing the WRAPS with a forward reaching movement

From the Jacobian, one can easily observe that the forces and the moments in the sagittal plane (f_y, f_z, m_x) are fully determined by the forces measured from the four load cells along the limbs throughout the workspace of the end-effector, while the other components of forces and moments need to be calculated from the unmeasured constraint forces along the revolute joint axes. Hence, the force measurement will be collected only in the sagittal plane components, and the dimension of the Jacobian transpose $\mathbf{J}_s^T$ can be reduced to 3×4.

2.4 Hardware Realization

A prototype of the device was created for evaluation, as shown in Fig. 2.7. The two braces were designed from a body scan of a healthy adult male and were made of 3D-printed ABS plastic (Fortus 360mc, Stratasys, Eden Prairie, MN, USA). The braces have adjustable width and are lined with a soft foam padding (Rolyan Polycushion Padding Sheet, Performance Health, Warrenville, IL, USA) to distribute pressure and improve wearer comfort. The device is actuated by Actuonix Micro-linear actuators (L16-100-150-12-P in the UPS limbs and L16-140-150-12-P in the [RP]S limbs, Actuonix Motion Devices, Victoria, BC, Canada). The motors have a 100 mm and 140

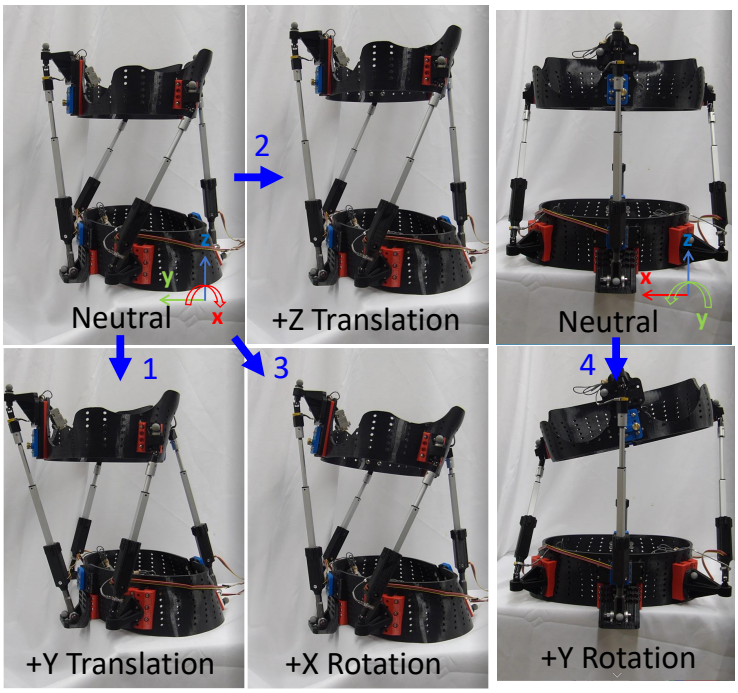

Figure 2.9: Motion in each of the four degrees-of-freedom

mm stroke, respectively, and their maximum force is 250 N. They are driven at 12 V using a 1000 Hz PWM signal through a small driver (TB6612FNG, Toshiba, Minato, Tokyo, Japan). These motors contain an on-board potentiometer, and are placed in series with a load cell (LCM 200 Miniature Tension and Compression Load Cell with IAA100 Analog Amplifier with Voltage Output, FUTEK, Irvine, CA, USA). The signals from these sensors are multiplexed and sent to a portable reconfigurable I/O (RIO) device (myRIO-1900, National Instruments, Austin, TX, USA) as a control board. The command is sent from a user interface of a LabVIEW™ software (version 2017, National Instruments, Austin, TX, USA) in a host computer connected to the control board either through the Wi-Fi or a USB cable. The pelvic ring is attached to a custom-made bench by two bearings so that this rotation will accommodate the pelvic tilt during sitting. Alternatively, the bearing shaft can be rigidly fixed relative to the bench in any angle, as needed during experimentation, as shown in Fig. 2.8. Also, the independent motion in each of the four DOFs is shown in Fig. 2.9.

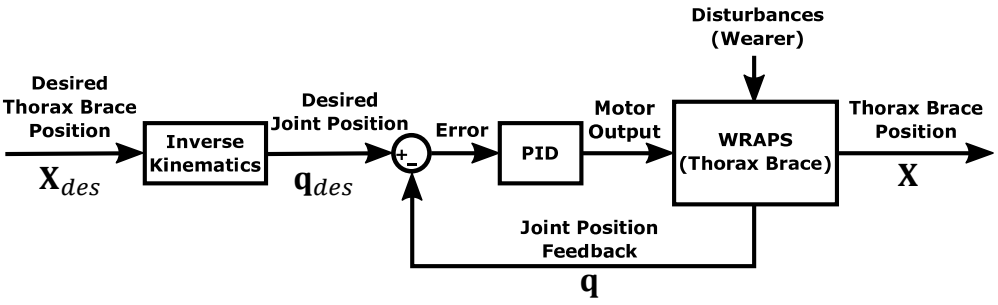

Figure 2.10: Position control mode

2.5 System Evaluation

The performance of the device has been evaluated against reference systems in terms of the accuracy of the forward kinematics algorithm, the force-moment output calculated from the forces along the limbs, and the capability to support the torso.

2.5.1 Forward Kinematics Validation

The forward kinematics of the device was validated using a motion-capture camera system (Bonita, Vicon Motion Systems, Oxford, UK). The robot configuration is controlled in the position mode as shown in Fig. 2.10. The actual position and orientation of the end-effector is calculated using the four variables (y, z, α, β) obtained from solutions of forward kinematics according to Sections 2.3.2 and 2.3.3. The accuracy of the forward kinematics is shown in Figs. 2.11 and 2.12.

In Fig. 2.11, the device was commanded to rotate about the x-axis and move forward and down in a flexion/extension motion. The mean absolute error (MAE) of rotation about the x-axis, which was the primary direction of motion, was 1.08 degrees. The maximum MAE was 3.80 mm in the z direction, and the maximum MAE error in rotation was 3.28 degrees about the y-axis.

In Fig. 2.12, the device moved in a complex motion that combined all four degrees-of-freedom. The maximum RMS translation error was 3.96 in the z direction and the maximum RMS rotational error was 2.55 degrees about y. For all directions, the translation error was within 4 mm and the rotational error was within 3 degrees. The degrees-of-freedom with the largest errors were translation in z and the rotation about y.

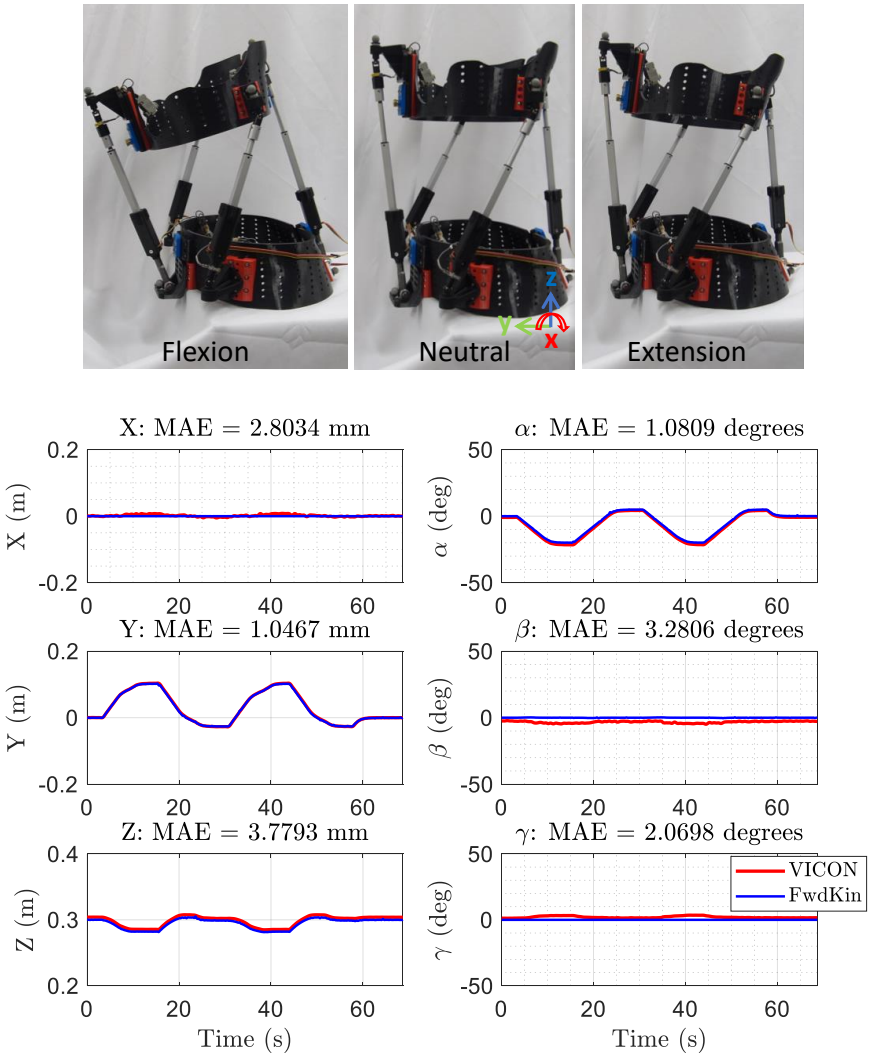

Figure 2.11: Flexion-Extension motion (rotation about x, with translation in y and z)

The error is due in part to manufacturing, including motion from imprecise joint tolerance and an initial angular offset between the braces. The initial offset of the top brace relative to the pelvis brace is not zero in some DOFs, which causes the position measured from the motion capture system to show the initial offset error relative to the forward kinematic solution. Nevertheless, the predominant errors are from these initial offsets, and the problem can be easily fixed in the hardware.

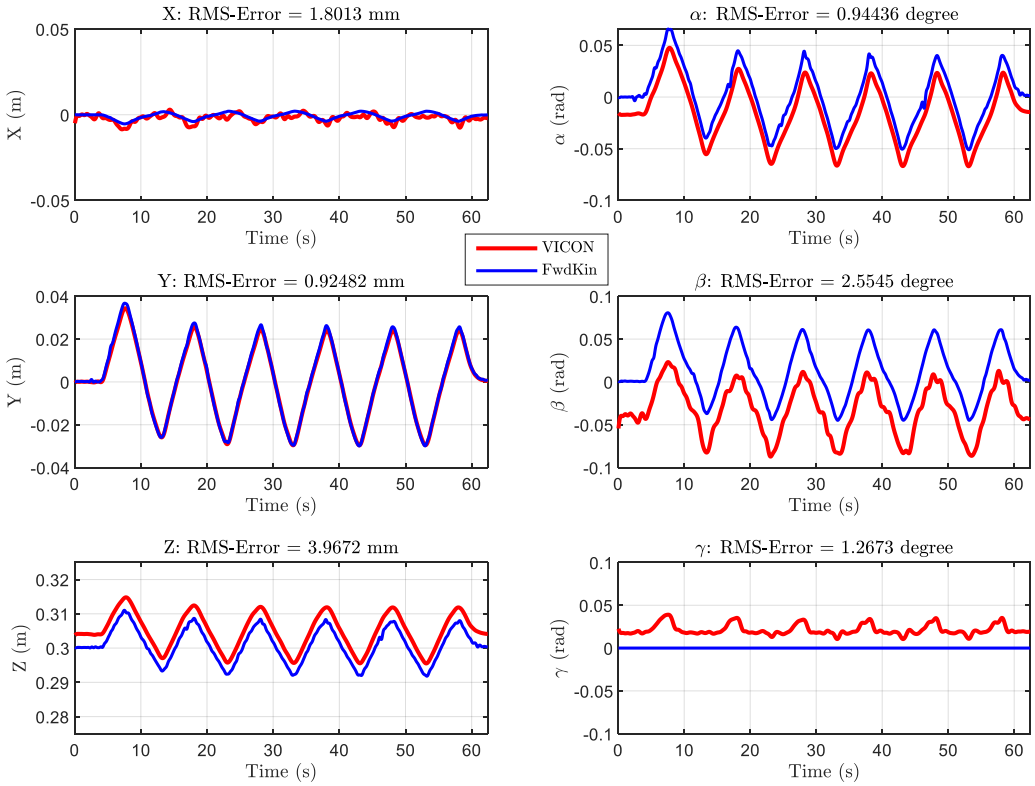

Figure 2.12: Compound Out-of-Plane Movement ($y - z$ translation and rotation about x and y)

2.5.2 Output Force and Moment Validation

The output wrench in the sagittal plane was evaluated. The robot was controlled in force mode as shown in Fig. 2.13. The pelvic brace was fixed to the bench and the thoracic brace was attached to an ATI Mini45 Force/Torque Sensor (ATI Industrial Automation, Apex, NC, USA), which was fixed to the frame, shown in Fig. 2.14. Forces in the y- and z directions, as well as a moment about x were, simultaneously applied with a frequency of 0.25 Hz and amplitude of 2 N, 5 N, and 2.5 N-m, respectively, as shown in Fig. 2.15. The root mean square (RMS) of the error in the y- and z directions were 0.866 N and 1.312 N respectively. The RMS of the error in the moments about the x and the y axis were 0.279 N-m and 0.179 N-m respectively.

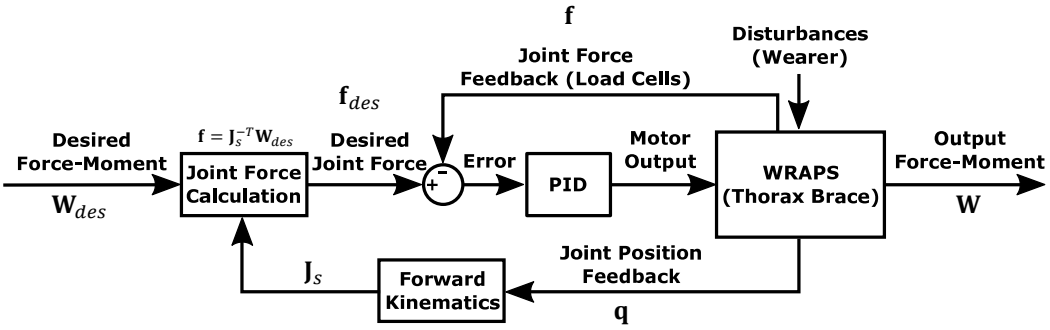

Figure 2.13: Force control mode

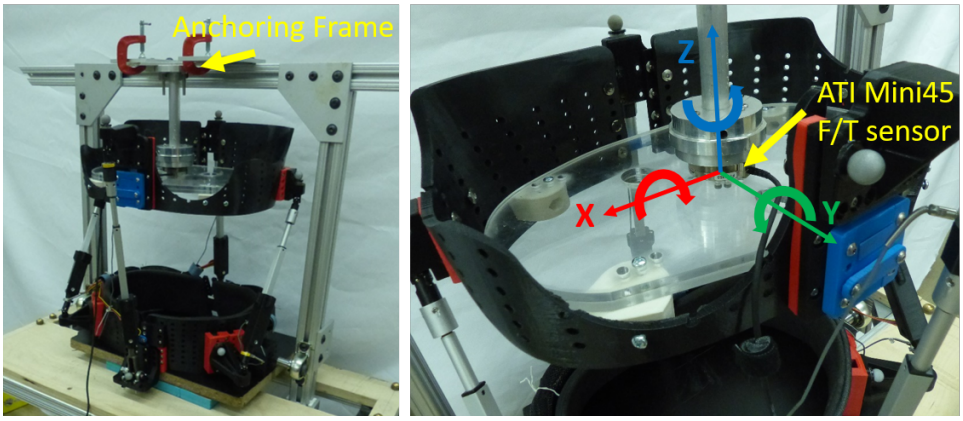

Figure 2.14: Test rig for the force-torque output validation

2.6 Human Evaluation

WRAPS design and performance were evaluated in seated able-bodied subjects [44]. We address three aims:

1. to characterize the torso range of motion (tROM) of users when wearing WRAPS in comparison to free-guided tROM without wearing it,

2. to determine the active-assistive capability of WRAPS to move the subjects on their own tROM trajectories while reducing activity of their primary torso muscles, and

3. to characterize the relationship between spatiotemporal features of muscle activation during the transparent mode and assistive sagittal forces and moment provided by WRAPS during the assistive mode.

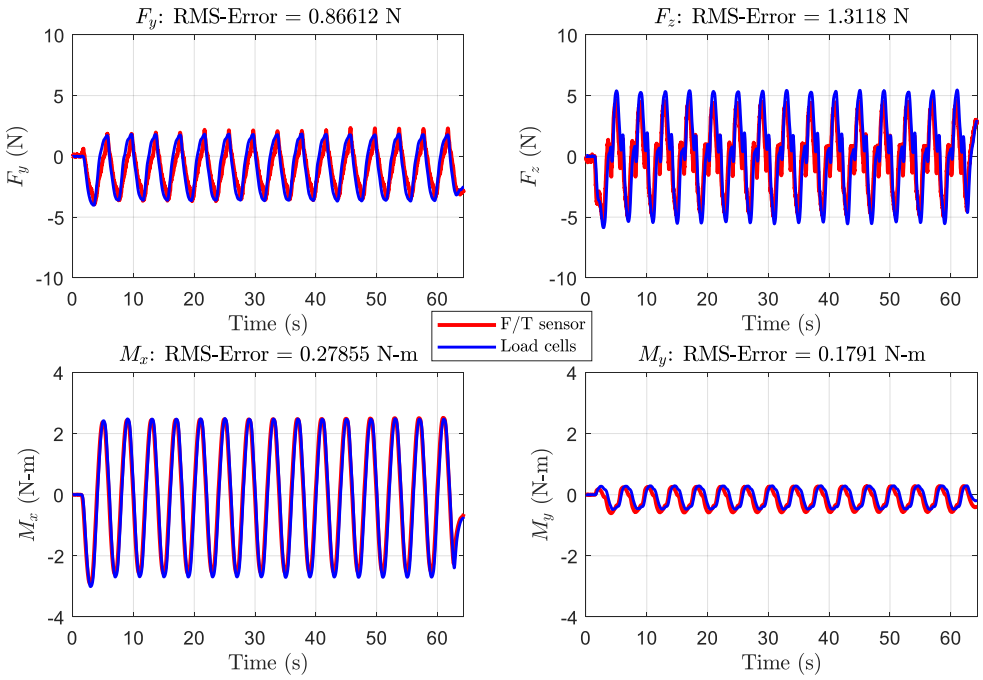

Figure 2.15: Force-moment accuracy

2.6.1 Experimental Protocol

The experiment was approved by the Institutional Review Board (IRB) of Columbia University (Protocol No. AAAR7388). Five healthy adult male subjects participated in the study with an average age of 26.60 years old (SD = 3.05 yr., range: 22 - 29 y/o.), 71.55 kg average weight (SD = 9.41 kg, range: 60 - 83 kg), 175.44 cm average height (SD = 7.67 cm, range: 167 - 184 cm), and 53 cm average torso height (SD = 3.08 cm, range: 51 - 58 cm) measured from the greater trochanter level to the suprasternal notch. The recruited subjects were within the adjustable range of the WRAPS brace sizes.

The experiment protocol is illustrated by the diagram in Fig. 2.16. In the "free" session, the subjects were constrained to the bench by the pelvic brace that is rigidly attached to it, while the upper trunk was unrestricted as shown in Fig. 2.17 (a). The subjects were instructed to move the torso relative to the pelvis in flexion-extension (main sagittal plane movement), lateral rotation (main frontal plane), and combined both planes of motion. The subjects were asked to perform the

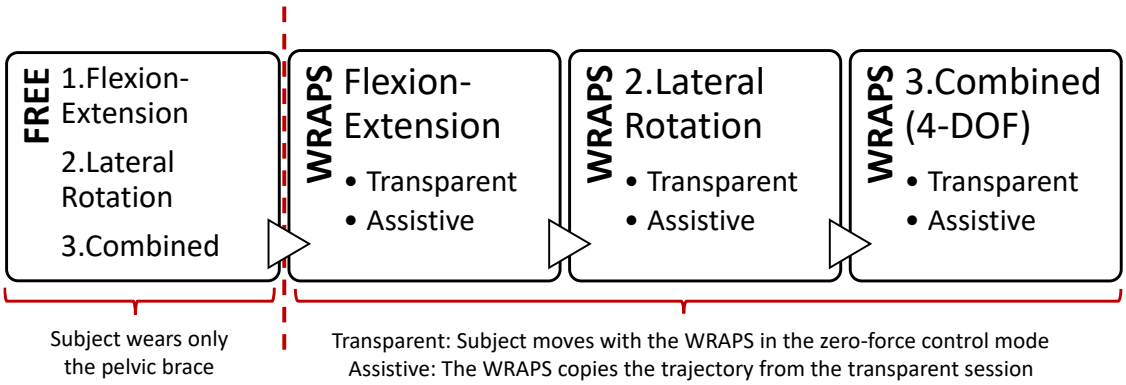

Figure 2.16: Experiment protocol

tROM in the given direction, starting from upright seating posture. A total of six continuous cycles were performed in each plane of motion. Additionally, a metronome was used to ensure a constant speed during movement.

Once the "free" session was completed, the subjects wore WRAPS, shown in Fig. 2.17 (b). The size of the WRAPS brace was adjusted and extra padding with semi-rigid foam was used to ensure the snug fit of the device on each subject. In the WRAPS session, the same three movement directions as in the "free" session were performed: flexion-extension, lateral rotation and combined motion (using all four DOFs of the device). Each movement was performed once in each of the two modes of the device in sequence as follows:

- Transparent Mode: the subject wore the WRAPS in the zero-force control mode, where the desired wrench $\mathbf{W}_{des}$ was set to be the zero vector, resulting in zero desired joint forces along all limbs, and thus the robot performed movements that complied with the forces exerted by the subject on the thoracic brace. The initial sitting posture when wearing the WRAPS was determined by the subject using this control mode. Then, the subject was instructed to perform the trunk movements to the maximum range of motion allowed by WRAPS. A metronome was used to pace trunk movements.

- Assistive Mode: the WRAPS was switched to the position control mode and was commanded to follow the tROM trajectories previously recorded during the transparent mode, copying the

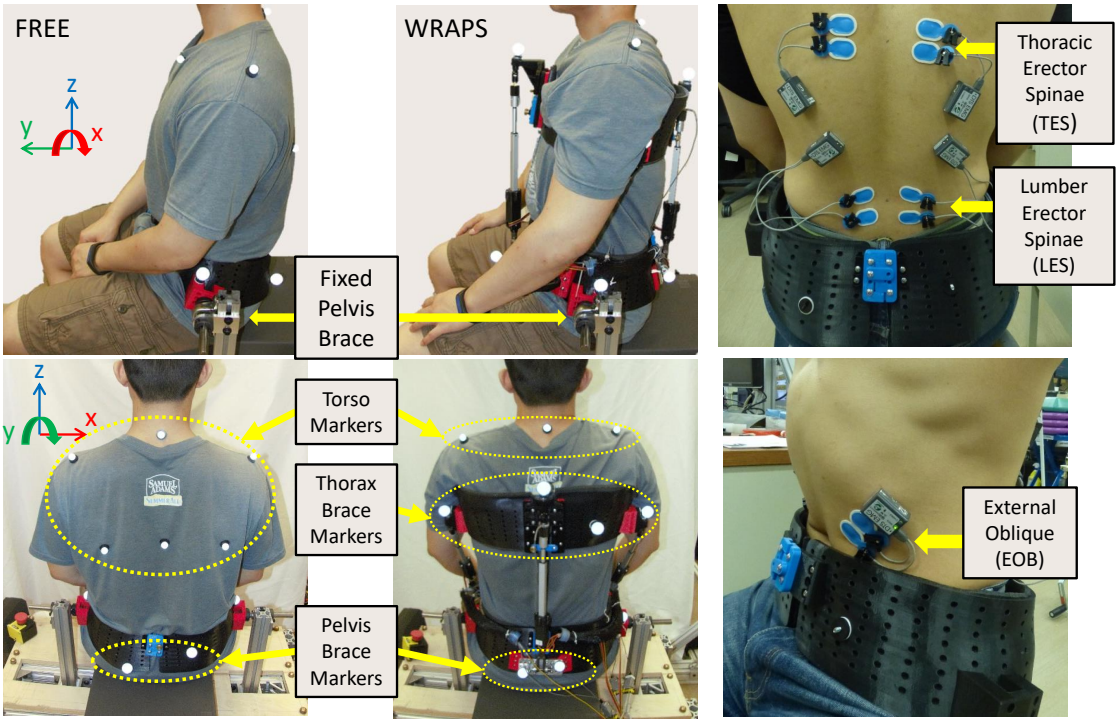

Figure 2.17: Experiment setup in (a) "free" session and (b) WRAPS session. (c) Placement of EMG electrodes on three trunk muscles groups: Thoracic Erector Spinae (TES), Lumber Erector Spinae (LES), and External Oblique (EOB). The coordinate frames roughly show the pelvis brace orientation in the figures.

physiological trunk motion of the subjects in the device. The subjects were verbally instructed to relax their torso muscles and avoid any voluntary trunk movement as the WRAPS followed the recorded trajectory.

Kinematics data was gathered via the control system of WRAPS together with additional measurements:

Motion Capture System

A set of eight motion capture system cameras (Vero v2.2, Vicon Motion Capture Systems, Oxford, UK) was used to track the motion of torso and the braces at 100 Hz. Marker placements during the "free" session corresponded to the anatomical landmarks proposed (Ref. [45]) to track the position and the orientation of the trunk: suprasternal notch, xiphoid process, C7 and T8 spinous

processes, right-left inferior angles of scapulae and right-left acromion processes. Furthermore, five markers were also placed on the pelvic brace (Fig. 2.17 (a)). In the WRAPS session (Fig. 2.17 (b)), only four markers were left on the subject's torso (suprasternal notch, C7, and right-left acromion processes) and 11 markers were placed on the pelvis and the thoracic braces of the WRAPS.

EMG Sensors

The overall muscle activity in the trunk was measured by surface EMG (sEMG). A wireless EMG system (TeleMyo™ Desktop Direct Transmission System (DDTS), Noraxon, AZ, USA) with sampling at 1500 Hz was used along with six electrode channels. The placements of the electrodes for measuring the sEMG of the muscle groups on the trunk were selected as suggested in Refs. [46, 47, 48]. The electrodes were placed bilaterally on three muscle groups as shown in Fig. 2.17 (c):

- Thoracic Erector Spinae (TES): 5 cm lateral to the T9 spinous process;
- Lumbar Erector Spinae (LES): 3 cm lateral to the L3 spinous process; and
- External Oblique (EOB): approximately 15 cm lateral to the umbilicus or just below the rib cage, along a line connecting the most inferior costal margin and the contralateral pubic tubercle.

Note that this selection of the positions of the electrodes prevents the electrodes from being compressed by the brace and minimizes artifacts recorded in the EMG signal. Some areas of the skin were shaved as necessary to improve the quality of the interface contact with the electrodes.

In addition, all recorded data from sEMG and the motion capture system were synchronized by using an analog sync box (Lock Lab, Vicon Motion Capture Systems, Oxford, UK). The motion capture software (Nexus 2.5, Vicon Motion Capture Systems, Oxford, UK) commanded the sync box to send a continuous high analog signal to the WRAPS control board and the wireless receiver of the EMG system during the data capture. Only the portion of recorded data with high analog sync signal was used.

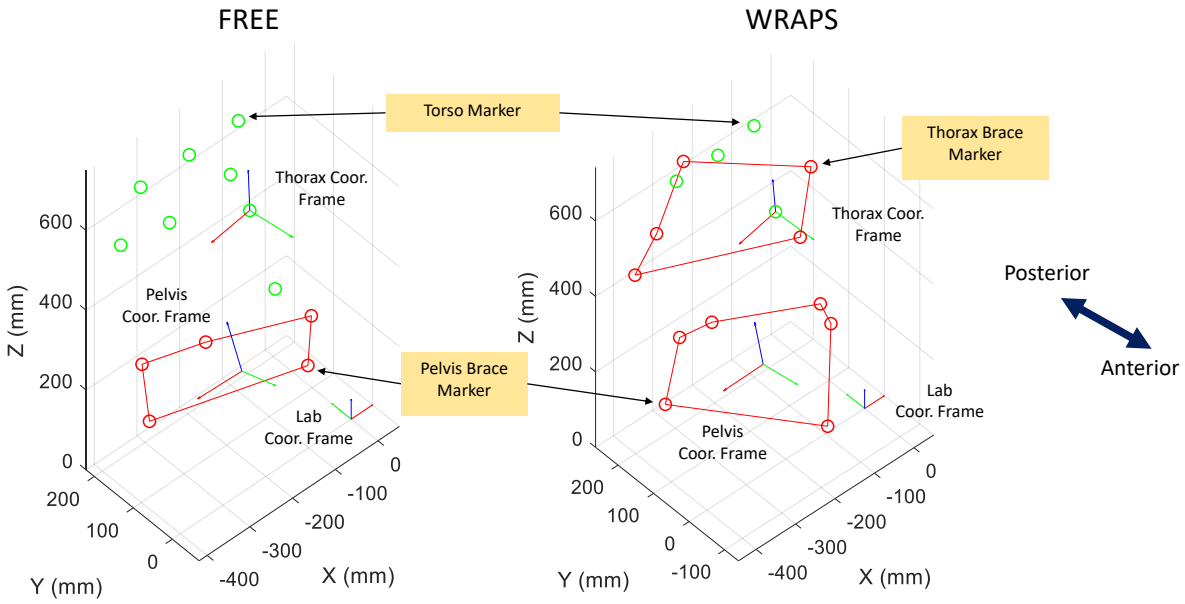

Figure 2.18: Vicon marker positions and constructed coordinate frames in a torso neutral configuration.

2.6.2 Data Analysis

Upper Torso Kinematics

The torso coordinate system was constructed by using marker positions on the anatomical landmarks, based on a guideline from Ref. [45]. The coordinate frame of the pelvis brace center was determined from marker positions in the 3D assembly model of the brace in a CAD software. A visualization of all coordinate systems in both sessions is presented in Fig. 2.18. We evaluated the kinematics of the upper torso of the subject by finding the transformation from the pelvic coordinate frame to the thorax coordinate frame. The output translational displacement (x, y, z) is from the pelvis frame origin to the thorax frame origin (the suprasternal notch), and the orientation of the thorax frame is in space-three 1-2-3 set of orientation angles $(\psi_x, \theta_y, \phi_z)$, corresponding to pitch-roll-yaw motion of the upper trunk. Fig. 2.19 shows an example of the processed trunk kinematics data in one movement of a subject for both the "free" and the WRAPS transparent trials. Fig. 2.19 (a) shows all six variables over time, and Fig. 2.19 (b) shows the trajectories of the

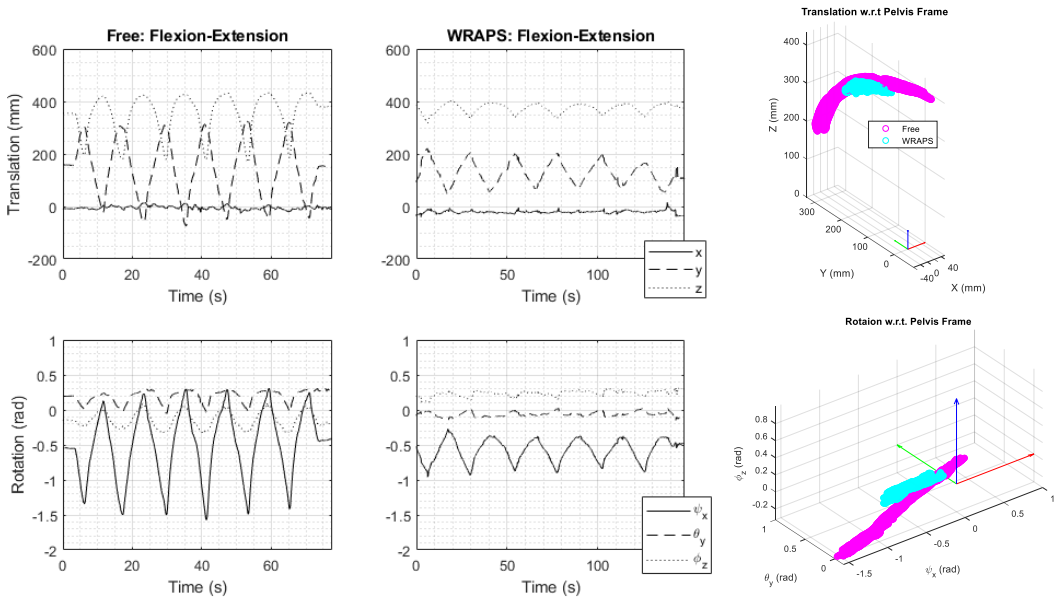

(a) (b)

Figure 2.19: Kinematics data of the torso flexion-extension movement of one representative subject with respect to the pelvis coordinate frame in both the "free" and the transparent trials in (a) all six DOFs over time and (b) the 3D trajectories of the translation and rotation over the entire movement.

WRAPS in the transparent mode overlaid with the trajectory in the "free" mode.

In order to calculate the trunk range of motion (tROM), we averaged the peaks of its dominant DOFs, namely (y, z, ψ_x) in the flexion-extension, and $(x, -z, \theta_y)$ in the lateral rotation. The peaks were found in both positive and negative directions relative to the starting position in each trial. The tROM in each DOF was calculated as a percentage of the average peak in the WRAPS session compared to the "free" session.

EMG Processing

The EMG processing was performed in myoRESEARCH® software (MR3.12, Noraxon, AZ, USA) and MATLAB® (R2018b, MathWorks, Natick, MA, USA) using suggested methods from Refs. [24, 49, 50]. First, the electrocardiography (ECG) data was removed from the raw measurement, then the data was detrended to remove the DC-offset of the signal. After this the band-pass filter of 30 – 500 Hz was applied to the signal, and then the band-stop filter (58 – 62 Hz) was applied

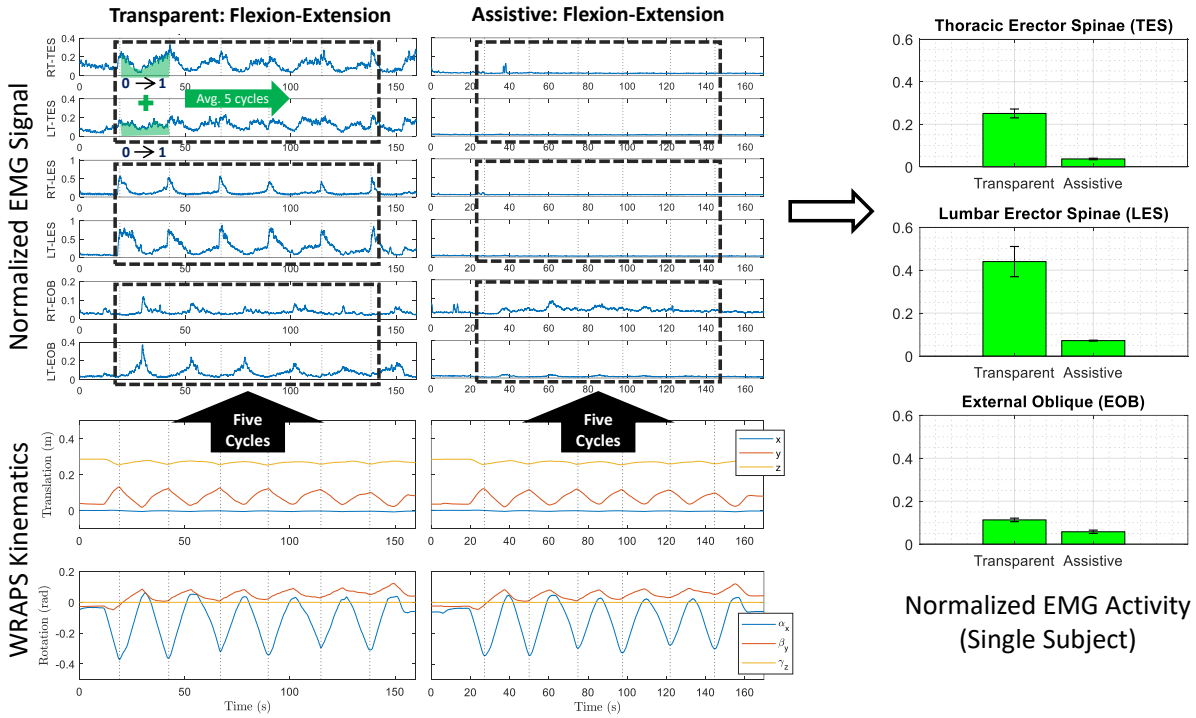

Figure 2.20: EMG processing of the flexion-extension movement of a subject wearing the WRAPS in the transparent and the assistive trials. Five cycles were determined by using the minimum peaks of the flexion-extension angles (α_x).

to remove the artifacts from the power line. The signal was then rectified and root-mean-square enveloped over the 500-ms sliding window. The signal magnitudes were normalized based on the maximum value in each channel occurring in the entire experiment.

In Fig. 2.20, the EMG signal was cut into cycles based on the kinematic data recorded from the WRAPS. Each cycle was specified by the interval from one peak to another in a selected degree-of-freedom. After this, all cycles were normalized by time. Finally, the summed integrated EMG data over the normalized time from the right and left muscles were averaged over the five cycles, representing the normalized EMG activity of each muscle group corresponding to a trial. Note that the kinematics of the WRAPS in both conditions were slightly different due to the delay from the time constant of the PID controller and different load conditions.

2.6.3 Statistical Analysis

The statistical package SPSS® (version 25, IBM, Armonk, NY, USA) was used for statistical analyses of the normalized EMG data between the transparent and assistive modes of the WRAPS. Data normality was explored with Q-Q plots and Shapiro-Wilk test. The alpha rate was set at 0.05 as significance level. For our single subject test, we used relative change with respect to baseline to describe WRAPS functionality in transparent and assistive modes within the same movement. In our group analysis (n = 5), a paired sample t-tests was used to examine significant differences. One subject was removed from the EMG analysis due to technical issues, as determined by extreme data outliers (three times greater than the interquartile data range).

2.7 Results and Discussions

2.7.1 Torso Range of Motion: "Free" vs. WRAPS Sessions

The tROM of the WRAPS in the transparent mode is compared to the tROM in the "free" mode in percentage of the average peak values. The group average %tROM in each DOF was calculated from two subjects with complete motion capture data (Fig. 2.21). Each DOF has two values of %tROM in positive and negative directions starting from the neutral configuration.

In Fig. 2.21 (a), WRAPS can achieve a higher %tROM in the flexion ($+y, -z, -\psi_x$) than the extension movement ($-y, +z, +\psi_x$). The device can achieve relatively high %tROM in the forward translation ($+y$) as well as the flexion angle ($-\psi_x$) at 69.0 ± 4.5% and 47.5 ± 10.6%, respectively. These outcomes indicate that the WRAPS can efficiently support the body and provide an in-device forward reaching distance very close to the user's natural reach. WRAPS was principally designed to expand the subject's functional reach space in the forward direction while proving comfortable and active full body weight support. The vertebral column is highly unstable in the vertical position [51], and the absent neuromuscular control of paravertebral muscles during extension movements may be the cause of further neural or soft tissue injuries in people which SCI caused by hypertension mechanisms [52].

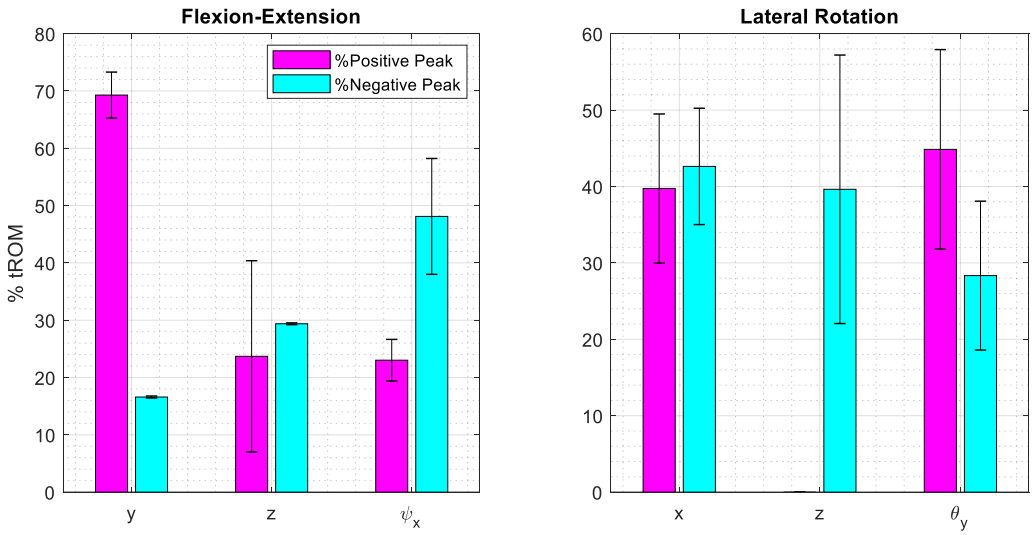

Figure 2.21: Average %tROM (n = 2) in the WRAPS compared to the "free" conditions in (a) flexion-extension and (b) lateral rotation movements.

In Fig. 2.21 (b), the lateral rotation in the WRAPS achieved uniform %tROM across all major DOFs of the movement. The average %tROM in lateral translation (x) achieved relatively symmetric values ($40.0 \pm 9.4\%$ and $42.5 \pm 7.8\%$ in positive and negative directions respectively). The downward translation ($-z$) also has the average %tROM ($40.0 \pm 17.1\%$) close to other DOFs. The slightly asymmetric %tROM of lateral bending angles ($45.0 \pm 13.2\%$ and $28.5 \pm 9.8\%$ on the right and left side, respectively) may be due to an offset neutral angle around the y axis of the device. Also, the %tROM can significantly vary by different pelvis and thoracic brace sizes across the subjects. The subjects with wider brace sizes tend to have less %tROM during the lateral rotation movement since the linear actuators in the UPS chains will have to reach longer lengths for the same angle of torso lateral rotation (θ_y).

2.7.2 Assistive Forces and Moment vs. Muscle Activation Pattern

During the assistive mode (position controller), the peak forces along the actuators when interacting with the subjects were always below the back drive force (102 N), and thus the robot was able to track the desired trajectories throughout the experiment. The peak forces that occurred throughout the experiment were 87.48 N in compression along the lateral UPS leg, and 90.83

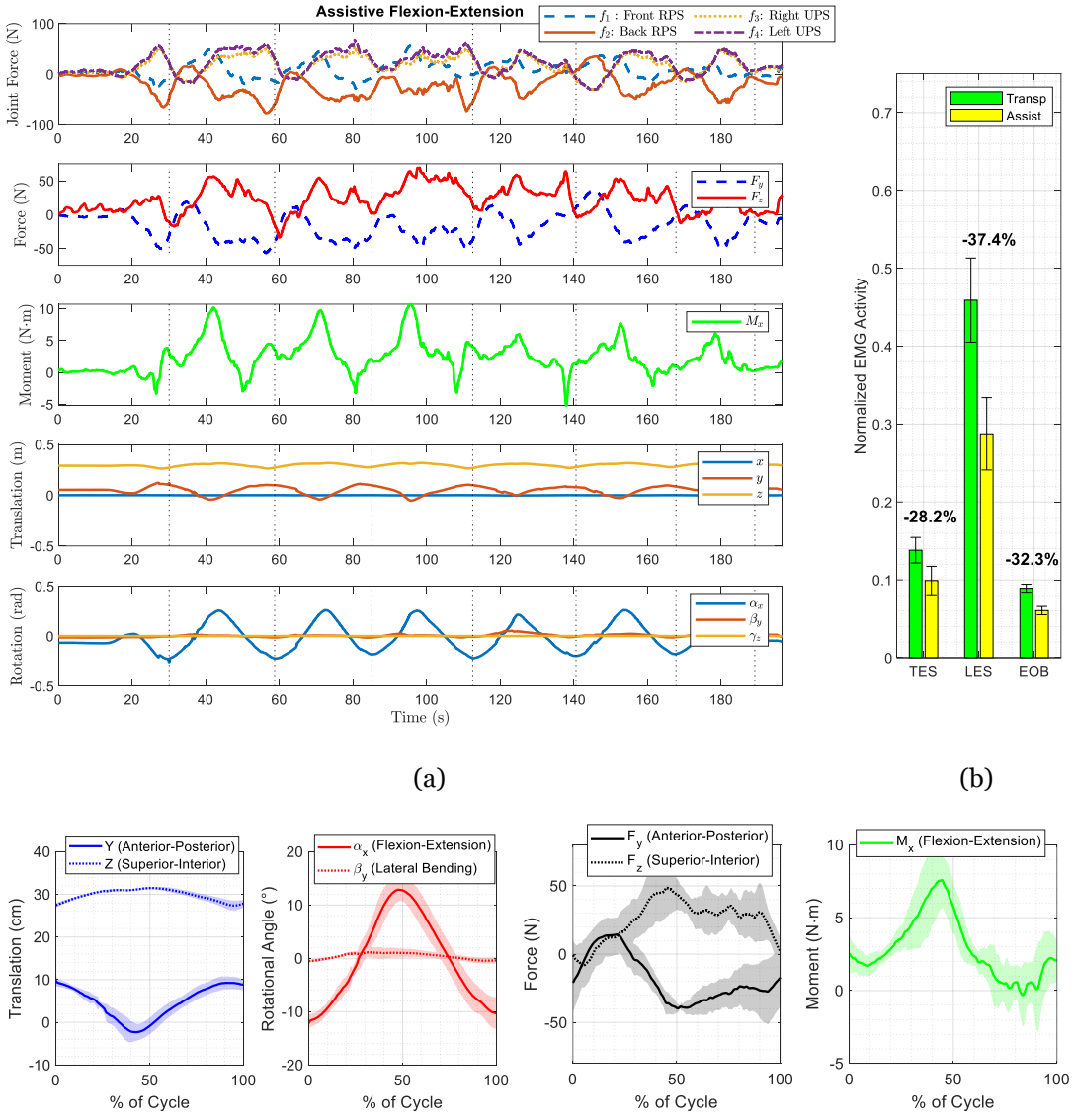

Figure 2.22: (a) Joint forces along limbs and sagittal forces and moment at the center of the thoracic brace in the assisted flexion-extension session in a representative subject. Dotted lines indicated the time when the WRAPS reached the extreme flexion motion. Positive and negative joint forces correspond to in-line tension and compression forces respectively. The forces and moment shown are the force applied on the end-effector by the wearer. (b) Normalized EMG activities of three muscle groups during transparent and assistive modes with relative percentage differences based on the transparent mode. (TES: Thoracic Erector Spinae; LES: Lumber Erector Spinae; EOB: External Oblique). (c) Average kinematics and force-moment data in five cycles of the same subject (one extreme flexion angle to another) with $\pm 1SD$ bands. The WRAPS reached the maximum flexion angle at 0% and 100% of the cycle.

N in tension along the rear [R$\underline{P}$]S leg. The maximum peak forces occurred during the assisted flexion-extension were 80.77 N in compression along the rear [R$\underline{P}$]S leg and at 70.66 N in tension along a lateral U$\underline{P}$S leg.

Since the structure of the robot was specifically designed to control and measure forces and moment in the sagittal plane, the recorded force data was exclusively correlated with the assisted flexion-extension movement. The joint forces, end-effector wrench, and kinematics data measured by the WRAPS of a representative subject are shown in Fig. 2.22 (a). Positive and negative joint forces correspond to axial tension and compression forces, respectively. The forces and moment shown are in the direction applied on the end-effector from interaction with the wearer. The time points at which the robot reached its extreme flexion angle are shown by vertical dotted lines. Given that all muscle activities in this healthy subject, shown in Fig. 2.22 (b), have decreased (-28.2% in TES, -37.4% in LES, and -32.3% in EOB), the characterization of the assistance provided by the WRAPS in this case could be related to the patient group with low muscle strength in the torso.

There are distinct trends of the end-effector sagittal forces (F_y, F_z) and the moment (M_x) during this cyclic flexion-extension motion. For easier interpretation of the data, the kinematic and force-moment data of the representative subject in Fig. 2.22 (a) were averaged throughout the five time-normalized cycles and then shown in Fig. 2.22 (c). The unique characteristic of the assistive forces and moment were delineated in four consecutive phases of the movement as follows:

Flexion to Neutral Phase (0% – 25% of Cycle)

In the third plot from the left in Fig. 2.22 (c), the resultant sagittal force vector $\mathbf{F} = \begin{bmatrix} 0 & F_y & F_z \end{bmatrix}^T$ on the torso (opposite direction of the forces shown in the the plot) started from the forward direction due to the guiding force in the previous cycle that assisted the torso to reach the terminal flexion angle. After that, the force shifted toward the posterior and inferior direction (pulling torso backward and downward) in order to adjust the body back to the neutral configuration. It can be observed that joint force along the rear [R$\underline{P}$]S limb changed from compression at the 0% of the cycle to the tension at the end of this phase. This joint force profile was similar to the main activation pattern of

the LES muscle during the same phase of motion in the transparent mode as seen in Fig. 2.20. The onset of peak activation by the TES and LES muscle were immediately after the extreme flexion motion and remained high shortly afterwards. It could be concluded that the substantial decrease of required muscle activity in the LES was contributed by this assistive joint force. Note that the magnitude of the tension force along the rear [RP]S limb was relatively low, possibly due to the additional compressive force from the torso inertia when it was shifted backward. Interestingly, the moment from the inertia of the torso rotating backward was greater than the gravitational torque from the weight of the torso, resulting in the small positive value of flexion-extension moment reaction on the WRAPS.

Neutral to Extension Phase (25% – 50% of Cycle)

The direction of the F_y and F_z rapidly diverged from each other at the beginning of the cycle. The F_y returned to the negative direction again, meaning that after the sagittal angle (α_x) of the thoracic brace had shifted to the positive direction (extension), the subject's torso weight immediately shifted backward until the F_y reached its peak at around –40 N at the extreme extension angle. Meanwhile, the increase in the positive vertical reaction force F_z on the end-effector was mainly due to the extension of the spinal column, which overcame the downward gravitational force of the torso. In contrast, the sagittal moment reached its peak at the end of this phase, reflecting the gravitational moment from the fully extended torso. During extension movements, it can be concluded that the subject's torso weight was shifted backwards, and the WRAPS had a major role in supporting the upper body in the vertical position. This biomechanical effect was observed during low, or almost inexistent, EMG activity abdominal muscles (EOB) that were used to stabilize the reclining motion during the transparent mode. This is an important finding in WRAPS since people with total low cervical or high-thoracic SCI do not have muscle stabilization of the torso and passive orthosis could not offer this active regulation of compression forces in vertical or during active extension movements. Furthermore, it was reasonable to observe that the front [RP]S and the lateral UPS limbs that have the configurations similar to the abdominal muscles, like the Rectus Abdominis

and the EOB, respectively, are dominantly under the tension at the terminal extension angle. This pattern is supported by the representative data in Fig. 2.20, which shows that both left and right EOBs reached their peak activity when the torso is fully extended in the WRAPS.

Extension to Neutral Phase (50% – 75% of Cycle)

The magnitude of the sagittal force vector slightly decreased while the torso was moving back to the neutral configuration (more neutral spinal column). At the same time, the gravitational moment M_x on the end-effector rapidly decreased during this phase to nearly zero. This outcome is well related with the noticeable reduction of the tension force along the front [RP]S leg when the gravitational moment was disengaged (Fig. 2.22 (a)), while the lateral UPS legs were still maintaining more tension throughout this phase since their diagonal vectors were more aligned with the partially extended upper spinal column and also mainly contributed to the end-effector anterior force that push the body forward to the neutral position.

Neutral to Flexion Phase (75% – 100% of Cycle)

The main reaction force was still in the backward direction since the WRAPS was pushing the torso forward to the flexion posture, meanwhile, the gravitational moment M_x from the torso shifted more into the negative direction. Interestingly, the resultant moment magnitude in the negative direction was still relatively low since the positive reaction moment from the effort by the robot trying to bend the body forward significantly compensated the gravitational moment from the torso.

In summary, during the represented subject's assisted flexion-extension motion in the WRAPS, we can conclude that during the first phase (0% – 25%), the rear [RP]S limb can serve to supply the absent activity of the erector spinae muscle group in people with SCI to extend the torso back to the neutral configuration. In the second phase (25% – 50%), the front [RP]S limb and the lateral UPS limbs acted like the abdominal muscle groups which stabilized the torso when reaching the fully extended position. In the last two phases (50% – 100%), the front [RP]S limb exclusively controlled the flexion-extension moment on the torso while the steady vertical and horizontal force components

that mobilized the torso forward were specifically controlled by the tensions along the lateral UPS limbs, favored by their symmetrical and diagonal configuration in the sagittal plane. In Fig. 2.22 (a), the joint forces along the lateral UPS limbs (f_3, f_4) are nearly the same in both directions and magnitudes throughout the entire movement. This means that if the recorded movement during the transparent mode is symmetrical around the sagittal plane, the design of the WRAPS will maintain equally distributed forces among the actuators around the sagittal plane when displacing the torso through the copied trunk movement. This design merit may provide additional vertebral stability of the WRAPS user.

These observed patterns may slightly vary with differences in anthropometric measurements as well as the movement speeds. It is also important to note that the representative subject had the same range of flexion and extension angles in the device. This tROM was based on the self-selected neutral configuration of the subject. In addition, the cyclic movements in this experiment were continuous, which might be different from normal seated tasks that involve prolonged static postures, such as reaching something on a shelf. Nevertheless, the synergies between the actuations and the kinematics of the trunk found in this experiment could be potentially generalized to a template for patients with similar anthropometry.

2.7.3 Group Comparison of sEMG between Transparent vs. Assistive Modes

The average normalized sEMG activity for each muscle group across cycles in the three different movements were analyzed (Fig. 2.23). The EMG data shows a general trend of reduced muscle activity during the assistive mode. Furthermore, statistical significance was found between the two WRAPS modes of control for specific muscle groups. The normalized EMG activity of TES was significantly reduced during the combined movements in the assistive mode (M = 0.062, SD = 0.034) compared to the transparent mode (M = 0.129, SD = 0.031); t = 3.25 (3), p = 0.048. Similarly, in the assistive mode, there was a significant decrease of the normalized EMG activity in the EOB muscle group during lateral rotation movements (M = 0.048, SD = 0.020) that was not found with the transparent mode (M = 0.106, SD = 0.038); t = 3.66 (3), p = 0.035.

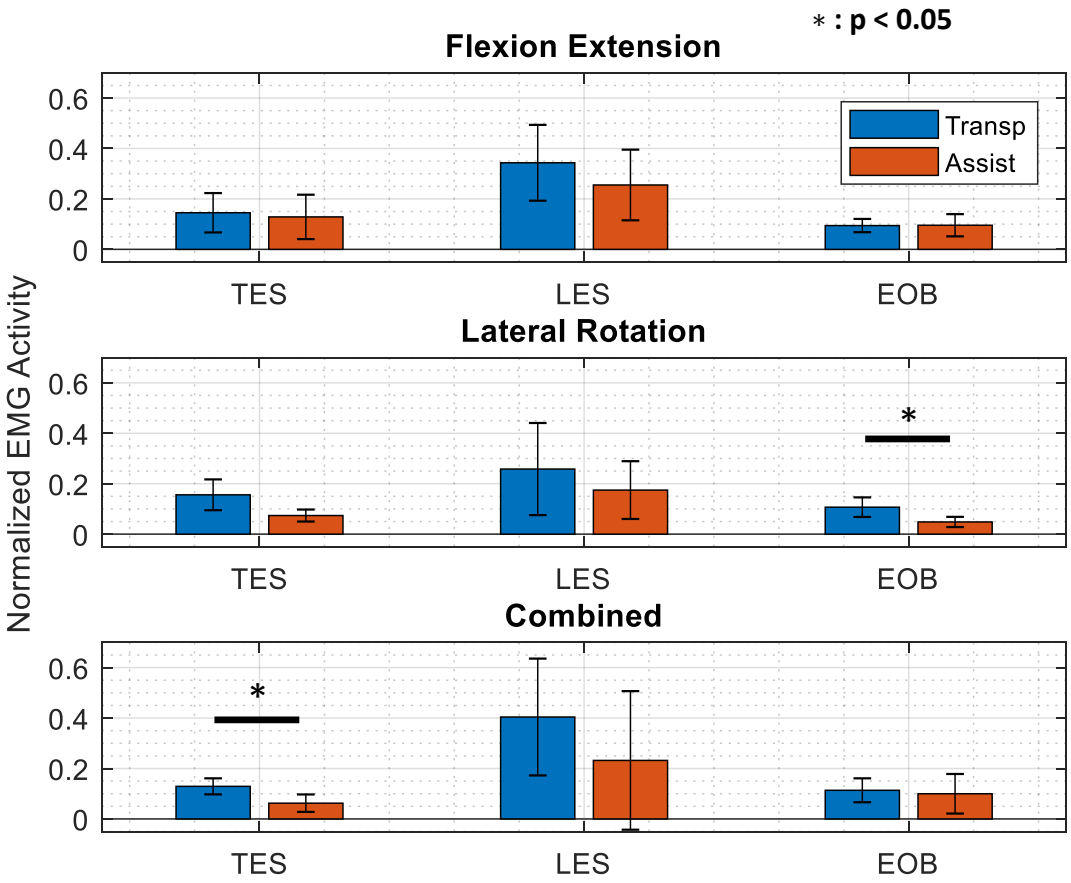

Figure 2.23: Subject group average (n=4) of the normalized EMG activity on each muscle group during three movements.

The reason we do not see statistically significant reduction of the average EMG activity throughout all muscle groups may be due to different strategies that healthy subjects used to move the brace in the transparent mode. Some subject might already have minimized their muscle activation because of high sensitivity of the zero-force controller. The speed of the metronome of some subjects were adjusted to be slightly slower to ensure that the subjects could reach their extreme positions in the brace while keeping up with a tempo, which might be a reason why these subjects produced only marginally higher EMG activity in the transparent mode respective to the assistive mode. Furthermore, the subject-based normalization technique that was used may provide inconsistency in the ranges of calculated normalized muscle activity. Tuning controller gains based on perception and strategy of each subject may also lead to different EMG activity levels. It is also interesting to investigate the EMG activity during the “free" movement in comparison with the WRAPS conditions; the speed of the movement as well as the tROM have to be similar in order to the make the EMG activity comparable across these two conditions.

A selected subject’s center of pressure (COP) at the base of support was tracked via a force plate (Bertec, Columbus, Ohio, USA), shown Fig. 2.24. In transparent mode, the subject was able to achieve a 1.9 cm excursion of the COP along the anterior-posterior (a-p) axis. The COP primarily traveled during the flexion phase of the movement. During the extension phase, the COP remained in approximately the same location on the a-p axis as when in the neutral position. However, during this phase there was a substantial amount (1.9 cm) of lateral movement of the COP, which could indicate some instability of the trunk. In addition, large lateral displacement of the COP can cause most of the force from the user’s weight to go through only one ischial tuberosity, rather than being distributed through both. This can increase the peak pressure on the user. On the other hand, anterior displacement allows one to distribute the pressure between both ischial tuberosities and the femurs and feet, which reduces the peak pressure. In assistive mode, the subject achieved a slightly greater COP excursion distance of (2.1 cm) along the a-p axis. The lateral excursion during the extension phase is much smaller (0.8 cm), which suggests greater torso stability. This suggests that the WRAPS may be able to assist users in modulating underseat pressure.

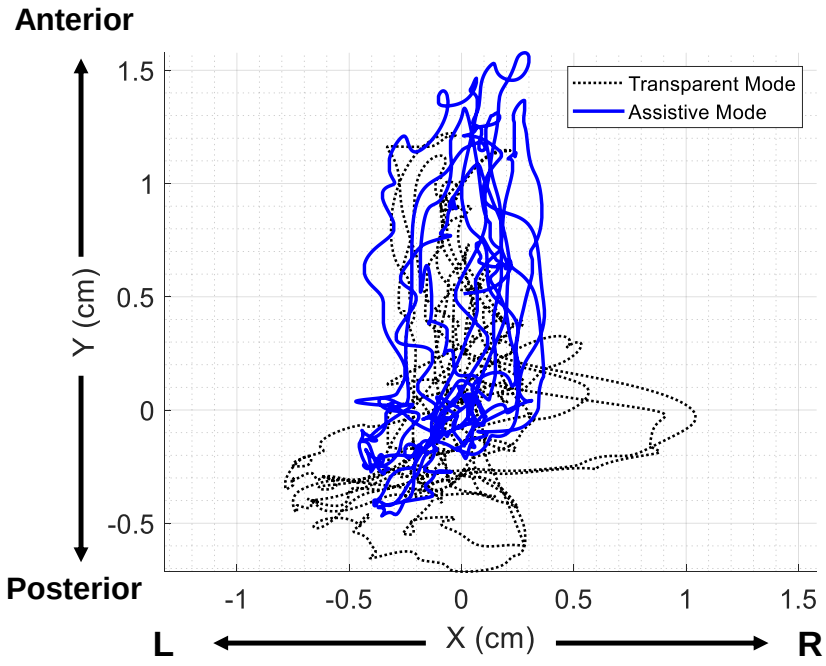

Figure 2.24: Center of pressure excursion at base of support

2.8 Conclusions

We examined in seated healthy subjects the trunk range of motion in the sagittal and frontal planes with WRAPS in two modes: transparent (i.e. zero force control mode) and assistive mode (position control). The data from these two modes were compared with the condition without WRAPS ("free" condition). In summary, WRAPS was able to safely and comfortably sustain and stabilize the concomitant active forces resulting from the torso of healthy young adults (mean = 71.55 kg) during assisted trunk motion. No major complaints (i.e. pain or excessive paravertebral muscle fatigue) were reported by the subjects. Our outcomes show that WRAPS can accommodate trunk trajectories that are close to physiological trunk ROM in sitting position along the sagittal and frontal planes, considering the hardware limitations. Furthermore, the position control mode can be efficiently applied to guide the torso throughout the planar trajectories that copy torso movements registered during the transparent mode. Importantly, our sEMG data demonstrates that WRAPS can reproduce such trunk trajectories with a significant reduction in EMG activity of primary torso

muscles, which is a condition expected in people with SCI. Moreover, the WRAPS actuation pattern is mechanically closely related to the spatiotemporal activation of abdominal and erector spinae muscle groups; and thus, it may be used to replace such muscle function in people with SCI without trunk muscle control. Altogether, these preliminary observations open new frontiers in the future safe and efficient application of WRAPS in patients with neuromotor disorders and profound trunk control deficits like SCI at cervical or high-thoracic levels, spina bifida, cerebral palsy with severe axial hypotonia and neuromuscular conditions.

As a limitation, only male subjects participated in the present study. Therefore, future work will aim at the improvement in the adjustability and the ergonomics of the WRAPS to fit both genders and a wider range of torso dimensions. An admittance-based controller can be implemented in future as an alternative to the direct PID force controller to improve the stability and robustness when the system is interacting with healthy subjects, while the impedance-based controller can be used during the assistive mode to improve the interaction forces with the wearer. As a statistical note, we think that the lack of power due to low sample size could be masking the presence of further significant EMG activity reductions during the assistive mode.

Furthermore, the user intention via an external manipulandum, like a joystick, will be incorporated into the control of the robot to offer independence and greater level of motor flexibility to users with absent trunk control. An upper-body motion mode recognition from inertia measurement units (IMUs) with machine learning algorithms (Ref. [53] can potentially be combined with an assist-as-needed controller to encourage functional activities performed by population with partial trunk motor impairment like cerebral palsy patients to encourage healthy postures and delay the muscle atrophy. It is also interesting to investigate the change in the pressure distribution in the gluteal region when the WRAPS is guiding the torso in different movements. Velocities and acceleration profiles of the devices with the trunk movements also remain to be explored in the future.

Chapter 3: WRAPS Design for Pelvis Motion

The motion of the pelvis is a challenge for wheelchair users. Even during sitting, motion of the pelvis plays an important role during functional movements. However, for people with trunk impairments, it is often a challenge to maintain a healthy alignment of the pelvis. The control of the trunk often starts at the neck and progresses down to the pelvis. For someone with poor trunk control, the lower segments of the trunk need to be stabilized in order to effectively use the upper segments. Another consequence of trunk instability is that the pelvis can often end up tilted in the frontal plane, referred to as pelvic obliquity, which can lead to twisting of the trunk, i.e., scoliosis. While sitting with pelvic obliquity, the majority of under seat pressure gets concentrated on a single ischial tuberosity, placing it at risk for pressure sores. In addition, there is a wide variation in the dimension and habitual posture of the pelvis. In light of these restrictions, it is desirable to build a pelvic robot module that can accommodate a range of pelvis heights, widths, and tilt angles in different directions on the seat.

Regarding the underlying mechanism design for the robot, pelvic movements while seated are very task specific and highly individual. The movements also depend on external constraints, such as the seat surface, the foot support, the back rest, the arm rest, and the upper-body posture etc. These complexities make it challenging to obtain a generalized model of human motion. Hence, we selected motion capture data as an integral part of this new mechanism design. Human segmental kinematics is widely studied by using instantaneous screw axes (ISAs). Page et al. studied the torso flexion-extension motion while seated and observed that the ISA locations of the thorax and the pelvis are contributed from the rolling motion of the pelvis and relative motions between vertebral segments [54].

Only a few designs of robot devices have been based on empirical ISA or motion capture data. A single-DOF finger rehabilitation exoskeleton was optimized by fitting the mechanism motion

path to that of the collected finger movement data [55]. A spatial 3-DOF parallel manipulator (PM) for accommodating the head-neck motion was also developed [56]. However, these studies mainly focused on minimizing trajectory errors whereas the performance aspects of the mechanism had less priority in the design. Other exoskeletons or rehab devices based on PMs were proposed along with optimization of some kinematic performances [57, 58, 59, 60], yet their designs were still developed based on simplified human joint models.

To the best of the authors' knowledge, a robotic exoskeleton for assisting the pelvis motion while seated has not yet been developed. Also, a mechanism optimization procedure that systematically considers ISAs from human movement data, the workspace, and the kinematic performance has not been established [61].

3.1 Design of a Pelvic Robot

A custom-made rigid pelvic brace was fabricated as the platform of the new robotic mechanism. The 3D CAD assembly of the brace is shown in Fig. 3.1. The pelvic brace consists of 3D-printed Acrylonitrile Butadiene Styrene (ABS) plastic parts (Fortus 360mc, Stratasys, Eden Prairie, MN, USA), connected by machined aluminum plates. An array of holes around the brace were created as the feasible joint attachment points with kinematic limbs. The brace dimensions can be adjusted in both width (x-axis) and depth (y-axis) to fit the subject's pelvis. Reflective infrared markers for collecting motion capture data are attached to the brace through dedicated screw holds or adhesives, and the xyz positions of the markers with respect to the pelvis coordinate frame $\{O_p\}$ are determined by the CAD model as shown in Fig. 3.2. Donning and doffing is done using thumb screws and quick-release pins on the lateral aluminum plates (opening point). When fitting the pelvic brace, the local coordinate frame of the pelvic brace $\{O_p\}$ is aligned in front of the umbilicus of the subject, and mechanical pointers with vertical adjustments (z-axis) are bilaterally leveled with anterior superior iliac spine (ASIS) and the posterior superior iliac spine (PSIS) of the subject. Some soft foam paddings are lined inside to ensure a snug fit and improve wearer comfort. This fitting based on the anatomical landmarks allows us to estimate the position and orientation of the subject's pelvic

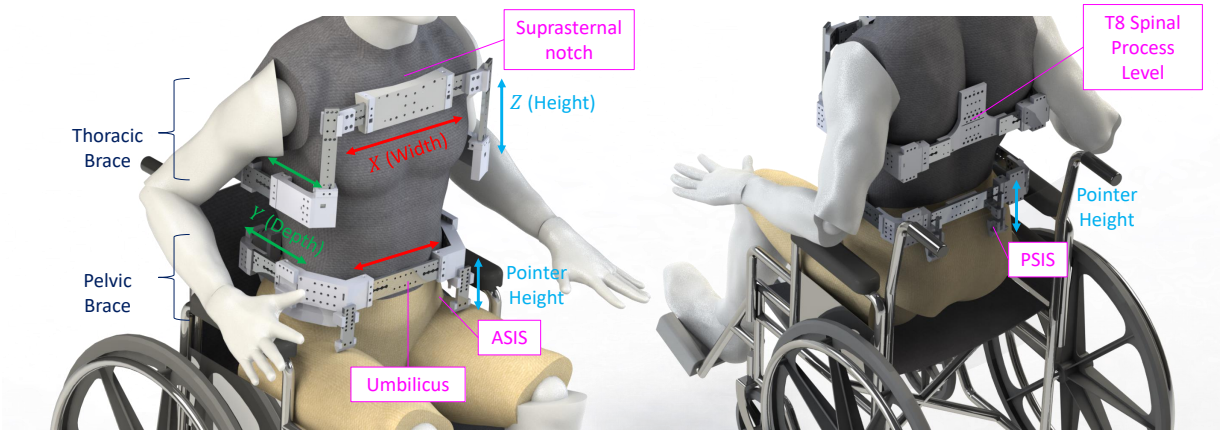

Figure 3.1: New design of pelvic and thoracic braces with adjustable dimensions and positions for aligning with anatomical landmarks on a subject.

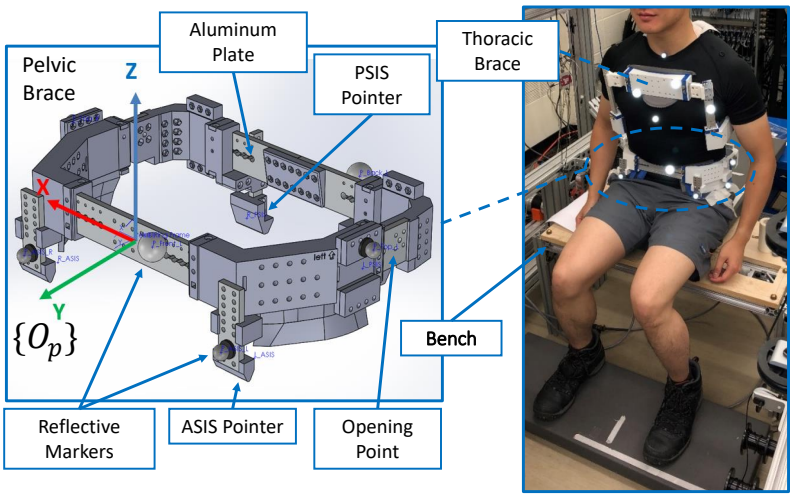

Figure 3.2: 3D CAD model of the pelvic brace with Vicon markers and experiment setup for data collection of seated movement from a healthy subject

bone relative to the seat in near real-time. A new thoracic brace was also designed and fabricated in the similar manner. The fitting is based on the anatomical landmarks on the subject's upper trunk. The height of the chest pad on the thoracic brace can be adjusted in order to independently align the suprasternal notch of the subject to the front of the upper edge of the chest pad and the the T8 spinal process level on the back part of the brace.

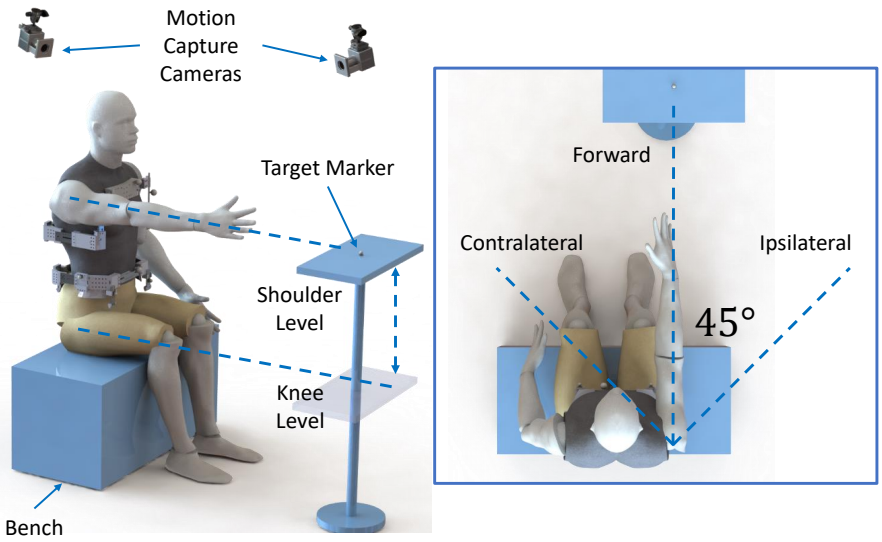

Figure 3.3: Reaching positions in three directions and two elevations

3.2 Human Movement Data

The data collection protocol was approved by the Institutional Review Board (IRB) of Columbia University (Protocol No. AAAR7388). A healthy adult male subject was the participant (Age: 25 years old, Weight: 70.0 kg, Height 173.0 cm, right dominant hand and foot). The experimental setup is shown in Fig. 3.2 and Fig. 3.3. The subject sat upright on a rigid bench without a back rest while keeping ankles, knees, and hip at approximately 90-degree angles in the neutral configuration. The pelvic and the thoracic braces were fitted on the subject's body with reflective markers attached on both the braces and the body. Note that the two braces are unconnected, allowing the subject to move the thoracic and the pelvic segments independently. A set of ten cameras (Vero v2.2, Vicon Motion Capture Systems, Oxford, UK) was used to track marker positions at 100 Hz. A static neutral posture of the subject was recorded for five seconds. After that, the subject was instructed to perform seated torso movements in 20 sessions described in Table 3.1. Sessions 15-20 are reaching tasks where the setup is shown in Fig. 3.3. A reflective marker was placed on a height-adjustable stool at the pre-determined maximum of the subject's reach with the dominant arm fully extended. Six reaching positions are at the knee and shoulder levels; each level has three directions: in the line of the forward extended dominant arm with torso upright, and two lines at 45 degrees (measured by

Table 3.1: Recorded Seated Movement Sessions

No.	Movement Description
1-6	Move the torso to perceived extreme ROM in a plane of motion (sagittal plane: flexion-extension, frontal plane: right/left lateral bending, and transverse plane: right/left axial rotation) while still maintaining stability. Pause for five seconds then return to the neutral position.
7-12	Six cycles between the extreme ROM in each of the three planes of motion. Each plane of motion was performed at two speeds, paced by a metronome (30 and 60 beats/sec), four beats long between the neutral to an extreme position.
13-14	Six cycles of rolling the torso around the vertical axis in the counter clockwise direction, paced by a metronome. Each quadrant of a cycle was four beats long.
15-20	Six reaching positions. Reach the target by finger tips with the fully extended dominant arm and pause for five seconds, then return to the neutral position.

a goniometer) from the center in the ipsilateral and the contralateral directions. All motions besides the cyclic movements were at self-selected speeds.

The selected movements include most of the required functional sitting postures for ADL while avoiding excessive amount of the experimental time and the collected data. Movements in sessions 1-6 determine the workspace of pelvis at the margin of stability in each of the planes of motion. Sessions 7-14 record dynamic movements at two controlled speeds in the isolated and mixed planes of motion. These sessions provide us more continuous ISA data between the extreme ROM. The two different metronome paces were selected to approximate the low and high speeds where the subject was able to follow comfortably while maintaining stability. This may help us to obtain kinematic data for optimizing a design suitable for both quasi-static and dynamic motions. The cyclic movements in the sagittal and the frontal planes also correspond to the pressure relief maneuvers suggested in [16]. The design of reaching tasks was motivated by the references [62, 63]. The lower reaching at knee level was included to achieve a more comprehensive reaching

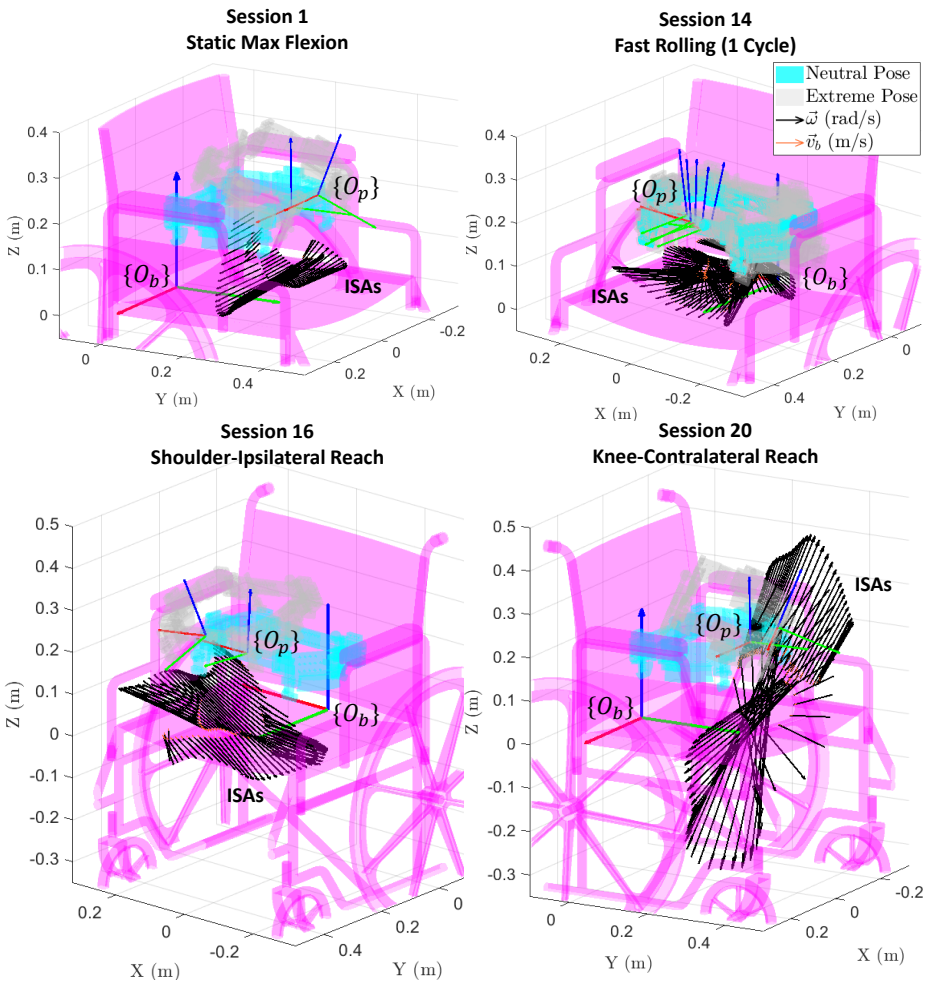

Figure 3.4: Axodes of the pelvic brace during (top left) a single cycle between the neutral pose and the maximum flexion, (top right) a cycle of fast rolling, (bottom left) an ipsilateral reaching at shoulder level, and (bottom right) a contralateral reaching at knee level.

workspace in front of the wheelchair, We expect variability in the shoulder extension angles to cover other reaching heights. The knee height reaching was found to stay within a comfortable ROM without the brace interference. This low reaching is extremely challenging for wheelchair users with trunk impairment without external assistance.

Note that the ROM of the subject when wearing the brace would be reduced compared to the subject's physiological ROM without the braces. This condition was intentional since the motion data would already include the effect of the hardware interference between the braces.

3.2.1 Motion Capture Data Processing

In this study, we only use marker positions on the pelvic brace. The raw marker position data were processed in a motion capture software (Nexus 2.5, Vicon Motion Capture Systems, Oxford, UK) and then analyzed in MATLAB® (version R2019b, MathWorks®, Natick, MA, USA) to obtain the coordinate frame and the ISAs of the pelvic brace segment. First, raw marker positions on the pelvic brace were smoothened by using a fourth-order zero-lag low-pass filter (cutoff at 1 Hz). Then the coordinate frame of the pelvic brace at each time step was computed based on a least-square method in [64]. The linear velocities of the markers were calculated by the five-point first-order differentiation. Finally, the ISAs of the pelvic brace were obtained from the linear velocities of the markers in the cluster using the pseudo-point-mass method in [54] when the magnitude of the angular velocity is over a certain threshold (25% of the peak angular velocity magnitude of each session). Also, a new coordinate frame $\{O_b\}$ on the wheelchair was defined, which is used as the inertial base frame of the robot, rather than the laboratory frame. All ISA data are with respect to this frame.

3.3 Mechanism Design Candidate

3.3.1 Motion Type Selection

Selected movement sessions with axodes (ruled surfaces created by series of ISAs) are shown in Fig. 3.4. The shape of an axode highly depends on the task. The ISAs are in all directions and change their location over time. These ISAs are also finite-pitch screws (or general screws) with relatively small pitch values. Therefore, we concluded that we desire a mechanism that provides the full 3D rotational motion while also allowing some coupled translation. A PM was desired for compactness, high stiffness, and low inertia due to the ability to place the actuators on the base [65]. However, PMs with higher DOFs (> 3) are less preferable due to additional limbs, leading to more space required and mechanical interference.

Some fully-actuated 3-DOF PMs with coupled motions in their uncontrolled DOFs have been

studied, such as the 3-[RP]S mechanism. In fact, this mechanism architecture has two main motion types, namely, T1R2 (zero-torsion design) or R3 (cubic/pyramid design) [66], depending on the limb arrangement on the base. Axode profiles were analyzed in the R3 (cubic/pyramid design) case of this mechanism [67, 68, 69] and would fit our design requirements well. In addition, a list of kinematic limbs called one-force-branches (OFBs), which can be used to achieve the R3 motion type, was compiled [70]. These limbs can be used to impose non-intersecting zero-pitch constraint wrenches on the platform.

3.3.2 Limb Design Candidates

Some considerations were used to select the limb candidates as follows: (i) we prefer a fully-actuated non-redundant PM having only one actuator mounted on the base at each limb; (ii) All limbs have the same connectivity of five between the end-effector and the base (number of 1-DOF joints); (iii) the PM consists of only the rotary joints (R: revolute, U: universal, S: spherical); (iv) the limbs tend to have simple kinematic solutions; (v) the geometric constraints of the platform are invariant in the space and are independent of limb dimensions; and (vi) the limbs are easy to manufacture. As a result, our selected limb candidates are [RR]S, and [RRR]U. These impose a 3D planar constraint on the platform. Our PM can either consist of a single limb type or a combination of the two limb types. Such a design will allow natural coupled translation of the center of mass of the user within a fixed range relative to the seat. This may intrinsically enhance the safety and minimize the slipping of the pelvis on the seat. Moreover, from not having any independent translation DOF, the size of rotational workspace will be always finite.

The planar linkage structure also provides a greater design flexibility. For example, the physical linkage dimensions can be selected to minimize the interference with the user and the wheelchair, while still satisfying the same screw system and the kinematic performance. The actuated joint positions on the wheelchairs can be chosen anywhere along the lines of the joint axes. In addition, the all-revolute-joint limb design can produce a wider range of the end-effector speed, higher backdrivability, and less bulky design compared to a design with prismatic joints.

3.4 Mathematical Models

3.4.1 Platform Inverse Kinematics

Consider the moving pelvic brace coordinate frame $\{O_p\}$ having an origin position ${}^b\mathbf{p}_p = \begin{bmatrix} x_p & y_p & z_p \end{bmatrix}^T$ and its orientation matrix ${}^b\mathbf{R}_p$ with respect to the inertial base frame $\{O_b\}$. Three known fixed local positions of spherical or universal joint centers of the ith limb are denoted by ${}^p\mathbf{b}_i = \begin{bmatrix} b_{x,i} & b_{y,i} & b_{z,i} \end{bmatrix}^T$. Each of the three constraint planar 3D surfaces is defined by two variables for a unit normal vector ${}^b\mathbf{n}_i = \begin{bmatrix} n_{x,i} & n_{y,i} & n_{z,i} \end{bmatrix}^T$ and a scalar value ρ_i for determining a point on the surface. A position on the plane with respect to the base frame is ${}^b\mathbf{d}_i = \begin{bmatrix} d_{x,i} & d_{y,i} & d_{z,i} \end{bmatrix}^T = \rho_i {}^b\mathbf{n}_i + {}^b\mathbf{d}_{i,o}$, where ${}^b\mathbf{d}_{i,o}$ is an optional constant offset position from the origin of the base frame. Since the spherical/universal joint center always lies in the plane, the constraint equation is

$$\left({}^b\mathbf{p}_p + {}^b\mathbf{R}_p {}^p\mathbf{b}_i - {}^b\mathbf{d}_i \right) \cdot {}^b\mathbf{n}_i = 0. \tag{3.1}$$

Rewrite (3.1) as

$$n_{x,i} \left(x_p + e_{x,i} \right) + n_{y,i} \left(y_p + e_{y,i} \right) + n_{z,i} \left(z_p + e_{z,i} \right) - \rho_i = 0, \tag{3.2}$$

where $\begin{bmatrix} e_{x,i} & e_{y,i} & e_{z,i} \end{bmatrix}^T = {}^b\mathbf{R}_p {}^p\mathbf{b}_i - {}^b\mathbf{d}_{i,o}$.

${}^b\mathbf{p}_p$ can be solved from the system of three linear equations in (3.2), given that all three unit normal vectors of the plane are linearly independent.

3.4.2 Twist of Constrained Platform

According to the Theory of Screws [71], an instantaneous motion of a rigid body in the 3D space (linear and angular velocities) with respect to an inertial frame $\{O_a\}$ can be uniquely represented as a screw motion (sliding and rotating) along a line in the 3D space. Details regarding the screw representation is in Appendix B.

The twist of the platform at a certain configuration and an angular velocity ${}^b\boldsymbol{\omega}_p$ can be directly obtained when constraint unit wrenches imposed by the three limbs are provided. First, we can write the constraint unit wrenches ${}^b\hat{\$}_{w,c,i}$ $(i = 1, 2, 3)$ in a form of column vector matrix or the Jacobian of constraints $\mathbf{J}_c$ as defined in [72]:

$$\mathbf{J}_c^T = \begin{bmatrix} {}^b\hat{\$}_{w,c,1} & {}^b\hat{\$}_{w,c,2} & {}^b\hat{\$}_{w,c,3} \end{bmatrix} \tag{3.3}$$

where in the case of the [$\underline{\text{R}}$R]S and [$\underline{\text{R}}$RR]U limbs, according to the reciprocity condition no. 1 in Appendix B, the constraint unit wrench of each limb is a pure force (zero-pitch wrench) which is always normal to the 3D planar surface and passes through the spherical/universal joint center of the limb [70] or

$${}^b\hat{\$}_{w,c,i} = \begin{bmatrix} {}^b\mathbf{n}_i \\ \left({}^b\mathbf{p}_p + {}^b\mathbf{R}_p {}^p\mathbf{b}_i\right) \times {}^b\mathbf{n}_i \end{bmatrix}. \tag{3.4}$$

If all the column vectors in $\mathbf{J}_c^T$ from (3.3) are linearly independent, we can obtain a set of three linearly independent twists that spans the twist space of the end-effector by calculating the left null space of $\mathbf{J}_c^T$, denoted as null$(\mathbf{J}_c)$:

$$\mathbf{G}_c = \text{null}(\mathbf{J}_c) = \begin{bmatrix} {}^b\$_{t,c,1} & {}^b\$_{t,c,2} & {}^b\$_{t,c,3} \end{bmatrix} = \begin{bmatrix} \mathbf{G}_v \\ \mathbf{G}_\omega \end{bmatrix}. \tag{3.5}$$

If $\mathbf{G}_\omega$ is invertible, the twist of the platform with respect to the base frame is

$${}^b\$_{t,p} = \mathbf{G}_c \begin{bmatrix} \mathbf{G}_\omega^{-1} \end{bmatrix} {}^b\boldsymbol{\omega}_p. \tag{3.6}$$

3.4.3 Maximum Virtual Loss Coefficient

Here, we propose a mathematical expression that evaluates the misalignment between a pair of twists (with the same axis direction and intensity) in the context of human assistance. Consider two systems of rigid bodies in the quasi-static condition: the human pelvic segment and the pelvic brace. Assume negligible slipping or deformation and identical positions of the pelvic brace from human data and the platform position. From the principle of virtual work, (neglecting gravity since the pelvis is supported by the seat), the instantaneous work or the power developed by all the wrenches acting on the human pelvic segment undergoing a twist ${}^{b}\underline{\$}_{t,p} = \omega_p {}^{b}\underline{\hat{\$}}_{t,p}$ is

$$\left(f_h {}^{b}\hat{\$}_{w,h} + f_{h-p} {}^{b}\hat{\$}_{w,h-p} \right) \circ \omega_p {}^{b}\underline{\hat{\$}}_{t,p} = 0, \tag{3.7}$$

and for the pelvic brace segment undergoing a constrained twist obtained in (3.6) ${}^{b}\$_{t,p} = \omega_p {}^{b}\hat{\$}_{t,p}$, the power developed from the wrenches is

$$\left(f_p {}^{b}\hat{\$}_{w,p} - f_{h-p} {}^{b}\hat{\$}_{w,h-p} \right) \circ \omega_p {}^{b}\hat{\$}_{t,p} = 0 \tag{3.8}$$

where $f_h {}^{b}\hat{\$}_{w,h}$ denotes an arbitrary resultant wrench from the human muscles on and/or other external wrenches that are transferred through the body to the physiological pelvic segment; $f_{h-p} {}^{b}\hat{\$}_{w,h-p}$ is a wrench of interaction between the human pelvic segment and the pelvic brace; and $f_p {}^{b}\hat{\$}_{w,p}$ is the resultant wrench on the pelvic brace by actuation and constraints of the limbs. Summing of (3.7) and (3.8) yields

$$\underbrace{f_p \omega_p {}^{b}\hat{\$}_{w,p} \circ {}^{b}\hat{\$}_{t,p}}_{\text{actuation work on platform}} = \underbrace{-f_h \omega_p {}^{b}\hat{\$}_{w,h} \circ {}^{b}\underline{\hat{\$}}_{t,p}}_{\text{-(external load/human work on pelvis)}} + \underbrace{f_{h-p} \omega_p {}^{b}\hat{\$}_{w,h-p} \circ \left({}^{b}\hat{\$}_{t,p} - {}^{b}\underline{\hat{\$}}_{t,p} \right)}_{\text{human-platform interaction term}}. \tag{3.9}$$

When the actuators are producing work or ${}^{b}\hat{\$}_{w,p} \circ {}^{b}\hat{\$}_{t,p} > 0$, it is desirable to have ${}^{b}\hat{\$}_{w,h} \circ {}^{b}\underline{\hat{\$}}_{t,p} < 0$, which means that the muscles are being assisted and/or any external load on the body transferred to the pelvis are being resisted. Hence, given that the human body is passive, the actuation power

transferred to the human pelvis will be minimized when the largest possible positive value of ${}^b\hat{\$}_{w,h-p} \circ \left({}^b\hat{\$}_{t,p} - {}^b\underline{\hat{\$}}_{t,p}\right)$ occurs. Similarly, in the back-driving case, where ${}^b\hat{\$}_{w,h} \circ {}^b\underline{\hat{\$}}_{t,p} > 0$, the magnitude of the negative back-drive power transferred to the robot actuators $\left({}^b\hat{\$}_{w,p} \circ {}^b\hat{\$}_{t,p} < 0\right)$ will be reduced most when the same term ${}^b\hat{\$}_{w,h-p} \circ \left({}^b\hat{\$}_{t,p} - {}^b\underline{\hat{\$}}_{t,p}\right)$ has its maximum positive value. Note that ${}^b\hat{\$}_{w,h-p}$ is an arbitrary unit wrench from the interface between the human and the pelvic brace. depending on the current robot configuration, the direction of the resultant wrench from the limbs on the platform, the wrench from human muscles, the hardware interface between the pelvic brace and the pelvis segment, etc.

Let $\Delta\tilde{w}_{h-p} := {}^b\hat{\$}_{w,h-p} \circ \left({}^b\hat{\$}_{t,p} - {}^b\underline{\hat{\$}}_{t,p}\right)$ define the Virtual Loss Coefficient (VLC) from the misalignment of the two unit twists undergoing an arbitrary unit wrench, and from (B.3) and the scalar triple product, it can be written in the following form:

$$\begin{aligned}
\Delta\tilde{w}_{h-p} &= {}^b\hat{\$}_{w,h-p} \circ \left({}^b\hat{\$}_{t,p} - {}^b\underline{\hat{\$}}_{t,p}\right) \\
&= \left({}^b\hat{\$}_{w,h-p} \circ {}^b\hat{\$}_{t,p}\right) - \left({}^b\hat{\$}_{w,h-p} \circ {}^b\underline{\hat{\$}}_{t,p}\right) \\
&= \left(h_{t,p} - \underline{h}_{t,p}\right)\left({}^b\mathbf{s}_{w,h-p} \cdot {}^b\mathbf{s}_{t,p}\right) + \left({}^b\mathbf{r}_{t,p} - {}^b\underline{\mathbf{r}}_{t,p}\right) \cdot \left({}^b\mathbf{s}_{t,p} \times {}^b\mathbf{s}_{w,h-p}\right) \\
&= \left(h_{t,p} - \underline{h}_{t,p}\right)\left({}^b\mathbf{s}_{w,h-p} \cdot {}^b\mathbf{s}_{t,p}\right) + {}^b\mathbf{s}_{w,h-p} \cdot \left(\left({}^b\mathbf{r}_{t,p} - {}^b\underline{\mathbf{r}}_{t,p}\right) \times {}^b\mathbf{s}_{t,p}\right).
\end{aligned} \tag{3.10}$$

Note that ${}^b\hat{\$}_{t,p}$ and ${}^b\underline{\hat{\$}}_{t,p}$ share the same unit vector of the twist direction ${}^b\mathbf{s}_{t,p}$. Then we can rewrite (3.10) as

$$\Delta\tilde{w}_{h-p} = \left(h_{t,p} - \underline{h}_{t,p}\right)\cos\vartheta + \left\|{}^b\mathbf{n}_t\right\|\cos\gamma, \tag{3.11}$$

where ϑ and γ are the projection angles of ${}^b\mathbf{s}_{w,h-p}$ onto ${}^b\mathbf{s}_{t,p}$ and $\left({}^b\mathbf{r}_{t,p} - {}^b\underline{\mathbf{r}}_{t,p}\right) \times {}^b\mathbf{s}_{t,p}$, respectively, and ${}^b\mathbf{n}_t$ is the common normal from the point ${}^b\underline{\mathbf{r}}_{t,p}$ on the line axis of ${}^b\underline{\hat{\$}}_{t,p}$ to a point on the line axis of ${}^b\hat{\$}_{t,p}$. Also, ${}^b\mathbf{n}_t$ is orthogonal to both ${}^b\mathbf{s}_{t,p}$ and $\left({}^b\mathbf{r}_{t,p} - {}^b\underline{\mathbf{r}}_{t,p}\right) \times {}^b\mathbf{s}_{t,p}$, and its magnitude (or common normal distance) is

$$\left\|{}^b\mathbf{n}_t\right\| = \left\|\left({}^b\mathbf{r}_{t,p} - {}^b\underline{\mathbf{r}}_{t,p}\right) \times {}^b\mathbf{s}_{t,p}\right\|. \tag{3.12}$$

Defining χ as the projection angles of ${}^{b}\mathbf{s}_{w,h-p}$ onto ${}^{b}\mathbf{n}_{t}$, we have directional cosine angles $(\vartheta, \gamma, \chi)$ of ${}^{b}\mathbf{s}_{w,h-p}$ with respect to the three orthogonal vectors ${}^{b}\mathbf{s}_{t,p}$, $\left({}^{b}\mathbf{r}_{t,p} - {}^{b}\underline{\mathbf{r}}_{t,p}\right) \times {}^{b}\mathbf{s}_{t,p}$, and ${}^{b}\mathbf{n}_{t}$, respectively. Choosing ϑ and χ as independent variables that define the line axis direction of the wrench ${}^{b}\hat{\$}_{w,h-p}$, from (3.11) and (3.12), the maximum amplitude of $\Delta\tilde{w}_{h-p}$ is

$$\begin{aligned} &\max_{\vartheta,\chi}\left|\Delta\tilde{w}_{h-p}\right| = \sqrt{\left(h_{t,p} - \underline{h}_{t,p}\right)^2 + \left\|\left({}^{b}\mathbf{r}_{t,p} - {}^{b}\underline{\mathbf{r}}_{t,p}\right) \times {}^{b}\mathbf{s}_{t,p}\right\|^2}, \\ &\text{when } \chi = \frac{\pi}{2}, \text{ and } \vartheta = \arctan\left(\frac{\left\|\left({}^{b}\mathbf{r}_{t,p} - {}^{b}\underline{\mathbf{r}}_{t,p}\right) \times {}^{b}\mathbf{s}_{t,p}\right\|}{h_{t,p} - \underline{h}_{t,p}}\right) \end{aligned} \tag{3.13}$$

or when the unit vector of the wrench axis ${}^{b}\mathbf{s}_{w,h-p}$ is parallel to the plane created by ${}^{b}\mathbf{s}_{t,p}$ and $\left({}^{b}\mathbf{r}_{t,p} - {}^{b}\underline{\mathbf{r}}_{t,p}\right) \times {}^{b}\mathbf{s}_{t,p}$, and also makes a certain projection angle on ${}^{b}\mathbf{s}_{t,p}$, which depends on the pitches and the common normal distance between the two twist axes. We define $\max_{\vartheta,\chi}\left|\Delta\tilde{w}_{h-p}\right|$ in (3.13) as the Maximum Virtual Loss Coefficient (MVLC).

Note that when $\chi = 0$: ${}^{b}\mathbf{s}_{w,h-p}$, being parallel to the common normal ${}^{b}\mathbf{n}_{t}$ and perpendicular to the plane formed by ${}^{b}\mathbf{s}_{t,p}$ and $\left({}^{b}\mathbf{r}_{t,p} - {}^{b}\underline{\mathbf{r}}_{t,p}\right) \times {}^{b}\mathbf{s}_{t,p}$, $\left|\Delta\tilde{w}_{h-p}\right|$ becomes zero regardless of the two twists. The other two trivial cases are having two identical twists and when the interaction wrench ${}^{b}\hat{\$}_{w,h-p}$ is a pure moment couple. Note that this mathematical evaluation is specific for that case where the two twists share the same intensity as well as the direction of the axis.

3.4.4 Limb Inverse Kinematics

Once we have computed the coordinate transformation of the platform in section 3.4.1, the position and the orientation of the last joint rotation axis in the spherical/universal joint can be obtained with respect to the first revolute joint coordinate in the ith limb $\{O_i\}$, of which the z-axis is coaxial to the first joint. Then the joint angles in each limb case can be computed as follows:

[$\underline{\text{R}}$R]S limb

This limb type is fully defined by a constant three Denavit-Hartenberg (DH) parameters (a_1, d_2, a_2). Given ${}^i\mathbf{p}_{s,i} = \begin{bmatrix} x_s & y_s & z_s \end{bmatrix}^T$, the five joint angles $(\theta_1, \theta_2, \theta_3, \theta_4, \theta_5)$ can be solved below

$$
\begin{aligned}
\cos\theta_2 &= \frac{x_s^2 + y_s^2 + z_s^2 - a_1^2 - a_2^2 - d_2^2}{2a_1a_2} := D \\
\theta_2 &= \arctan 2\left(\pm\sqrt{1 - D^2}, D\right) \\
\theta_1 &= \arctan 2\left(y_s, x_s\right) - \arctan 2\left(a_2\sin\theta_2, a_1 + a_2\cos\theta_2\right) \\
\theta_3 &= \arctan 2\left(r_{23}, r_{13}\right) - \theta_1 - \theta_2 \\
\theta_4 &= \arctan 2\left(r_{33}, \sqrt{1 - r_{33}^2}\right) + \frac{\pi}{2} \\
\theta_5 &= \arctan 2\left(-r_{32}, r_{31}\right)
\end{aligned}
\tag{3.14}
$$

where r_{ij} are the entries of the rotational matrix of the last joint coordinate frame with respect to the first rotary joint frame of the limb. Note that θ_1 and θ_2 are angles of the first actuated revolute joint ($\underline{\text{R}}$) and the passive revolute joint (R) in the planar subchain respectively, and θ_3, θ_4, and θ_5 are the three angles of the spherical joint (S).

[<u>R</u>RR]U limb

This limb type is defined by four constant DH parameters (a_1, a_2, d_3, a_3), and all the joint positions $(\theta_1, \theta_2, \theta_3, \theta_4, \theta_5)$ need to be solved in order to fully describe the twist system of this limb. Let $r_{m,n}$ denotes an element in the rotational matrix of the last rotational axis in the universal joint with respect the first revolute joint, defined by the DH convention, along with the position of the universal joint center ${}^{i}p_{u,i} = \begin{bmatrix} x_u & y_u & z_u \end{bmatrix}^T$ the joint angles are computed as the following steps:

$$
\begin{aligned}
&\text{Assuming, } \sin\theta_4 \geq 0, \\
&\theta_4 = \arctan 2\left(\sqrt{1 - r_{33}^2}, -r_{33}\right), \theta_5 = \arctan 2\left(-r_{32}, r_{31}\right) \\
&\theta_1 + \theta_2 + \theta_3 := \theta_{123} = \arctan 2\left(r_{23}, r_{13}\right) \\
&x_p = x_u - a_3\cos\theta_{123}, y_p = y_u - a_3\sin\theta_{123} \\
&\cos\theta_2 = \frac{x_p^2 + y_p^2 + z_u^2 - a_1^2 - a_2^2 - d_3^2}{2a_1a_2} := D \\
&\theta_2 = \arctan 2\left(\pm\sqrt{1 - D^2}, D\right) \\
&\theta_1 = \arctan 2\left(y_p, x_p\right) - \arctan 2\left(a_2\sin\theta_2, a_1 + a_2\cos\theta_2\right) \\
&\theta_3 = \theta_{123} - \theta_1 - \theta_2 \\
&\theta_4 = \arctan 2\left(\sqrt{1 - r_{33}^2}, r_{33}\right) \\
&\theta_5 = \arctan 2\left(-r_{32}, r_{31}\right).
\end{aligned}
\tag{3.15}
$$

Note that there are elbow down-up solutions $(+\theta_2, -\theta_2)$ in both kinds of the kinematic limbs. When computing the inverse kinematics of the full robot, the inverse kinematic solution of every limb must exist, otherwise that the desired platform pose is considered unfeasible.

3.4.5 Screw-based Jacobians

Forward Force-Moment Mapping

Assuming no joint friction and all rigid components, unique Jacobians of low-mobility parallel mechanisms can be obtained from methods proposed in [43, 72, 73, 74, 75]. The forward static force-moment relation, which maps the limb actuated joint torques $\boldsymbol{\tau} = \begin{bmatrix}\tau_1 & \tau_2 & \tau_3\end{bmatrix}^T$ to the platform output wrench ${}^b\$_{w,p} = \begin{bmatrix}\mathbf{f}^T & \mathbf{m}_b^T\end{bmatrix}^T$ with respect to the base coordinate frame $\{O_b\}$ and its origin, can be directly obtained as

$$ {}^b\$_{w,p} = \mathbf{J}_x^T \mathbf{J}_q^{-1} \boldsymbol{\tau} = \mathbf{J}_w \boldsymbol{\tau} \tag{3.16} $$

where

$$ \mathbf{J}_x^T = \begin{bmatrix} {}^b\hat{\$}_{w,ra,1} & {}^b\hat{\$}_{w,ra,2} & {}^b\hat{\$}_{w,ra,3} \end{bmatrix} \tag{3.17} $$

$$ \mathbf{J}_q = \mathrm{diag}\left({}^b\hat{\$}_{w,ra,1} \circ {}^b\hat{\$}_{t,a,1} \quad {}^b\hat{\$}_{w,ra,2} \circ {}^b\hat{\$}_{t,a,2} \quad {}^b\hat{\$}_{w,ra,3} \circ {}^b\hat{\$}_{t,a,3} \right). \tag{3.18} $$

${}^b\hat{\$}_{w,ra,i}$ is the unit wrench of the transmission wrench screw (TWS), which is reciprocal to all joint twists except the twist of the actuated joint in the ith limb or ${}^b\hat{\$}_{t,a,i}$. TWS is also reciprocal to the virtual twist screw of constraints ${}^b\hat{\$}_{t,c,i}$, obtained by normalizing the limb constraint ${}^b\hat{\$}_{w,c,i}$ in (3.4) based on the Plücker's ray coordinate form, i.e., normalizing the wrench screw by the norm of last three entries of the wrench. Hence, the basis of the TWS in each limb can be uniquely obtained by finding the left null space of a five-column matrix consisting of screws of the four passive joint twists and ${}^b\hat{\$}_{t,c,i}$, which again can be done carried out by using the *null* function in MATLAB®.

Note that the TWS of an [RR]S limb, with the first revolute joint actuated, is simply the zero-pitch wrench (pure force) that lies in the plane created by the spherical joint center and the axis of the second revolute joint. It also passes through the spherical joint center and is perpendicular to the joint axes of the [RR] subchain. In contrast, an [RRR]U chain has a finite-pitch TWS of which the axis lies on the plane created by two axes of the passive R-joints,

Forward Velocity Mapping

The forward velocity mapping from the limb actuated joint velocity $\dot{\mathbf{q}} = \begin{bmatrix} \dot{q}_1 & \dot{q}_2 & \dot{q}_3 \end{bmatrix}^T$ to the platform twist ${}^b\$_{t,p} = \begin{bmatrix} \boldsymbol{\omega}^T & \mathbf{v}_b^T \end{bmatrix}^T$, is explicitly obtained in [73] as follows:

$$ {}^b\$_{t,p} = \mathbf{J}_{rp}[\mathbf{r}]_p^{-1}\mathbf{J}_q\dot{\mathbf{q}} = \mathbf{J}_t\dot{\mathbf{q}} = \begin{bmatrix} \mathbf{J}_{t,\omega} \\ \mathbf{J}_{t,v} \end{bmatrix} \dot{\mathbf{q}} \tag{3.19} $$

where

$$ \mathbf{J}_{rp} = \begin{bmatrix} {}^b\hat{\$}_{t,rp,1} & {}^b\hat{\$}_{t,rp,2} & {}^b\hat{\$}_{t,rp,3} \end{bmatrix} \tag{3.20} $$

$$ \begin{aligned} [\mathbf{r}]_p &= \mathbf{J}_{rp}^T\mathbf{J}_x^T = \mathbf{J}_x\mathbf{J}_{rp} \\ &= \operatorname{diag}\left({}^b\hat{\$}_{w,ra,1} \circ {}^b\hat{\$}_{t,rp,1} \quad {}^b\hat{\$}_{w,ra,2} \circ {}^b\hat{\$}_{t,rp,2} \quad {}^b\hat{\$}_{w,ra,3} \circ {}^b\hat{\$}_{t,rp,3} \right). \end{aligned} \tag{3.21} $$

The columns screws ${}^b\hat{\$}_{t,rp,i}$ in $\mathbf{J}_{rp}$ are unit screws of the controllable end-effector twists, contributed by each of the actuated joints [73]. The screws are obtained from finding the left null space of the span of five column vectors of the three limb constraint wrenches and the other two TWS of the non-corresponding limbs. Note that the forward velocity Jacobian can also be obtained by using the method of the imaginary mechanism in [67]. In addition, note that the platform twists ${}^b\$_{t,p}$ with an equal angular velocity computed from 3.6 and 3.19 are identical.

3.5 Mechanism Optimization

Our optimization routine consists of two stages: stage (I) platform constraint synthesis, and stage (II) limb structural synthesis. The optimized parameters in the first stage determine the geometric constraints of the pelvic brace, which is independent of the parameters in the second stage. This strategy provides some flexibility to adjust the ranges of parameters corresponding to the results obtained from stage (I). Also, the performance among the limb types in stage (II) can be directly compared based on the same optimized "seed" parameter set from stage (I). The details of the overall optimization routine are illustrated in Fig. 3.5 and Fig. 3.6.

3.5.1 Stage (I): Platform Constraint Synthesis

The parameters in this stage determine the 3D planar surfaces in which the center positions of the spherical/universal joints lie. The 3D planar surface can be fully determined by three spherical coordinates $(\rho_i, \upsilon_i, \varphi_i)$ as the radial distance ρ_i, the azimuthal angle υ_i, and the zenith angle φ_i, respectively. Each of the three local joint attachment points on the pelvic brace is defined by three cylindrical coordinates $\left(\ell_{p,i}, \nu_{p,i}, z_{p,i}\right)$, corresponding to the radius $\ell_{p,i}$, the rotation angle around the z-axis $\nu_{p,i}$ and the z-axis position $z_{p,i}$, respectively: ${}^{p}\mathbf{b}_i = \begin{bmatrix} \ell_{p,i}\cos\nu_{p,i} & \ell_{p,i}\sin\nu_{p,i} & z_{p,i} \end{bmatrix}^T + {}^{p}\mathbf{b}_{i,o}$. Note that constant offsets of translation ${}^{p}\mathbf{b}_{i,o}$ are added to these surface and joint positions to create a bias for a preferred volumetric region relative to the wheelchair seat and the pelvic brace. The visualization of the feasible joint position on the pelvic brace and a representation of each of the three constraint planes (π_1, π_2, π_3) are shown in Fig. 3.5 (right). Note that the last axis of the universal joint in the [$\underline{\text{R}}$RR]U limb type is parallel to the local z-axis of the pelvic brace.

Four main cost functions are evaluated. We define the error distance between the pelvic brace coordinate frame of the human data and that of the platform inverse kinematic solution at the nth data point as

$$\varepsilon_{p,n} = \left\| {}^{b}\boldsymbol{\varepsilon}_{p,n} \right\| = \left\| {}^{b}\underline{\mathbf{p}}_{p,n} - {}^{b}\mathbf{p}_{p,n} \right\|. \tag{3.22}$$

The first three cost functions are

$$\begin{aligned}
&{}^{(\text{I})}_{1}C_{neutral} = \varepsilon_{p,1} && \text{(neutral pose distance error)} \\
&{}^{(\text{I})}_{2}C_{mean} = \tfrac{1}{N_w}\sum_{n=1}^{N_w}\varepsilon_{p,n} && \text{(mean distance error)} \\
&{}^{(\text{I})}_{3}C_{peak} = \max_{n\in\{1,2,\ldots,N_w\}}\left\{\varepsilon_{p,n}\right\} && \text{(peak distance error)} .
\end{aligned} \tag{3.23}$$

With a known unit twist ${}^{b}\hat{\$}_{t,p}$ of the constrained platform, computed and normalized from (3.6), the fourth cost function computes the average of the MVLC in (3.13) with a correction using the

position error vector in (3.22):

$$ {}^{(\mathrm{I})}_{4}C_{loss} = \frac{1}{N_s}\sum_{n=1}^{N_s}\left(\sqrt{\left(h_{t,p}-\underline{h}_{t,p}\right)^2+\left\|\left({}^{b}\mathbf{r}_{t,p}+{}^{b}\boldsymbol{\varepsilon}_{p}-{}^{b}\underline{\mathbf{r}}_{t,p}\right)\times{}^{b}\mathbf{s}_{t,p}\right\|^2}\right)_n . \tag{3.24} $$

This correction (ε-MVLC) is equivalent to translating the entire base (including the 3D planar constraint surfaces) of the robot until the pelvic braces from both cases are superimposed, which in turn assumes the identical posture of human subject in both conditions. The cost function has a length unit (m) or could also be weighted by $\omega_{p,n}$, resulting in a unit of power per magnitude of force (Watt/N) or normalized physical assistance power loss (NPAPL). In addition, constant saturation values ($\varepsilon_{p,n} = 1$ m) will be assigned to $\varepsilon_{p,n}$ and the nth corrected maximum virtual loss coefficient values if the inverse kinematic solution does not exist at the nth data point or when they simply exceed those saturation values.

A set of 67 homogeneous transformation matrices from movement data were selected. The first 25 poses ($N_w = 25$), including a static neutral configuration ($n = 1$), were used to evaluate the first three cost functions in (3.23), while the remaining 42 poses ($N_s = 42$) that have ISA data with selected positive and negative peak angular velocities from each of the sessions were used to compute ${}^{(\mathrm{I})}_{4}C_{loss}$ in (3.24). All poses and the ISA are visualized in Fig. 3.5 (left).

The Non-dominated Sorting Genetic Algorithm-II (NSGA-II) [76] was implemented to perform the multi-objective optimization to search for Pareto sets of parameters that minimize all four cost functions in (3.23) and (3.24). This selected optimization technique can be used with discontinuous objective functions. In addition, this evolutionary-based algorithm prevents solutions from getting stuck in local minima like the gradient based ones. The parameters were normalized to within the range of 0 to 1 and were encoded into a chromosome of 1D array, representing an individual. Every individual/chromosome always has the same size of 18 normalized values (6 parameters per limb). An upper threshold of $\varepsilon_{p,1} < 0.025$ m was used for screening the randomized individuals during the initialization.

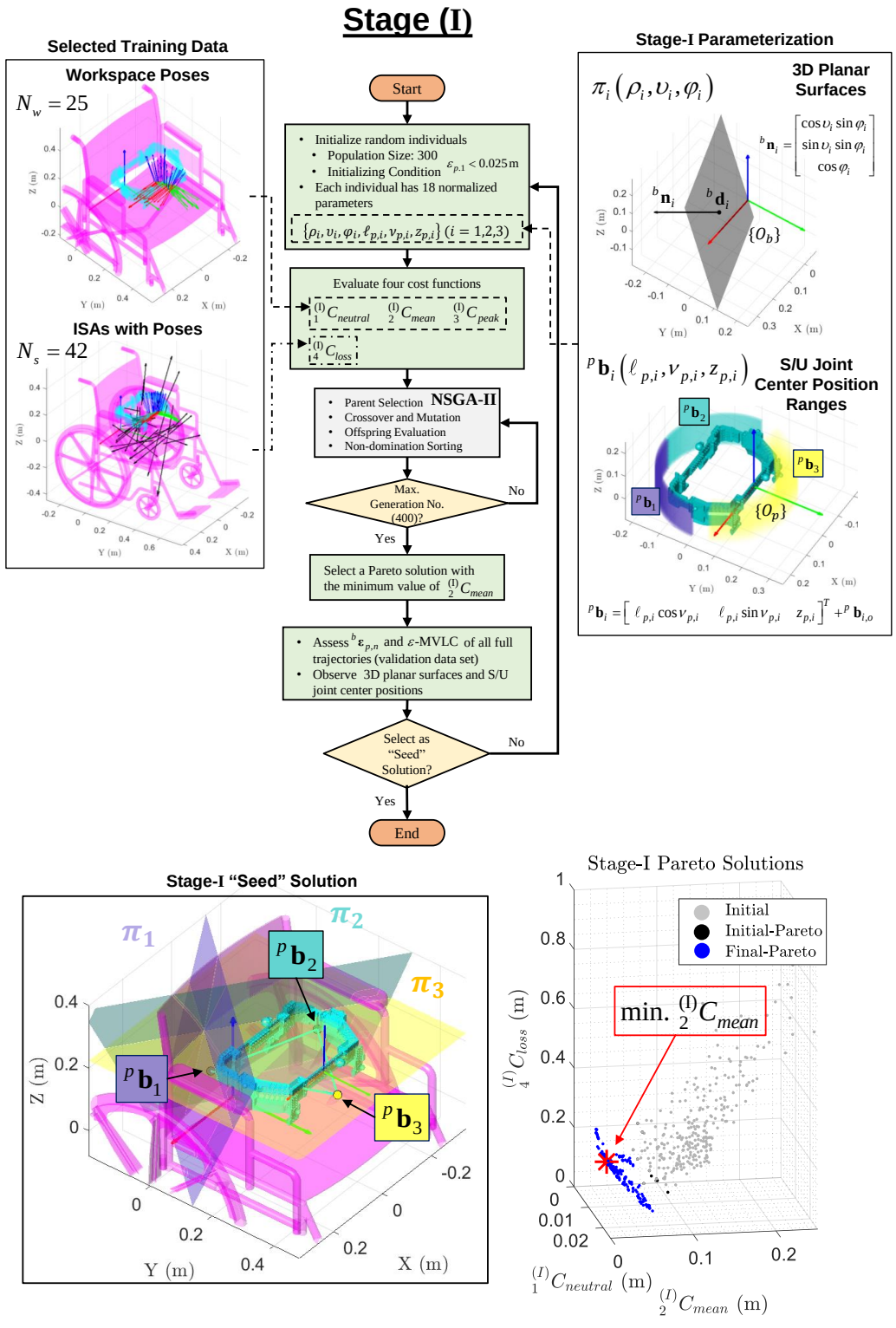

Figure 3.5: Flow chart of the multi-objective optimization (MOO) stage (I). Note that in the plot of Stage-I Pareto Solutions, all individuals in the final generation are non-dominated (Pareto) solutions.

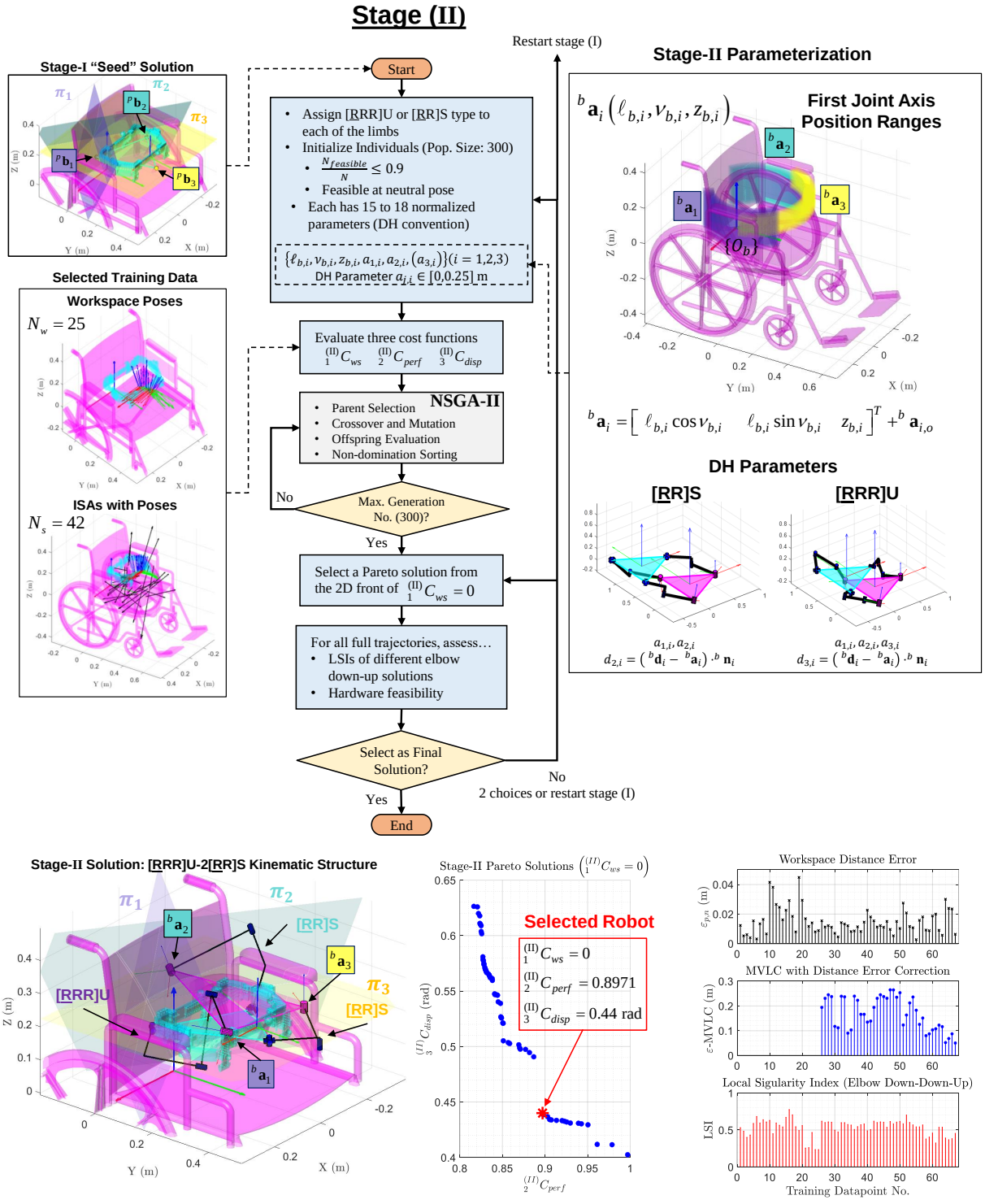

Figure 3.6: Flow chart of the multi-objective optimization (MOO) stage (II).

3.5.2 Stage (II): Limb Structural Synthesis

In this stage, we search for remaining parameters required to complete the robot design. The first nine genes in each of the chromosomes indicate the values of the cylindrical coordinates $\left(\ell_{b,i}, \nu_{b,i}, z_{b,i}\right)$ (three genes for each limb) which are used to compute a fixed point that the first joint axis passes through as ${}^{b}\mathbf{a}_i = \begin{bmatrix} \ell_{b,i}\cos\nu_{b,i} & \ell_{b,i}\sin\nu_{b,i} & z_{b,i} \end{bmatrix}^T + {}^{b}\mathbf{a}_{i,o}$ in the feasible region of joint positions in the same manner as that of the spherical/universal joint positions on the pelvic brace, as shown in Fig. 3.6. The limb inverse kinematics in section 3.4.4 for obtaining joint angles in each limb case can be computed by using three DH parameters of the [$\underline{\text{R}}$R]S type $\left(a_{1,i}, d_{2,i}, a_{2,i}\right)$ or four parameters for the [$\underline{\text{R}}$RR]U limb type $\left(a_{1,i}, a_{2,i}, d_{3,i}, a_{3,i}\right)$. Note that the DH parameter $d_{2/3,i}$ is calculated from the selected first joint position ${}^{b}\mathbf{a}_i$ in stage (II), the position ${}^{b}\mathbf{d}_i$ and the normal vector ${}^{b}\mathbf{n}_i$ of the planar surface from the stage-I "seed" solution: $d_{2/3,i} = \left({}^{b}\mathbf{d}_i - {}^{b}\mathbf{a}_i\right) \cdot {}^{b}\mathbf{n}_i$.

Three cost functions were implemented. First, in order to preserve the workspace achieved by the "seed" solution in stage (I), we use the cost function that calculates the ratio of the number of feasible poses to the total number of poses ($N = N_w + N_s$):

$$ {}^{(\text{II})}_{1}C_{ws} = 1 - \frac{N_{feasible}}{N}. \tag{3.25} $$

The second cost function regulates the mechanism performance by using the local singularity index (LSI) [77]:

$$ {}^{(\text{II})}_{2}C_{perf} = 1 - \min_{m,n}\left\{\sigma_{local,m,n}\right\}, \tag{3.26} $$

where $\sigma_{local} = \min\{\eta_{in}, \eta_{out}, \eta_{const}\}$, $\sigma_{local} \in [0, 1]$; the input transmission index (ITI) η_{in}, output transmission index (OTI) η_{out}, and constraint transmission index (CTI) η_{const} are obtained from [77, 78, 79] (see Appendix C). When the mechanism approaches a singularity condition, the LSI becomes closer to zero. m represents a case among all eight combinations ($m = 1, 2, ..., 8$) of elbow down-up solutions at the feasible nth data point $\left(n = 1, 2, ..., N_{feasible}\right)$.

Finally, the third cost function is used to limit the magnitude of three actuated joint displacements $\mathbf{q}_n = \begin{bmatrix} q_1 & q_2 & q_3 \end{bmatrix}^T$ relative to the neutral configuration by finding the maximum value, among the eight elbow down-up cases, of the average of $\left\|\mathbf{q}_{n,m}\right\|$ across the feasible poses:

$$ {}^{(\mathrm{II})}_{3}C_{disp} = \max_{m} \left\{ \frac{1}{N_{feasible}} \sum_{n=1}^{N_{feasible}} \left\|\mathbf{q}_{n,m}\right\| \right\}. \tag{3.27} $$

The normalized parameters in this stage correspond to first revolute joint locations ${}^{b}\mathbf{a}_i$ and the linkage dimensions based on the DH parameters. Since the parameter $d_{2,i}$ for [$\underline{\mathrm{R}}$R]S or $d_{3,i}$ for [$\underline{\mathrm{R}}$RR]U is fully defined from the 3D plane and ${}^{b}\mathbf{a}_i$, only two additional values for $\left(a_{1,i}, a_{2,i}\right)$ of [$\underline{\mathrm{R}}$R]S or three values for $\left(a_{1,i}, a_{2,i}, a_{3,i}\right)$ of [$\underline{\mathrm{R}}$RR]U are added to the chromosome. Hence, the chromosome size in each run of the stage (II) varies from 9 + 2 + 2 + 2 = 15 to 9 + 3 + 3 + 3 = 18, depending on a selected limb combination. Individuals who have $\frac{N_{feasible}}{N} \leq 0.9$ or are not feasible in the neutral configuration were rejected during the initialization. A set of saturation values for the three cost functions $\left(1, 1, 2\sqrt{3}\pi\right)$ were also assigned to these individuals during the evaluation steps in every generation. The final Pareto solutions which have zero value of ${}^{(\mathrm{II})}_{1}C_{ws}$ were assessed with the validation data set (All full trajectories of the 20 Movement sessions) to obtain the optimized full robot structure. Then a few Pareto solutions with largest crowding distances (tend to include solutions at the edges of the Pareto front) in the 2D axes of the two remaining objectives $\left({}^{(\mathrm{II})}_{2}C_{perf} \text{ and } {}^{(\mathrm{II})}_{3}C_{disp}\right)$ were selected to be assessed with the validation data set (All full trajectories at 1/100 down sampling rate from the processed data).

Additional considerations for choosing the final mechanism include the location of the first actuated joints, the range of the actuated joint displacements, the linkage dimensions, occurrences of linkage toggle positions in the validation trajectories, and the overall values of LSI corresponding to the selected elbow down-up case that tends to minimize the hardware interference.

3.5.3 Optimized Solution

The optimization stage (I) was run multiple times for 400 generations each, with a population size of 300. Individuals in the Pareto front with smallest ${}^{(\mathrm{I})}_{2}C_{mean}$ values from different runs were selected. Then we observed the distance error in (3.22) and the ε-MVLC from (3.24) in each of the data points from the validation data set. After that, a few best chromosomes from the stage (I) were selected to be used s the "seed" in the next stage.

After we obtained the "seed" solutions from stage (I), we ran the stage (II) using each of the "seed" solutions for 300 generations long with the population size of 300 for a few times. We started with only the two symmetrical cases, namely, 3-[R̲R]S and 3-[R̲RR]U. After some assessment with the validation data set, we found that the overall performance of the 3-[R̲RR]U solutions in terms of the workspace and the LSIs in the validation trajectories is superior to those of the 3-[R̲R]S solutions, within the same "seed". For example, many 3-[R̲R]S solutions are not capable of providing full ROM during the contralateral reaching at knee level and tend to approach singularities earlier than the [R̲RR]U. However, a greater number of linkages is less desirable due to a small area on the wheelchair. Through observations across a few "seed" solutions, the endpoint workspace of the first limb (π_1 in Fig. 3.5, for example) seemed to have larger joint displacements than other limbs due to the twist-and-bend motion during a contralateral reaching. Therefore, we hypothesized that the [R̲RR]U-2[R̲R]S combination would be a good design compromise since the dexterity provided by the [R̲RR]U limb in the plane π_1 can help maintain good workspace and prevent the LSI from dropping too sharply at extreme positions while the footprint of the mechanism can be kept small.

An optimized mechanism with the [R̲RR]U-2[R̲R]S architecture was selected as shown in Fig. 3.6 (bottom left). The optimized parameters of the planar constraints and the joint positions are shown in Table 3.2, and the optimized DH parameters of the linkages are shown in Table 3.3. The [R̲RR]U limb was assigned to the first 3D plane π_1, which requires larger joint displacements than other limbs due to the twist-and-bend pelvic motion during contralateral reaching. The overall performance of our optimized mechanism with training data points is shown in Fig. 3.6 (bottom right), and some validation trajectories are shown in Fig. 3.7. The selected mechanism can achieve

Table 3.2: Optimized parameters of pelvic WRAPS

Stage (I): Platform Constraint Synthesis

Type	Parameter	Chain 1	Chain 2	Chain 3
3D Planar Surface	υ_i (rad)	-0.724724	-2.191696	-2.148428
	φ_i (rad)	1.295605	1.266729	0.007779
	ρ_i (m)	0.198399	0.146819	0.224010
Pelvic Joint Position ${}^{p}\mathbf{b}_i$	$\nu_{p,i}$ (rad)	-0.720094	3.511378	1.259345
	$z_{p,i}$ (m)	-0.022275	-0.073172	0.011034
	$\ell_{p,i}$ (m)	0.210283	0.217734	0.204406
Pelvic Joint Position Offset ${}^{p}\mathbf{b}_{i,o}$	$b_{i,o,x}$ (m)	0	0	0
	$b_{i,o,y}$ (m)	-0.1	-0.1	-0.1
	$b_{i,o,z}$ (m)	0	0	0

Stage (II): Limb Structural Synthesis

Type	Parameter	Chain 1	Chain 2	Chain 3
Base Joint Position ${}^{b}\mathbf{a}_i$	$\nu_{b,i}$ (rad)	1.002358	4.188312	2.386030
	$z_{b,i}$ (m)	0.239877	0.228948	0.204034
	$\ell_{b,i}$ (m)	0.211273	0.242377	0.281040
Base Joint Position Offset ${}^{b}\mathbf{a}_{i,o}$	$a_{i,o,x}$ (m)	0	0	0
	$a_{i,o,y}$ (m)	0.1	0.1	0.1
	$a_{i,o,z}$ (m)	0	0	0

all orientations throughout trajectories of the 20 sessions. The LSI values remain high throughout most of the trajectories. Note that we still allowed some reduction of LSI values to be closer to zero, as seen by the two minimum peaks of LSI (≈ 0.024) during the contralateral reaching at knee level, since the corresponding elbow down-up solution of the [$\underline{\text{R}}$RR]U limb provides the most feasible hardware design. Actuated joint displacements and velocities, angular velocities of the pelvic brace are within reasonable limits. In the third row of the plots, ε-MVLC values weighted by the magnitude of the angular velocities (or NPAPL) are kept under 0.1 Watt/N. The optimization routine was run in MATLAB® scripts (CPU: Intel Xeon E3-1230 V5 3.4GHz Quad-Core Processor); runtimes for the final solution are 3,096 seconds in stage (I) and 96,535 seconds in stage (II).

Table 3.3: Optimized Denavit–Hartenberg (DH) parameters of pelvic WRAPS

Chain 1: [R̲RR]U

Link i	θ_i (rad)	d_i (m)	a_i (m)	α_i (rad)
1	θ_1	0	0.249932	0
2	θ_2	0	0.203863	0
3	θ_3	0.164864	0.084980	$\pi/2$
4	θ_4	0	0	$\pi/2$
5	θ_5	0	0	0

Chain 2: [R̲R]S

Link i	θ_i (rad)	d_i (m)	a_i (m)	α_i (rad)
1	θ_1	0	0.248816	0
2	θ_2	-0.151904	0.160056	0
3	θ_3	0	0	$\pi/2$
4	θ_4	0	0	$\pi/2$
5	θ_5	0	0	0

Chain 3: [R̲R]S

Link i	θ_i (rad)	d_i (m)	a_i (m)	α_i (rad)
1	θ_1	0	0.250000	0
2	θ_2	0.020369	0.139779	0
3	θ_3	0	0	$\pi/2$
4	θ_4	0	0	$\pi/2$
5	θ_5	0	0	0

3.6 Hardware Realization

A CAD of WRAPS pelvic mechanism prototype with a user and its kinematic model is shown in Fig. 3.8 and the real hardware configuration with a human subject is shown in Fig. 3.9. The robot structure is mounted on a custom-made bench. The axes of the actuated revolute joints (R̲) are fixed relative to the bench coordinate frame $\{O_b\}$. The moving coordinate frame $\{O_p\}$ is rigidly attached to the pelvic brace. The positions of the universal joint center (U) of chain 1 and the spherical joint centers (S) of chain 2 and 3 on the pelvic brace are fixed relative to $\{O_p\}$. The actuated joints (R̲) are driven by three maxon permanent magnet blushless DC motors with Hall sensors (EC60 647692,

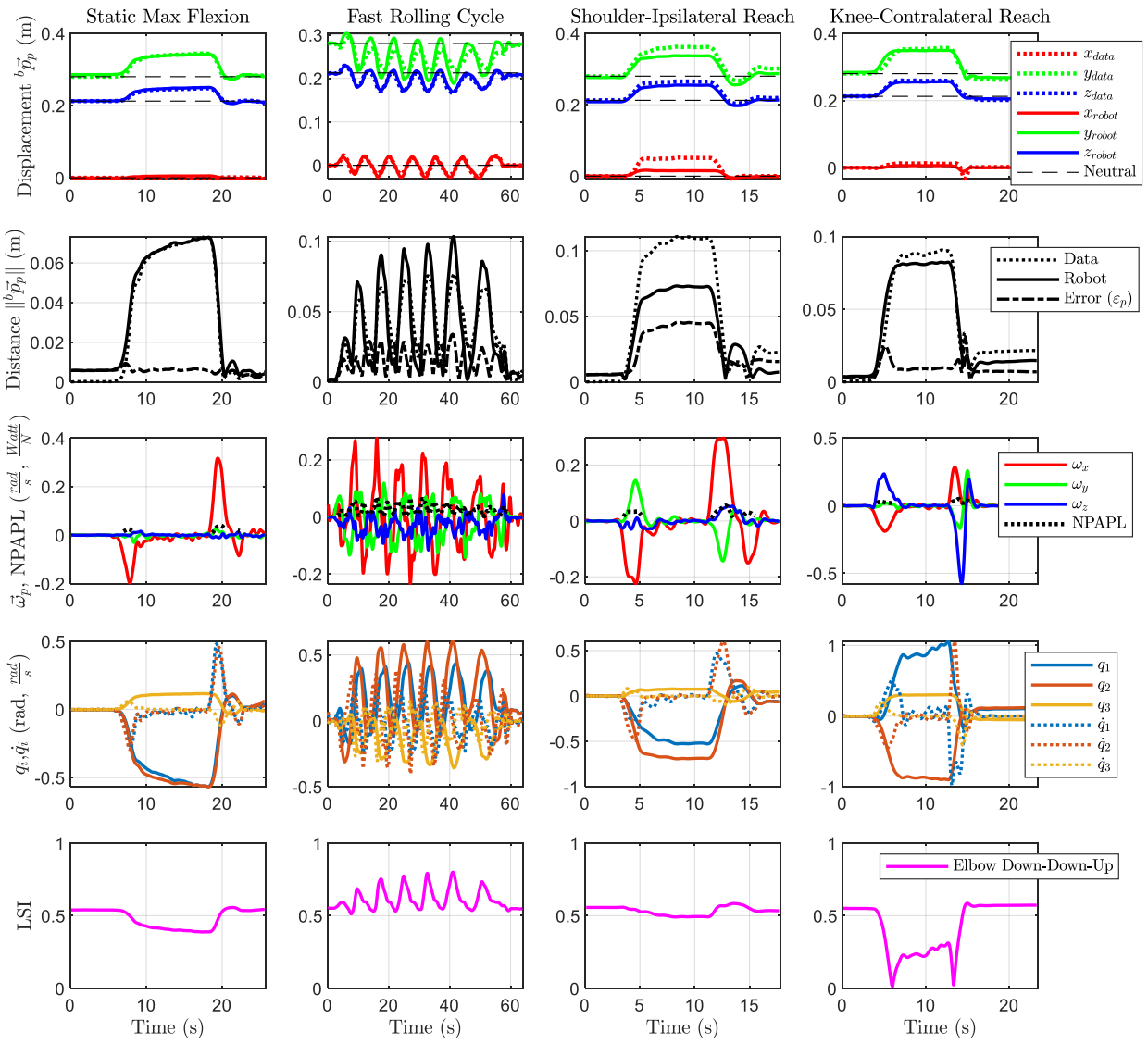

Figure 3.7: Validation trajectories of the selected four sessions.

maxon precision motors, Taunton, MA, USA) which are connected to the rotary shafts mounted on the fixed bearings on the bench frame. Each motor has a built-in encoder (MILE 421988) with 4,096 counts per turn (CPT), and a Ø52 mm planetary gearhead (GP 52 C 223095) with a gear ratio of 113:1 with 30 N-m maximum output torque. The robot linkages consist of CNC-machined aluminum parts, ABS 3D printed parts (Ultimaker S5, Ultimaker, Framingham, MA, USA), and off-the-shelf rotary bearings and ball joints. In order to accommodate different subject sizes, linkage dimensions can also be adjusted by arrays of clearance holes on some machined aluminum plates. In addition, four rotary quadrature incremental encoders with 3,600 pulses per revolution (CALT

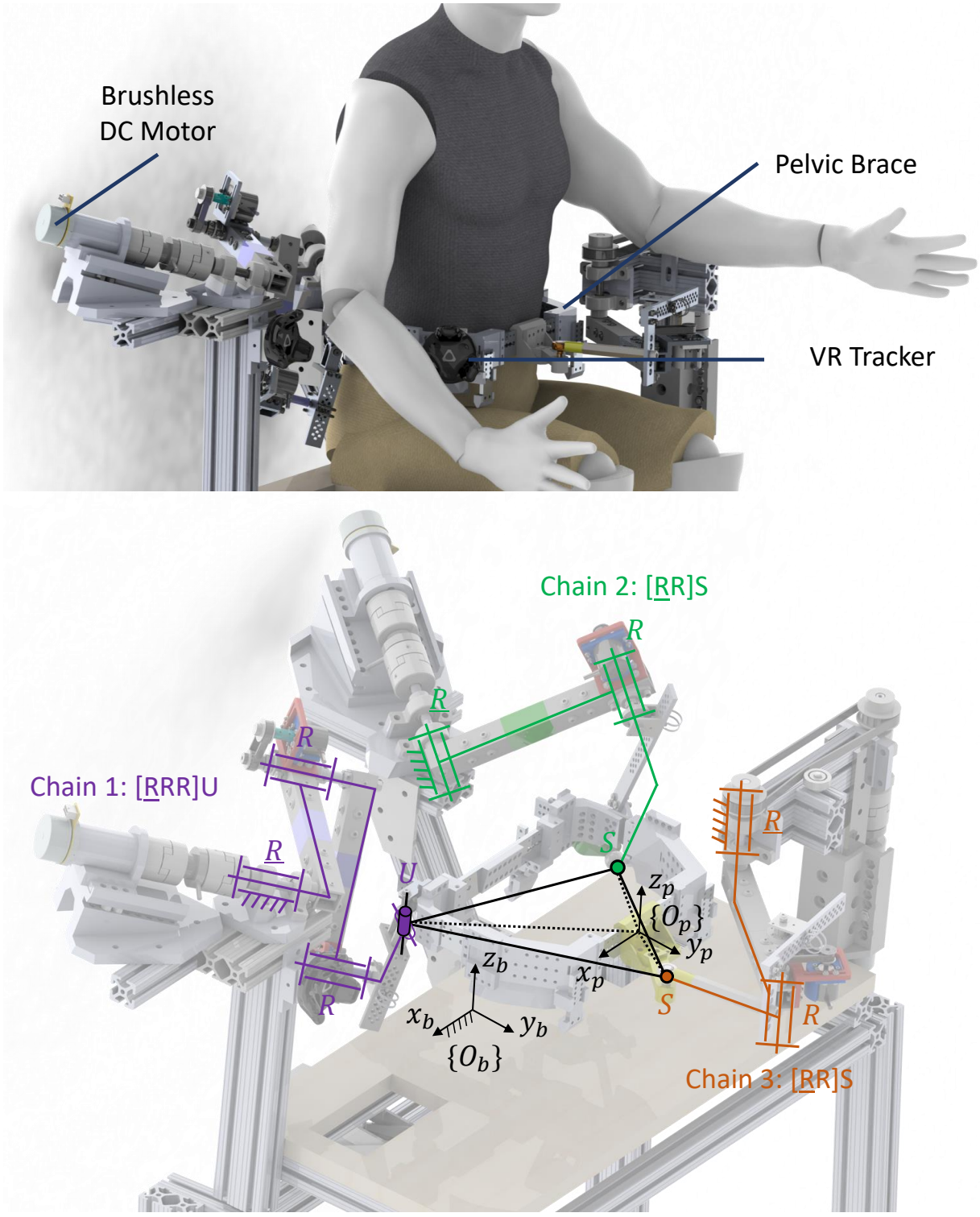

Figure 3.8: CAD Model of pelvic WRAPS prototype with kinematic model of [RRR]U-2[RR]S architecture.

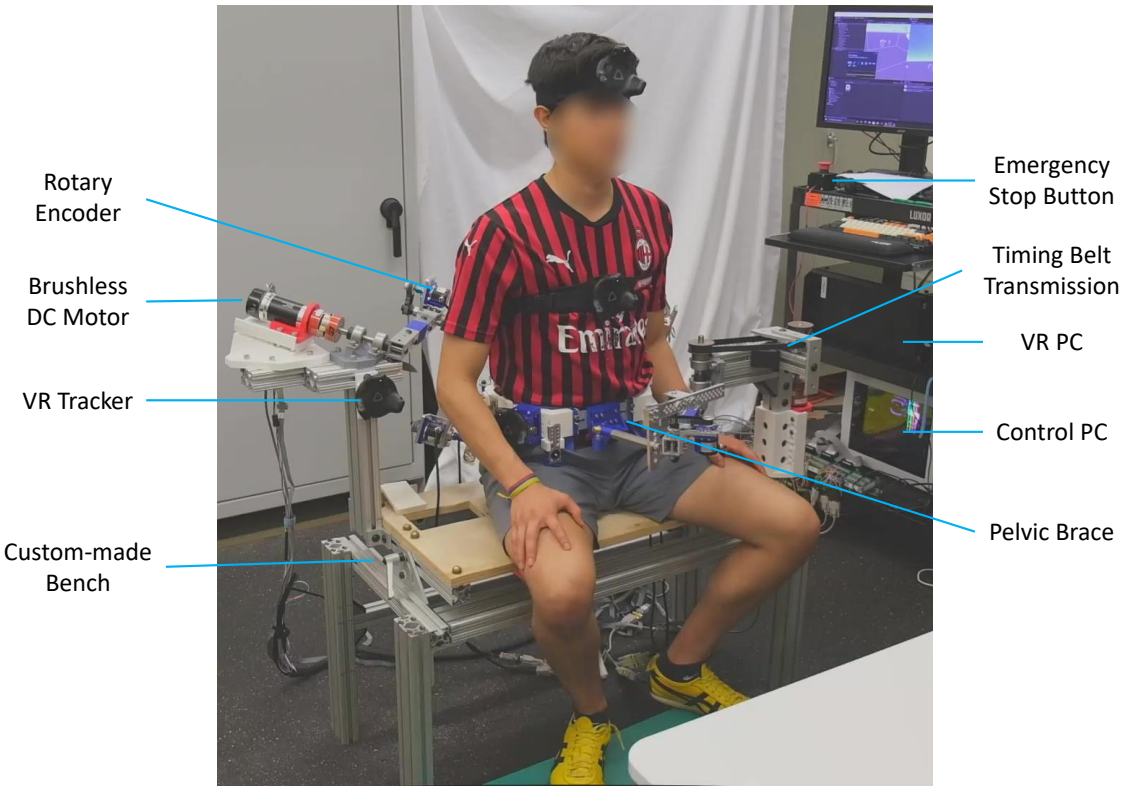

Figure 3.9: Pelvic WRAPS hardware with a subject

GHS38-06G3600BML5, Shanghai QIYI Electrical & Mechanical Equipment, Baoshan District, Shanghai, China) are connected to the passive revolute joints (R) in order to simplify the forward kinematic computation, by which all the center positions of the universal joint (U) and the spherical joints (S) can be calculated directly from the seven encoder readings, therefore the position and orientation of $\{O_p\}$ with respect to $\{O_b\}$ can be estimated by the least-squares rigid motion using SVD in [64] by using the three positions of the last joints of the three kinematic limbs.

3.6.1 Control System

The overview of the control system is shown in Fig. 3.10. Hardware interfaces between the sensors and the control PC (Ubuntu 16.04.7 LTS, Xenial Xerus) are carried out by using two Sensoray 826 PCI express analog and digital I/O data acquisition (DAQ) cards (Sensoray Co., Inc., Tigard, OR, USA). One of the DAQ card is connected to three ESCON 70/10, 4-Q Servo Controllers (maxon precision motors, Taunton, MA, USA). The servo controllers are powered by a

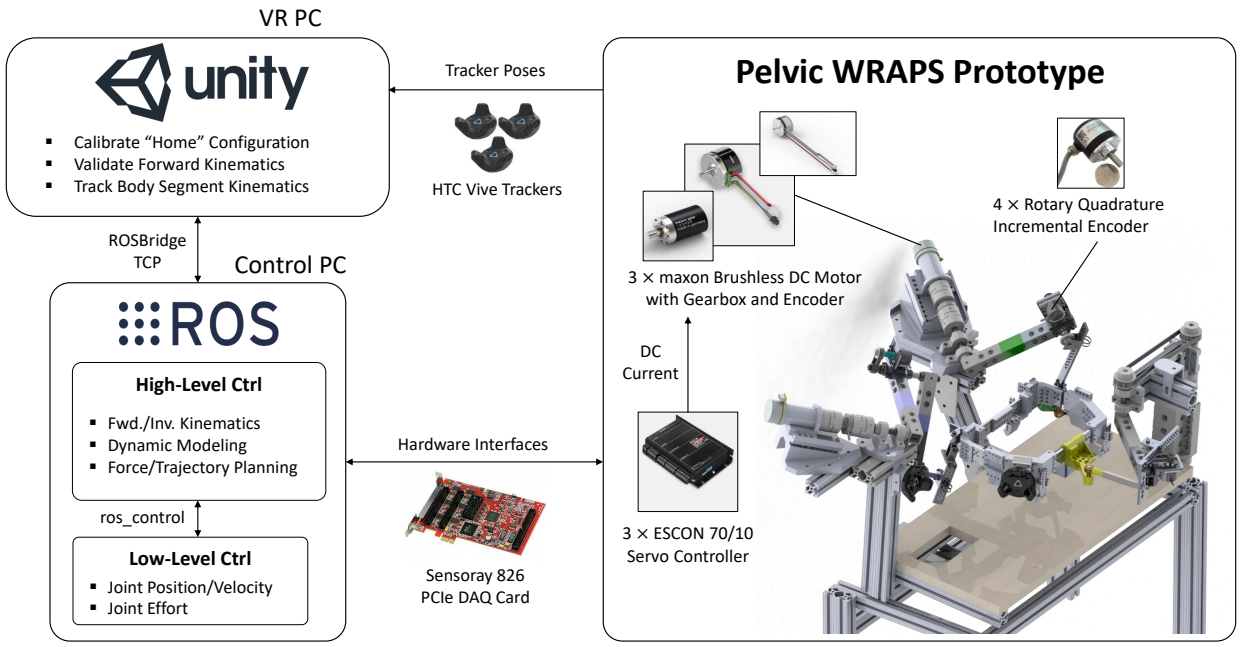

Figure 3.10: Control system overview of pelvic WRAPS

48 VDC power supply. Each of the servo controller is configured by the ESCON Studio Software (ver 2.2) to receive enable/disable digital signal from a DIO pin of the DAQ card and to receive an analog set value (-10 to 10 VDC) from the DAQ card to regulate the current/torque (-2.5 to 2.5 A : -31.82 to 31.83 N-m at the gearbox shaft) of the DC motor. In addition, the DAQ board receives two the differential analog signals from the servo controller (-4.0 to 4.0 VDC), which indicates the actual current/torque and the actual speed of the motor output shaft (-5.58 to 5.58 rad/s at the gearbox shaft). In addition, seven counter channels on the DAQ cards receive pulse signals from the incremental encoders of the three maxon motors and the four passive rovolute joints. The pulse values are converted to angular displacements of the joint shafts in radians.

The robot controller is implemented by an open-source Robot Operating System[1] (ROS, version Kinetic Kame) [80], written in C++ and python programming languages. A schematic of ROS nodes and messages in the WRAPS control system is presented in Fig. 3.11. The "/encoder_reading" node receives encoder positions relative to the robot home configuration (where all the encoder readings

[1]https://www.ros.org: The Robot Operating System (ROS) is a flexible framework for writing robot software. It is a collection of tools, libraries, and conventions that aim to simplify the task of creating complex and robust robot behavior across a wide variety of robotic platforms.

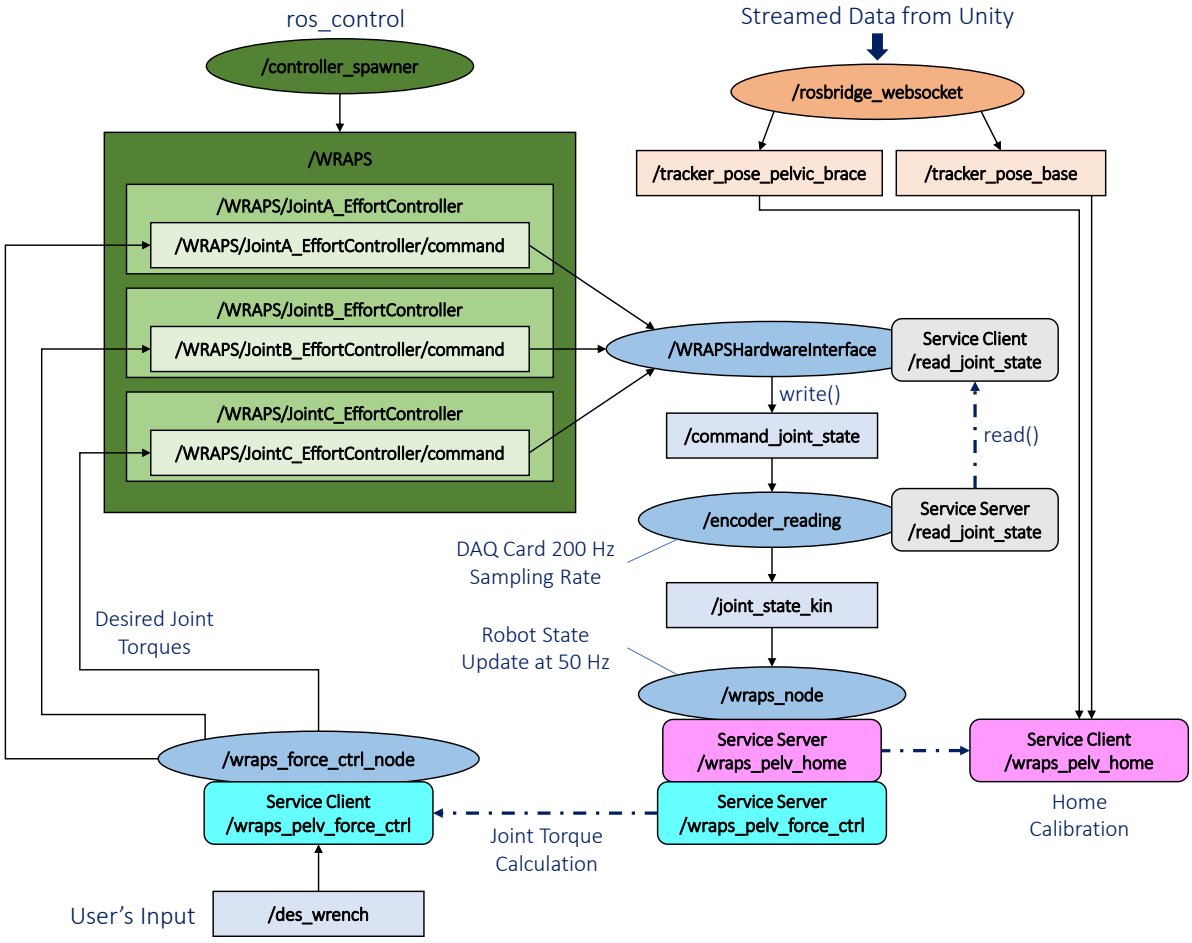

Figure 3.11: ROS node graph of pelvic WRAPS control system. A ROS node is represented by an ellipse with the node name while a ROS message is represented by a rectangular box with its topic name. The arrows indicate the publish-to-subscribe communication direction between the nodes. Service servers and clients are represented by rectangular boxes with round edges.

are zero values) from the DAQ card at the 200 Hz sampling rate and publishes the JointState[2] message named "/joint_state_kin", which is subscribed by the "/wraps_node" that performs the forward kinematic computation to register the current configuration of the robot at 50 Hz.

The high-level controller (force or position control mode) is implemented in a ROS node, by which the node will request a service from the "/wraps_node" to calculate the desired joint torques or joint angles and then send those commands to the low-level controller implemented by the

[2]sensor_msgs/JointState.msg: A message that holds data to describe the state of a set of torque controlled joints.

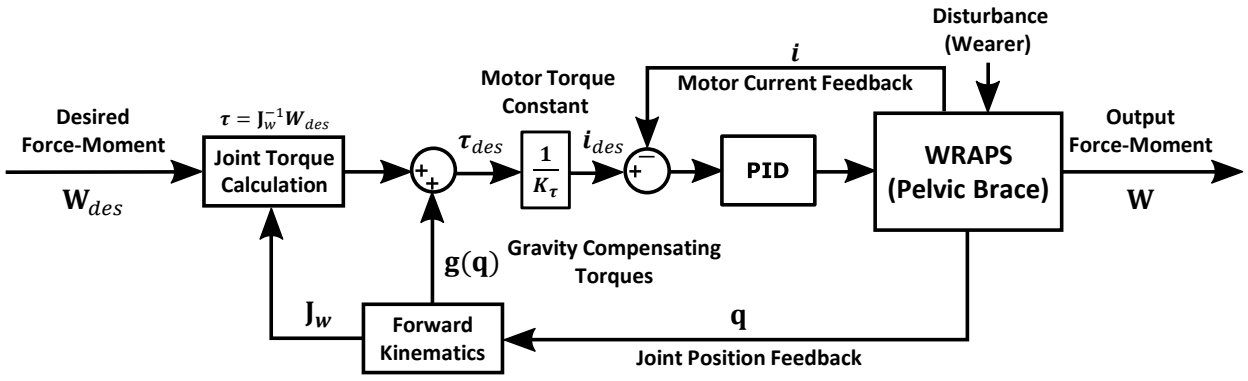

Figure 3.12: Force controller of pelvic WRAPS with gravity compensation

ros_control framework [81].

The position controller of the pelvic WRAPS is in the same manner as that of the WRAPS the for upper trunk segment in Fig. 2.10, whereas the force controller of the pelvic WRAPS sends the feed-forward torque/current commands to the ESCON servo controllers with the built-in closed-loop controllers of the motor currents, as shown in Fig. 3.12. A forward-backward Newton-Euler inverse dynamics algorithm [82] is implemented to estimate motor torques required to compensate the weights of the linkages in each limb throughout the workspace of the pelvic WRAPS. Note that since the robot has 3 DOFs, only three rows from the force-moment mapping Jacobian (either force or moment component) are selected for the joint torque calculation.

In the ros_control framework, the "/controller_spawner" node can be configured to implement either feed-forward joint effort commands to the motors, used in the force control mode, or joint effort commands based on the closed-loop PID control law, used in the position control mode.

To illustrate, the node graph in Fig. 3.11 represents an end-effector force control mode, where a setpoint value of Wrench[3] with the topic named "/des_wrench" is a direct user's input. This message is then subscribed by the "/wraps_force_ctrl_node", which in turn requests for a joint torque calculation service by the "/wraps_node". Then the "/wraps_force_ctrl_node" will publish the desired torque values to the "/WRAPSHardwareInterface" node. This low-level control node obtains the current joint state (measured by the data acquisition card) through the "/read_joint_state" service

[3]geometry_msgs/Wrench.msg: This represents force in free space, separated into its linear and angular parts.

by calling the read() function in the node, and calculates the command "/command_joint_state", sent to the "/encoder_reading" node by the write() function. Finally, the "/encoder_reading" node sends the effort commands as input DC voltages through the digital-to-analog (DAC) converter of the DAQ card to the ESCON servo controllers.

The control PC also communicates with the virtual reality (VR) Windows PC which is connected to a HTC Vive VR headset, base stations, controllers, and trackers (HTC, Taoyuan, Taiwan). The tracker positions and orientations (poses) are streamed to the control PC in real-time by using the rosbridge TCP communication protocol, developed in the ROS# (ros-sharp) package (Siemens AG, Munich, Germany), running in Unity Real-Time Development Platform (version 2020.3.2f1, Unity Technologies, San Francisco, CA, US). In Fig. 3.11, the "/rosbridge_websocket" node receives the streamed tracker data from the VR PC and publishes PoseStamped[4] messages, named as "/tracker_pose_base" and "/tracker_pose_pelvic_brace", representing coordinate frames of the Vive trackers attached to the base and the pelvic brace, respectively, as shown in the CAD model of Fig. 3.10. The streamed tracker poses on the bench and the pelvic brace are essential for calibrating the home configuration of the pelvic WRAPS, namely the transformation matrix of the pelvic brace coordinate frame $\{O_p\}$ from the bench coordinate frame $\{O_b\}$, where all the encoder readings are at zero positions. To set a home configuration, when the pelvic brace is moved to a desired position, a rotational matrix ${}^{b}\mathbf{R}_{p}$ of the pelvic brace frame $\{O_p\}$ with respect to the frame $\{O_b\}$ are calculated from the current poses of the two trackers. Next, the obtained rotational matrix is used to calculate all the absolute joint angles by the inverse kinematics, and the joint values are stored in the "/wraps_node" as the home absolute joint angles corresponding to a transformation matrix of the pelvic brace in the 3D space measured from the Vive trackers. This home calibration is done by calling "/wraps_pelv_home" service in Fig. 3.11. While the "/wraps_node" is running, the non-zero readings from the encoders in the message "/joint_state_kin" is added to the home absolute joint angles to get the current absolute joint angles, which in turn will be used to calculate the forward kinematics in real-time.

[4]geometry_msgs/PoseStamped Message: A Pose (position and orientation) with timestamp

Table 3.4: Seated movements in the pelvic WRAPS experiment

No.	Movement Description
1-6	Move the torso to perceived extreme ROM in a plane of motion (sagittal plane: flexion-extension, frontal plane: right/left lateral bending, and transverse plane: right/left axial rotation) while still maintaining stability. Pause for 2-3 seconds then return to the neutral position.
7-9	Six cycles between the extreme ROM in each of the three planes of motion. The motions were paced by a metronome at 120 beats/sec, four beats long between the neutral to an extreme position.
10	Six cycles of rolling the torso around the vertical axis in the counter clockwise (CCW) direction, paced by a metronome at 120 beats/sec. Each quadrant of a cycle was four beats long.

3.7 Human Evaluation

The pelvic WRAPS prototype was evaluated with able-bodied subjects to

1. validate the forward kinematics computation againts the actual pelvic brace position in the space measured by the VR trackers, and

2. to characterize the pelvic range of motion (pROM) when wearing the pelvic WRAPS in the transparent mode compared to pROM when the pelvic brace is not attached to the mechanism ("free" condition).

3.7.1 Experimental Protocol

The experiment was approved by the Institutional Review Board (IRB) of Columbia University (Protocol No. AAAR7388). Seven able-bodied adult subjects (4 males and 3 females) participated in the study with an average age of 24 years old (SD = 4.8 yr., range: 18 - 32 y/o.), 68.1 kg average weight (SD = 13.4 kg, range: 45.5 - 86.4 kg), 172.7 cm average height (SD = 10.1 cm, range: 155 -

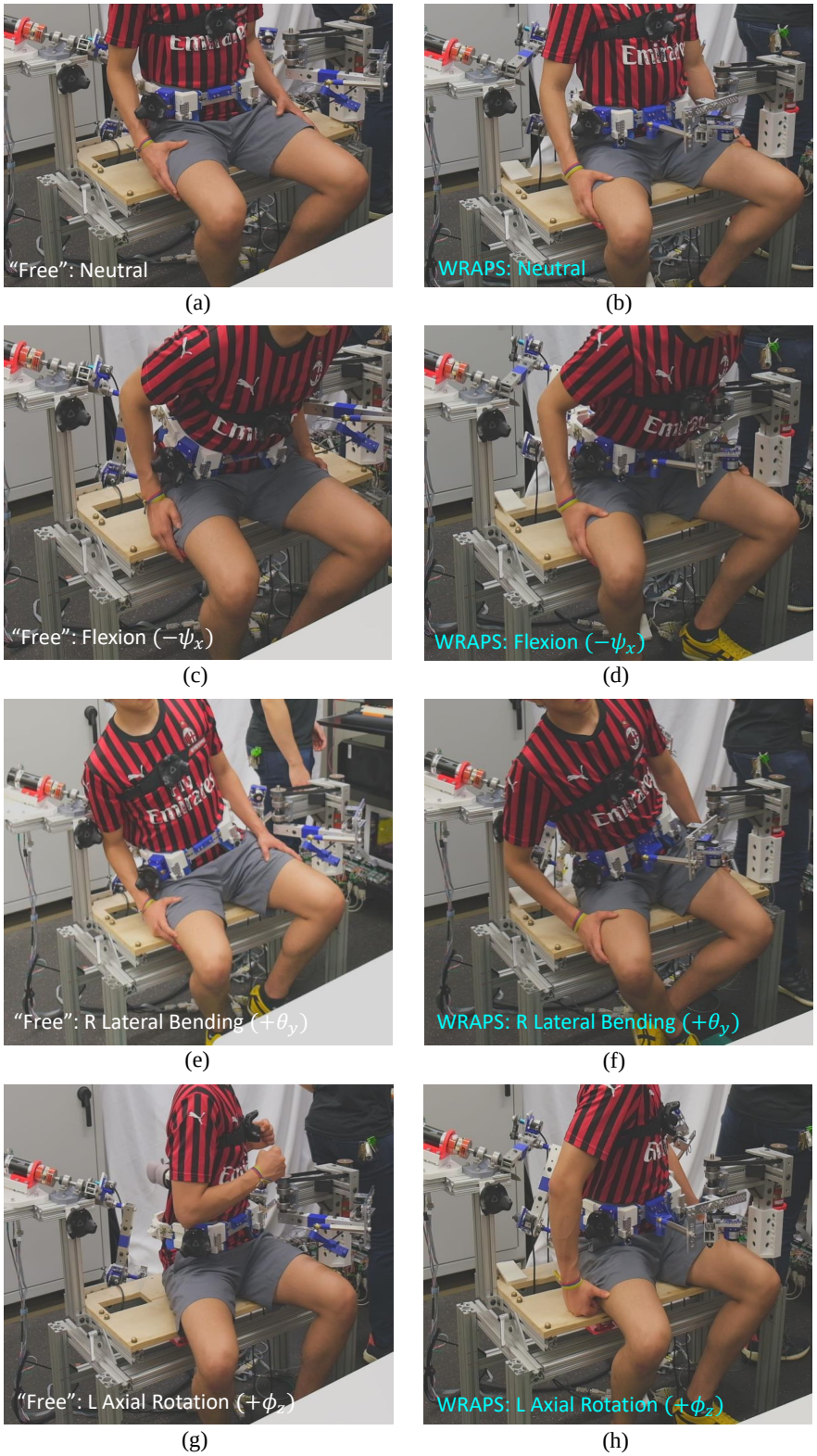

Figure 3.13: A subject performs different seated movements while wearing the pelvic brace in "free" and WRAPS conditions

Table 3.5: Group Average %ROM of pelvic WRAPS compared to "free" condition

	Flexion ($-\psi_x$)	Extension ($+\psi_x$)	R Lateral Bending ($+\theta_y$)	L Lateral Bending ($-\theta_y$)	Right Axial Rotation ($-\phi_z$)	Left Axial Rotation ($+\phi_z$)
MEAN	36.19%	33.05%	85.35%	87.44%	73.96%	63.51%
SD	17.48%	12.01%	33.05%	10.78%	24.59%	18.72%

184 cm), and 50.6 cm average torso height (SD = 7.2 cm, range: 39.4 - 61.0 cm) measured from the greater trochanter level to the suprasternal notch. The recruited subjects were within the adjustable range of the WRAPS pelvic brace sizes.

The subjects performed the same set of torso movements while wearing the pelvic brace with and without the mechanism being attached to it (no thoracic brace attached to the upper trunk). The movements are described in Table 3.4. The first six movements are static single plane ROM. The next three movements are the cyclical motions in each of the planes[5]. Finally, movement No. 10 is a continuous rolling around the vertical axis in the counter-clockwise (CCW) direction, which is a combination of motion in different planes. In the pelvic WRAPS condition, the robot is controlled in the transparent mode ($\mathbf{W}_{des} = \mathbf{0}$) with feed-forward gravity compensation torques to the motors.

The "free" and the WRAPS conditions at neutral configurations are shown in Fig. 3.13 (a) and (b) respectively. along with a flexion motion in Fig. 3.13 (b). Some selected motions in different planes were performed by a subject in both of the conditions, shown in Fig. 3.13: flexion (sagittal plane) in (c) and (d); right lateral bending (frontal plane) in (e) and (f), and left axial rotation (transverse plane) in (g) and (h). The position and orientation of the pelvic brace was recorded by an attached VR tracker (100 Hz). Additionally, forward kinematic solutions of the pelvic brace at each time step (50 Hz) was recorded during the WRAPS condition.

[5]This metronome pace is different from the movements in section 3.2 since subjects reported this metronome pace to be more comfortable to follow.

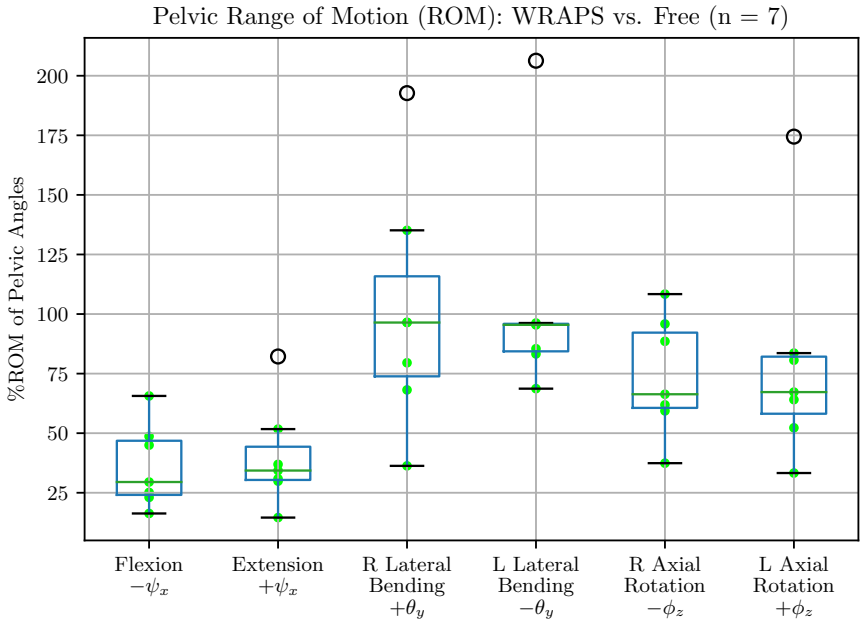

Figure 3.14: Box plots of pelvic range of motion (ROM) in WRAPS compared to “free" condition. Data points that extend over 1.5 times of interquartile range (IQR = Q3 - Q1) from the edges of the box are excluded as outliers.

3.8 Results and Discussions

3.8.1 Pelvic Range of Motion

The peak rotational angles in the primary planes of motion (Movement Nos. 1-6 in Table 3.4) were used to evaluate the percent pelvic range of motion (%pROM) when wearing the pelvic WRAPS compared to the “free” pelvic movement condition. The average %pROM of the WRAPS is shown in Table 3.5. The box plots of data points from the seven subjects are also presented in Fig. 3.14. Overall, the group average of the %pROM in the lateral bending direction (θ_y) are over 85% in both directions, which are the largest percentages among all the rotational directions. The average %pROM in the axial rotation are over 60%. The flexion and extension angles are shown to have smaller %pROM than other single plane ROMs at 36.19% and 33.05% respectively. This may be due to exaggerated flexion and extension angles from sliding motions of the pelvic brace relative to the torso of the subject during the “free” condition.

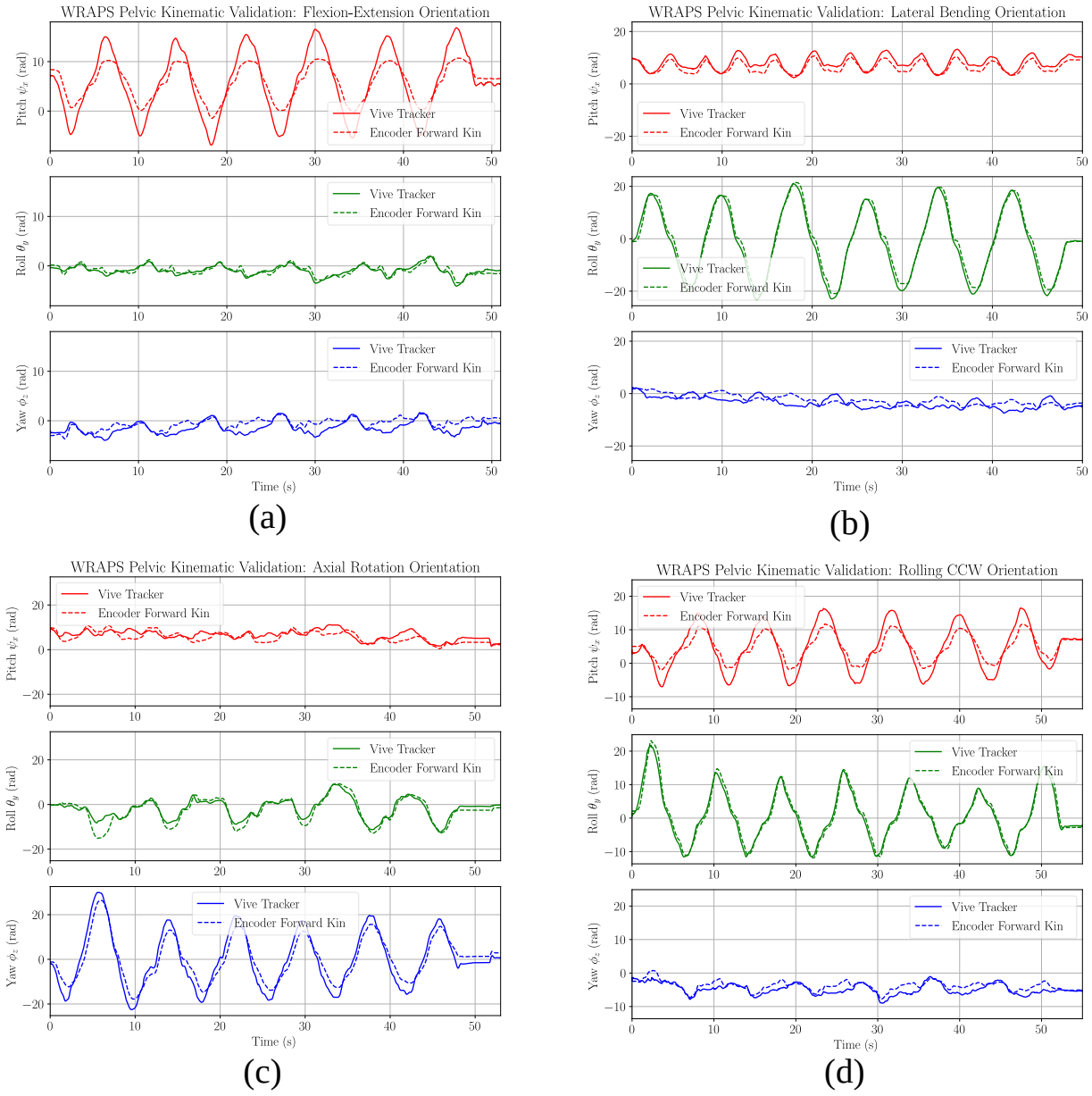

Figure 3.15: Rotational angles of the pelvic brace measured by the Vive tracker vs. forward kinematics from the encoder readings during cyclic movements by a selected subject: (a) flexion-extension, (b) lateral bending, (c) axial rotation, and (d) rolling in counter-clockwise direction.

Table 3.6: Group average (±SD) of rotation measurement accuracy by pelvic WRAPS (n = 6). Bold values are the primary angles in the planes of motion.

Motion	Error	Pitch ψ_x (deg)	Roll θ_y (deg)	Yaw ϕ_z (deg)
Flexion-Extension (Sagittal Plane)	MAE	**2.8 ± 0.7**	1.9 ± 2.2	2.0 ± 0.6
	RMSE	**3.4 ± 1.0**	2.1 ± 2.2	2.1 ± 0.6
	Peak	**7.6 ± 2.1**	3.7 ± 3.4	3.5 ± 0.8
Lateral Bending (Frontal Plane)	MAE	1.8 ± 1.2	**2.8 ± 1.4**	2.7 ± 1.0
	RMSE	2.0 ± 1.2	**3.3 ± 1.6**	2.9 ± 1.0
	Peak	4.4 ± 2.3	**7.7 ± 3.6**	5.4 ± 1.4
Axial Rotation (Transverse Plane)	MAE	2.1 ± 1.3	2.4 ± 1.9	**3.4 ± 0.9**
	RMSE	2.5 ± 1.5	2.8 ± 1.9	**3.9 ± 1.0**
	Peak	5.4 ± 3.5	6.8 ± 2.9	**8.5 ± 2.5**
Rolling (Combined)	MAE	2.7 ± 0.9	3.0 ± 2.1	2.6 ± 1.3
	RMSE	3.3 ± 1.1	3.6 ± 2.3	2.8 ± 1.2
	Peak	7.0 ± 2.5	8.1 ± 4.0	5.2 ± 2.0

3.8.2 Kinematic Validation

The data from the cyclical movements in single planes of motion (Movement Nos. 7-9) and combination of different planes (Movement No. 10) in Table 3.4 were use to evaluate the accuracy of the forward kinematic calculation from the encoder readings described in Section 3.6. A subject was excluded from the data analysis due to poor quality of tracker data. The results of group average (n = 6) of mean absolute error (MAE), root-mean-square error (RMSE), and peak of absolute error (Peak) over each of the movement sessions are shown in Table 3.6. Also, the recorded rotational angles of the pelvic brace over time (VR tracker vs. forward kinematics) in the four movement sessions performed by a selected subject are shown in Fig. 3.15.

The group average MAE and RMSE of the main angle in each of the planes are under 4.0 degrees, while the maximum average peak is at 8.5 degrees in the ϕ_z direction. All the average MAE and RMSE values in the rolling motion are also under 4.0 degrees, while the maximum average peak error is 8.1 degrees in the θ_y direction.

In Fig. 3.15 (a) and (d), the errors in the flexion-extension angle (pitch ψ_x) are increased around

the peaks of the cycles. This may be due to the external gravitational moment from the human body at the extreme positions in the sagittal plane, which created some deflection in the mechanical components and thus increased the tilt angles of the pelvic brace beyond the encoder readings.

3.9 Conclusions

We proposed a novel methodology for design and optimization of a fully-actuated 3-DOF parallel mechanism that accommodates an individual's pelvic seated range of motion (ROM) and instantaneous screw axes (ISAs) of the pelvic segment from motion capture data. A two-stage optimization routine was developed based on kinematic geometry and screw theory.

According to the results from the experiment, the mechanism can accommodate over 60 %pROM on an average across a group of able-bodied adults in the lateral bending and axial rotation, which seems promising for the pressure relief applications. The small %pROM observed in the flexion and extension angles may be due to the sliding motion of the pelvic brace during the "free" condition. Friction in the mechanism may also inhibit some motion in the sagittal plane. This problem can be overcome by adding friction compensation torque commands to the motor or use other control strategies in the transparent mode that are more responsive to external force-moment applied by the user.

The accuracy of the position sensors of the pelvic WRAPS against the validating VR tracking system are under 4 degrees of MAE and RSME group averages across all movements. The average peak errors, which tend to occur at extreme positions due to deflections of the mechanical components are kept below 9 degrees. We believe this level of accuracy is acceptable for postural training and rehabilitation applications.

Also, the pelvic brace design and the mechanism architecture can adapt to a wide range of subject sizes. The pelvic brace can fit both genders with pant sizes from XS to L (US). The adjustabilty of the linkage sizes in the [$\underline{\text{R}}$RR]U-2[$\underline{\text{R}}$R]S architecture makes it possible for the subject to comfortably wear the pelvic brace in their neutral configurations.

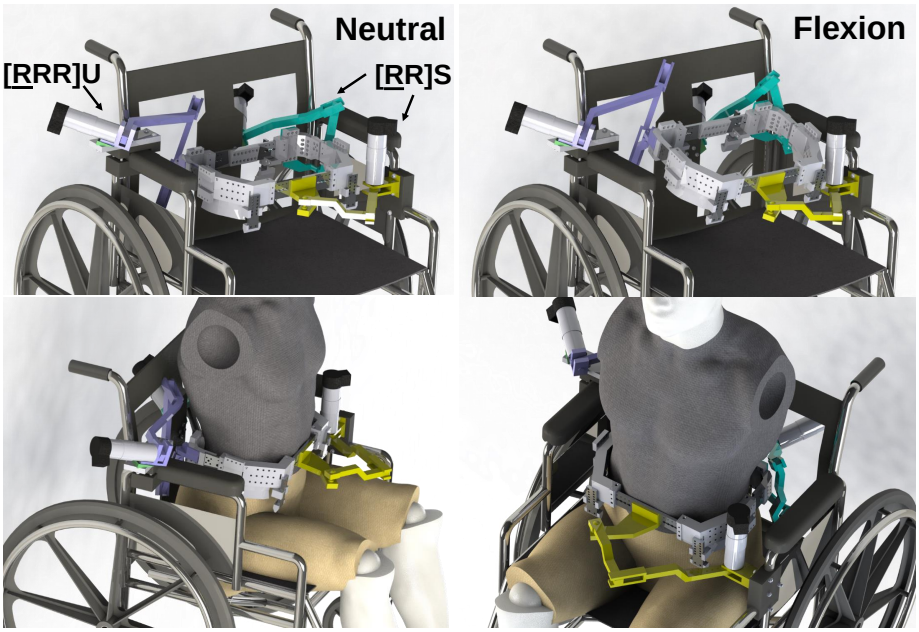

Figure 3.16: Visualization of a pelvic WRAPS design mounted on the wheelchair

In terms of transitioning from a lab prototype to a product in the real world, a simplified 3D CAD of the mechanism mounted on a wheelchair is visualized in Fig. 3.16. The structures of the first (purple) and the second (teal) limbs on the back are modeled to avoid interference with the user and the wheelchair. The third (yellow) limb in the front is installed like a dining table. Also, a cable-pulley transmission system from each motor can be added in order to mount the three motors at specific positions on the wheelchair.

In order to adapt the design to wheelchair users with limited trunk control, a set of movement data templates from size-matched healthy subjects can be used to optimize the mechanism architecture. In a case where the patient already has some postural abnormalities, it is better to collect movement data directly from the patient, being assisted by physical therapists (PTs). Alternately, an age and size-matched healthy subject can perform prescribed movements to customize for the specific patient.

Chapter 4: Summary

WRAPS is the first of its kind torso exoskeleton for seated trunk movements. The ultimate goals of the WRAPS system are to promote postural stability, seated mobility, and independence of the wheelchair users who have impaired trunk control. New design methodologies of this wearable device have been proposed as a major step towards development of a torso exoskeleton for sitting postures. The WRAPS project is summarized in the following topics:

4.1 Key Contributions

We propose new spatial multi-DOF parallel mechanism designs for movements of the upper trunk and the pelvis on the seat. The 4-DOF mechanism for the thoracic segment can accommodate/assist necessary DOFs of the trunk for ADL while maintaining a good spinal posture. The 3-DOF pelvic mechanism can accommodate all rotational directions with coupled translation of the pelvis on the seat. The pelvic mechanism was synthesized based on motion capture data with ISAs to achieve a data-driven ergonomic design. This design framework is based on the Screw Theory, which is the intersection between human biomechanics and robot kinematics. Also, the merits of the low-DOF (< 6-DOF) design are easier hardware realization, lower cost, safety, and simpler control strategies.

4.2 Limitations

The current prototypes are mounted on a custom-made bench and are not compatible with standard wheelchairs. Ideally, the pelvic mechanism can be optimized from a group of subjects rather than a single subject. The human studies in this dissertation are still limited to able-bodied subjects. The current adjustablity of the brace may not be able to fully accommodate the average size of the patient population.

4.3 Future Works

The combined mechanism for both segment is essential to modulate the overall spinal posture on the seat, especially for users with severe neurological impairment. A CAD model and a prototype of the combined mechanism for the pelvic and thoracic segments are shown in Fig. 4.1 (a) and (b) respectively. The system has 7 DOFs in total by connecting the [RRR]U-2[RR]S and the 2[RP]S-2UPS mechanisms in series. New control strategies for postural training or assistance using this full WRAPS system is to be developed. In addition, our potential research directions using WRAPS are as follows:

4.3.1 Postural Training and Rehabilitation

WRAPS is a unique system that can be used to investigate new rehabilitation training paradigms for postural control on the seat. Our three open research questions are: (i) how can we use the WRAPS to train seated functional movement, promote healthy sitting posture, and enhance sitting stability of individuals with SCI or CP who still have partial trunk control? (ii) which methodology is the most effective for motor learning, including the adaptation to novel tasks outside the training? And (iii) how can we quantify the improvement of one's control of posture overtime? We will explore new postural training methods by using the WRAPS system which can directly control and measure positions and forces at the pelvic and thoracic segments. New functional assessment of one's postural control will be developed based on subject data collected by the WRAPS along with other physiological measurements (EEG, EMG, etc.), which may facilitate the translation from the healthy subject training to patient rehabilitation. Able-bodied subjects will be assigned to learn novel and challenging tasks, such as reaching in different directions within or beyond their margin of stability and interacting with perturbative or assistive force fields generated by the WRAPS. For patient subjects, assigned tasks will be based on their level of impairment and the design of their personal torso support devices. Also, it is interesting to utilize immersive 3D visual feedbacks like VR for studying complex movements like reaching tasks that require significant coordination of the

pelvis, the upper trunk, and the head [83]. Furthermore, we can incorporate measurements from an instrumented pressure mat to study the effectiveness of the pressure relief maneuvers assisted by the WRAPS.

4.3.2 User-intent Control

This future aim is geared toward population with higher levels of trunk impairment where the WRAPS is mainly used to restore and augment daily functional movement of the user through assistance at the pelvic and the thoracic levels. Complex coordination between body segments during seated functional tasks makes it challenging to directly map movement intention from the user to the robot control. Therefore, algorithms for user intent detection and control of the WRAPS will be developed from collected sensor data associated with functional movements. There are two main research questions needed to be addressed: (i) what are the required sensor modules and decoding algorithm needed to achieve intuitive user control for required functional tasks?, and (ii) how do we generalize and project trunk movement data from healthy subjects to patients who severely lack trunk mobility? Significant contributions from these future aims are: (a) we will develop a new real-time decoding algorithm for intuitive control interface of the WRAPS system for assisting the sitting maneuvers, and (b) we will close the user-robot control loop as we design a new feedback interface for patients who lost sensory information to be aware of their current posture and be able to independently decide their desired movement goals, such as pressure reliefs and reaching tasks.

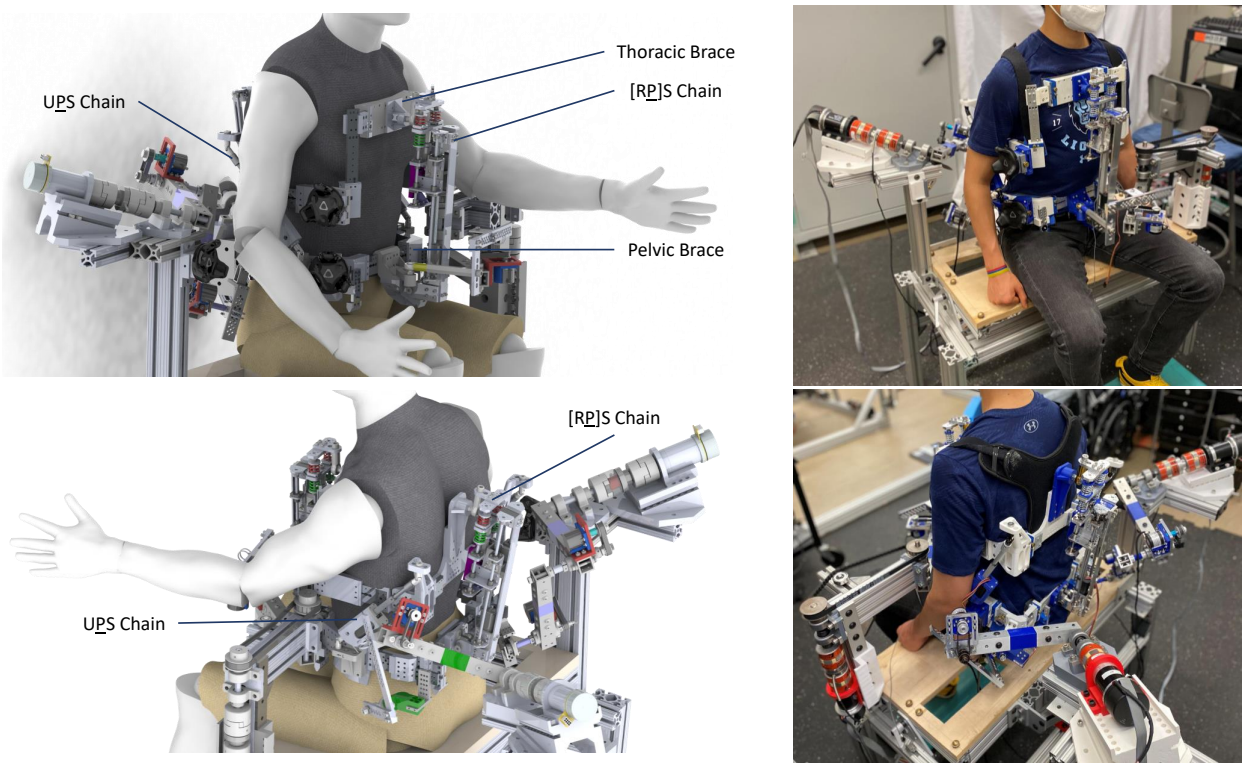

(a) (b)

Figure 4.1: (a) CAD model of WRAPS with combined pelvic ([RRR]U-2[RR]S) and thoracic (2[RP]S-2UPS) mechanisms and (b) a subject wearing the actual prototype.

References

[1] B. Gagnon, C. Vincent, and L. Noreau, "Adaptation of a seated postural control measure for adult wheelchair users," *Disability and Rehabilitation*, vol. 27, pp. 951–959, Sep. 2005.

[2] M. Hadders-Algra, "Typical and atypical development of reaching and postural control in infancy," *Developmental Medicine & Child Neurology*, vol. 55, pp. 5–8, 2013.

[3] H. A. M. Seelen, Y. J. M. Potten, A Huson, F Spaans, and J. P. H. Reulen, "Impaired balance control in paraplegic subjects," *Journal of Electromyography and Kinesiology*, vol. 7, no. 2, pp. 149–160, 1997.

[4] National Spinal Cord Injury Statistical Center, "Spinal cord injury facts and figures at a glance," University of Alabama at Birmingham, Birmingham, AL, Tech. Rep., 2021.

[5] L. H. C. Peeters, I. J. M. de Groot, and A. C. H. Geurts, "Trunk involvement in performing upper extremity activities while seated in neurological patients with a flaccid trunk – A review," *Gait & Posture*, vol. 62, pp. 46–55, 2018.

[6] E. Butler Forslund, K. S. Roaldsen, C. Hultling, K. Wahman, and E. Franzén, "Concerns about falling in wheelchair users with spinal cord injury-validation of the Swedish version of the spinal cord injury falls concern scale," *Spinal Cord*, vol. 54, no. 2, pp. 115–119, 2016.

[7] E. Butler Forslund, V. Jørgensen, E. Franzén, A. Opheim, Seiger, A. Ståhle, C. Hultling, J. K. Stanghelle, K. Skavberg Roaldsen, and K. Wahman, "High incidence of falls and fall-related injuries in wheelchair users with spinal cord injury: A prospective study of risk indicators," *Journal of Rehabilitation Medicine*, vol. 49, no. 2, pp. 144–151, 2017.

[8] N. Sezer, S. Akkuş, and F. G. Uğurlu, "Chronic complications of spinal cord injury," *World Journal of Orthopedics*, vol. 6, no. 1, p. 24, 2015.

[9] J. V. Subbarao, J. Klopfstein, and R. Turpin, "Prevalence and impact of wrist and shoulder pain in patients with spinal cord injury," *The Journal of Spinal Cord Medicine*, vol. 18, no. 1, pp. 9–13, Jan. 1995.

[10] M. Dalyan, D. D. Cardenas, and B. Gerard, "Upper extremity pain after spinal cord injury," *Spinal Cord*, vol. 37, no. 3, pp. 191–195, 1999.

[11] D. Christensen, K. Van Naarden Braun, N. S. Doernberg, M. J. Maenner, C. L. Arneson, M. S. Durkin, R. E. Benedict, R. S. Kirby, M. S. Wingate, R. Fitzgerald, and M. Yeargin-Allsopp, "Prevalence of cerebral palsy, co-occurring autism spectrum disorders, and motor functioning

– Autism and Developmental Disabilities Monitoring Network, USA, 2008," *Developmental Medicine and Child Neurology*, vol. 56, no. 1, pp. 59–65, Jan. 2014.

[12] M. Persson-Bunke, G. Hägglund, H. Lauge-Pedersen, P. Wagner, and L. Westbom, "Scoliosis in a total population of children with cerebral palsy," *Spine*, vol. 37, no. 12, E708–E713, 2012.

[13] R. Vialle, C. Thévenin-Lemoine, and P. Mary, "Neuromuscular scoliosis," *Orthopaedics & Traumatology: Surgery & Research*, vol. 99, no. 1, Supplement, S124–S139, Feb. 2013.

[14] A. Miller, T. Temple, and F. Miller, "Impact of orthoses on the rate of scoliosis progression in children with cerebral palsy," *Journal of Pediatric Orthopaedics*, vol. 16, no. 3, 1996.

[15] S. M. Michael, D. Porter, and T. E. Pountney, "Tilted seat position for non-ambulant individuals with neurological and neuromuscular impairment: A systematic review," *Clinical Rehabilitation*, vol. 21, no. 12, pp. 1063–1074, 2007.

[16] L. Stockton and S. Rithalia, "Is dynamic seating a modality worth considering in the prevention of pressure ulcers?" *Journal of Tissue Viability*, vol. 17, no. 1, pp. 15–21, Feb. 2008.

[17] T. K. Koo, A. F. Mak, and Y. Lee, "Posture effect on seating interface biomechanics: Comparison between two seating cushions," *Archives of Physical Medicine and Rehabilitation*, vol. 77, no. 1, pp. 40–47, Jan. 1996.

[18] M. Makhsous, D. M. Rowles, W. Z. Rymer, J. Bankard, E. K. Nam, D. Chen, and F. Lin, "Periodically relieving ischial sitting load to decrease the risk of pressure ulcers," *Archives of Physical Medicine and Rehabilitation*, vol. 88, no. 7, pp. 862–870, Jul. 2007.

[19] S. E. Sonenblum, T. E. Vonk, T. W. Janssen, and S. H. Sprigle, "Effects of wheelchair cushions and pressure relief maneuvers on ischial interface pressure and blood flow in people with spinal cord injury," *Archives of Physical Medicine and Rehabilitation*, vol. 95, no. 7, pp. 1350–1357, 2014.

[20] T. Ogura, T. Itami, K. Yano, I. Mori, and K. Kameda, "An assistance device to help people with trunk impairment maintain posture," in *2017 International Conference on Rehabilitation Robotics (ICORR)*, 2017, pp. 358–363, ISBN: VO -.

[21] M. Makhsous, S. Taylor, D. Pucci, J. Bankard, L. Ruberte, and F. Lin, "Flexible and user-adjustable lumbar-pelvic-thoracic support system for wheelchair seating," in *Rehabilitation Engineering and Assistive Technology Society of North America (RESNA) 28th Annual Conference*, Atlanta, Georgia, US, 2005.

[22] K. Shiotani, D. Chugo, S. Yokota, Y. Sakaida, and H. Hashimoto, "A depressurization assistance system with a suitable posture for a seated patient on a wheelchair," in *2013 IEEE*

13th International Conference on Rehabilitation Robotics (ICORR), 2013, pp. 1–6, ISBN: 1945-7898 VO -.

[23] P. van Geffen, J. Reenalda, P. H. Veltink, and B. F. Koopman, "Decoupled pelvis rotation in sitting: A passive motion technique that regulates buttock load associated with pressure ulcer development," *Journal of Biomechanics*, vol. 42, no. 9, pp. 1288–1294, Jun. 2009.

[24] M. N. Mahmood, L. H. C. Peeters, M. Paalman, G. J. Verkerke, I. Kingma, and J. H. van Dieën, "Development and evaluation of a passive trunk support system for Duchenne muscular dystrophy patients," *Journal of NeuroEngineering and Rehabilitation*, vol. 15, p. 22, Mar. 2018.

[25] S. L. Hurley, A. Hayes, D. Yamada, A. Siekman, J. Noon, and P. Axelson, "Increased forward lean among wheelchair users with use of a dynamic pelvic stabilization device," in *RESNA 26th International Annual Conference*, Atlanta, Georgia, US, 2003.

[26] A. Abreu, P. Arezes, C. Silva, and R. Santos, "A case study of product usability of a pelvic device used by children with neuromotor impairments," *Procedia Manufacturing*, vol. 3, pp. 5451–5458, Dec. 2015.

[27] M. Makhsous, F. Lin, R. W. Hendrix, M. Hepler, and L.-Q. Zhang, "Sitting with adjustable ischial and back supports: Biomechanical changes," *Spine*, vol. 28, no. 11, 2003.

[28] N. Coomer, L. Labno, M. Carlevato, L. Pemberton, J. Quach, E. Mcleod, F. Lin, and M. Makhsous, "Reaching performance using a new seat design in wheelchair users with spinal cord injury," in *Rehabilitation Engineering and Assistive Technology Society of North America (RESNA) 29th Annual Conference*, Jun. 2006.

[29] C. T. Li, Y. N. Chen, Y. T. Tseng, and K. H. Tsai, "Biomechanical analysis of different dynamic sitting techniques: An exploratory study," *BioMedical Engineering Online*, vol. 18, no. 1, pp. 1–7, 2019.

[30] P. van Geffen, J. Reenalda, P. H. Veltink, and B. F. Koopman, "Effects of sagittal postural adjustments on seat reaction load," *Journal of Biomechanics*, vol. 41, no. 10, pp. 2237–2245, Jul. 2008.

[31] J. Reenalda, P. van Geffen, G. Snoek, M. Jannink, M. Ijzerman, and H. Rietman, "Effects of dynamic sitting interventions on tissue oxygenation in individuals with spinal cord disorders," *Spinal Cord*, vol. 48, no. 4, pp. 336–341, 2010.

[32] M. I. Khan, V. Santamaria, J. Kang, B. M. Bradley, J. P. Dutkowsky, M Andrew, and S. K. Agrawal, "Enhancing seated stability using Trunk Support Trainer (TruST)*," *IEEE Robotics and Automation Letters*, pp. 1–8, 2016.

[33] M. I. Khan, A Prado, and S. K. Agrawal, "Effects of virtual reality training with Trunk Support Trainer (TruST) on postural kinematics," *IEEE Robotics and Automation Letters*, vol. 2, no. 4, pp. 2240–2247, 2017.

[34] V. Santamaria, T. Luna, M. Khan, and S. Agrawal, "The robotic Trunk-Support-Trainer (TruST) to measure and increase postural workspace during sitting in people with spinal cord injury," *Spinal Cord Series and Cases*, vol. 6, no. 1, p. 1, 2020.

[35] J.-H. Park, P Stegall, and S. K. Agrawal, "Dynamic brace for correction of abnormal postures of the human spine," *Robotics and Automation (ICRA), 2015 IEEE International Conference on*, pp. 5922–5927, 2015.

[36] R. C. Murray, C. Ophaswongse, and S. K. Agrawal, "Design of a wheelchair robot for active postural support," *Journal of Mechanisms and Robotics*, vol. 11, no. 2, pp. 20 911–20 919, Feb. 2019.

[37] Q. Li, Z. Huang, and J. M. Hervé, "Displacement manifold method for type synthesis of lower-mobility parallel mechanisms," *Science in China Series E: Technological Sciences*, vol. 47, no. 6, pp. 641–650, 2004.

[38] D. Gan, J. S. Dai, J. Dias, R. Umer, and L. Seneviratne, "Singularity-free workspace aimed optimal design of a 2T2R parallel mechanism for sutomated fiber placement," *Journal of Mechanisms and Robotics*, vol. 7, no. 4, pp. 41 022–41 029, Nov. 2015.

[39] Z. Wang, S. Ji, Y. Wan, C. Ou, J. Sun, and G. Wang, "Optimal design of parallel robots for the prescribed regular dexterous workspace," in *2007 IEEE International Conference on Automation and Logistics*, 2007, pp. 563–568, ISBN: 2161-8151 VO -.

[40] S. Caro, D. Chablat, P. Wenger, and J. Angeles, "The isoconditioning loci of planar three-dof parallel manipulators," *Recent Advances in Integrated Design and Manufacturing in Mechanical Engineering*, pp. 129–138, 2003.

[41] F. Ranjbaran, J. Angeles, M. A. González-Palacios, and R. V. Patel, "The mechanical design of a seven-axes manipulator with kinematic isotropy," *Journal of Intelligent & Robotic Systems*, vol. 14, no. 1, pp. 21–41, 1995.

[42] C. C. Nguyen, S. C. Antrazi, Z. L. Zhou, and C. E. Campbell, "Analysis and implementation of a 6 DOF Stewart platform-based robotic wrist," *Computers and Electrical Engineering*, vol. 17, no. 3, pp. 191–203, 1991.

[43] L.-W. Tsai, *Robot Analysis and Design: The Mechanics of Serial and Parallel Manipulators*, 1st ed. New York, NY, USA: John Wiley \& Sons, Inc., 1999, p. 520.

[44] C. Ophaswongse, R. C. Murray, V. Santamaria, Q. Wang, and S. K. Agrawal, "Human evaluation of Wheelchair Robot for Active Postural Support (WRAPS)," *Robotica*, vol. 37, no. 12, pp. 2132–2146, Dec. 2019.

[45] G. Wu, F. C. van der Helm, H. (DirkJan) Veeger, M. Makhsous, P. Van Roy, C. Anglin, J. Nagels, A. R. Karduna, K. McQuade, X. Wang, F. W. Werner, and B. Buchholz, "ISB recommendation on definitions of joint coordinate systems of various joints for the reporting of human joint motion—Part II: shoulder, elbow, wrist and hand," *Journal of Biomechanics*, vol. 38, no. 5, pp. 981–992, May 2005.

[46] M. S. M., "Electromyographic activity of the abdominal and low back musculature during the generation of isometric and dynamic axial trunk torque: Implications for lumbar mechanics," *Journal of Orthopaedic Research*, vol. 9, no. 1, pp. 91–103, Feb. 2005.

[47] L. Danneels, P. Coorevits, A. Cools, G. Vanderstraeten, D. Cambier, E. Witvrouw, and H. De Cuyper, "Differences in electromyographic activity in the multifidus muscle and the iliocostalis lumborum between healthy subjects and patients with sub-acute and chronic low back pain," *European Spine Journal*, vol. 11, no. 1, pp. 13–19, Feb. 2002.

[48] K. O'Sullivan, R. McCarthy, A. White, L. O'Sullivan, and W. Dankaerts, "Lumbar posture and trunk muscle activation during a typing task when sitting on a novel dynamic ergonomic chair," *Ergonomics*, vol. 55, Sep. 2012.

[49] M. S. Redfern, R. E. Hughes, and D. B. Chaffin, "High-pass filtering to remove electrocardiographic interference from torso EMG recordings," *Clinical Biomechanics*, vol. 8, no. 1, pp. 44–48, 1993.

[50] P. Konrad, "The ABC of EMG: A practical introduction to kinesological electromyography," in, 1.4, Scottsdale, Arizona: Noraxon U.S.A., Inc., 2005, pp. 1–61, ISBN: 0-9771622-1-4.

[51] M. Panjabi, K. Abumi, J. Duranceau, and T. Oxland, "Spinal stability and intersegmental muscle forces. A biomechanical model.," *Spine*, vol. 14, no. 2, pp. 194–200, 1989.

[52] H. Kinoshita, "Pathology of hyperextension injuries of the cervical spine," *Spinal Cord*, vol. 32, no. 6, p. 367, 1994.

[53] P. S. Sun, J Mai, Z Zhou, S Agrawal, and Q Wang, "Upper-body motion mode recognition based on IMUs for a dynamic spine brace," in *2018 IEEE International Conference on Cyborg and Bionic Systems (CBS)*, 2018, pp. 167–170, ISBN: VO -.

[54] A. Page, H. de Rosario, V. Mata, R. Porcar, J. Solaz, and M. J. Such, "Kinematics of the trunk in sitting posture: An analysis based on the instantaneous axis of rotation," *Ergonomics*, vol. 52, no. 6, pp. 695–706, Jun. 2009.

[55] O. Heidari, E. T. Wolbrecht, A. Perez-Gracia, and Y. S. Yihun, "A task-based design methodology for robotic exoskeletons," *Journal of Rehabilitation and Assistive Technologies Engineering*, vol. 5, p. 2 055 668 318 800 672, 2018.

[56] H. Zhang and S. K. Agrawal, "Kinematic design of a dynamic brace for measurement of head/neck motion," *IEEE Robotics and Automation Letters*, vol. 2, no. 3, pp. 1428–1435, 2017.

[57] A. Gupta, M. K. O'Malley, V. Patoglu, and C. Burgar, "Design, control and performance of RiceWrist: A force feedback wrist exoskeleton for rehabilitation and training," *The International Journal of Robotics Research*, vol. 27, no. 2, pp. 233–251, 2008.

[58] Y. Yu and W. Liang, "Manipulability inclusive principle for hip joint assistive mechanism design optimization," *The International Journal of Advanced Manufacturing Technology*, vol. 70, no. 5, pp. 929–945, Feb. 2014.

[59] Y. Du, R. Li, D. Li, and S. Bai, "An ankle rehabilitation robot based on 3-RRS spherical parallel mechanism," *Advances in Mechanical Engineering*, vol. 9, no. 8, p. 1 687 814 017 718 112, Aug. 2017.

[60] J. Hunt and H. Lee, "A new parallel actuated architecture for exoskeleton applications involving multiple degree-of-freedom biological joints," *Journal of Mechanisms and Robotics*, vol. 10, no. 5, pp. 51 010–51 017, Aug. 2018.

[61] C. Ophaswongse and S. K. Agrawal, "Optimal design of a novel 3-DOF orientational parallel mechanism for pelvic assistance on a wheelchair: An approach based on kinematic geometry and screw theory," *IEEE Robotics and Automation Letters*, vol. 5, no. 2, pp. 3315–3322, 2020.

[62] S. M. Lynch, P. Leahy, and S. P. Barker, "Reliability of measurements obtained with a modified functional reach test in subjects with spinal cord injury," *Physical Therapy*, vol. 78, no. 2, pp. 128–133, Feb. 1998.

[63] R. Aissaoui, C. Boucher, D. Bourbonnais, M. Lacoste, and J. Dansereau, "Effect of seat cushion on dynamic stability in sitting during a reaching task in wheelchair users with paraplegia," *Archives of Physical Medicine and Rehabilitation*, vol. 82, no. 2, pp. 274–281, Feb. 2001.

[64] O. Sorkine-Hornung and M. Rabinovich, "Least-squares rigid motion using svd," *Computing*, vol. 1, no. 1, 2017.

[65] J.-P. Merlet, *Parallel Robots*, ser. Solid Mechanics and Its Applications. Berlin/Heidelberg: Springer-Verlag, 2006, vol. 2, ISBN: 9781402041327.

[66] Z. Huang, Z. Chen, J. Liu, and S. Liu, "A 3DOF rotational parallel manipulator without intersecting axes," *Journal of Mechanisms and Robotics*, vol. 3, no. 2, p. 021 014, May 2011.

[67] Z. Huang and J. Wang, "Identification of principal screws of 3-DOF parallel manipulators by quadric degeneration," *Mechanism and Machine Theory*, vol. 36, no. 8, pp. 893–911, Aug. 2001.

[68] Z. Chen, H. Ding, W. Cao, and Z. Huang, "Axodes analysis of the multi DOF parallel mechanisms and parasitic motion," in *Proceedings of the ASME Design Engineering Technical Conference*, vol. 6, 2013.

[69] L. Nurahmi, J. Schadlbauer, S. Caro, M. Husty, and P. Wenger, "Kinematic snalysis of the 3-RPS cube parallel manipulator," *Journal of Mechanisms and Robotics*, vol. 7, no. 1, Feb. 2015.

[70] Z. Chen, W.-a. Cao, and Z. Huang, "Type synthesis of 3-DOF rotational parallel mechanisms with no intersecting axes," in *Volume 4: 36th Mechanisms and Robotics Conference, Parts A and B*, ASME, Aug. 2012, p. 565, ISBN: 978-0-7918-4503-5.

[71] R. S. Ball, *A Treatise on the Theory of Screws*. Cambridge university press, 1900, ISBN: 0521636507.

[72] S. A. Joshi and L.-W. Tsai, "Jacobian analysis of limited-DOF parallel manipulators," *Journal of Mechanical Design*, vol. 124, no. 2, pp. 254–258, May 2002.

[73] M. B. Hong and Y. J. Choi, "Kinestatic analysis of nonsingular lower mobility manipulators," *IEEE Transactions on Robotics*, vol. 25, no. 4, pp. 938–942, 2009.

[74] M. B. Hong and Y. J. Choi, "Formulation of unique form of screw based jacobian for lower mobility parallel manipulators," *Journal of Mechanisms and Robotics*, vol. 3, no. 1, pp. 11 002–11 006, Nov. 2010.

[75] T. Huang, H. T. Liu, and D. G. Chetwynd, "Generalized jacobian analysis of lower mobility manipulators," *Mechanism and Machine Theory*, vol. 46, no. 6, pp. 831–844, 2011.

[76] K. Deb, A. Pratap, S. Agarwal, and T. Meyarivan, "A fast and elitist multiobjective genetic algorithm: NSGA-II," *IEEE Transactions on Evolutionary Computation*, vol. 6, no. 2, pp. 182–197, 2002.

[77] X.-J. Liu, C. Wu, and J. Wang, "A new approach for singularity analysis and closeness measurement to singularities of parallel manipulators," *Journal of Mechanisms and Robotics*, vol. 4, no. 4, pp. 41 001–41 010, Aug. 2012.

[78] J. Wang, C. Wu, and X. J. Liu, "Performance evaluation of parallel manipulators: Motion/force transmissibility and its index," *Mechanism and Machine Theory*, vol. 45, no. 10, pp. 1462–1476, Oct. 2010.

[79] H. Liu, T. Huang, A. Kecskeméthy, and D. G. Chetwynd, "A generalized approach for computing the transmission index of parallel mechanisms," *Mechanism and Machine Theory*, vol. 74, pp. 245–256, Apr. 2014.

[80] M. Quigley, K. Conley, B. Gerkey, J. Faust, T. Foote, J. Leibs, R. Wheeler, and A. Y. Ng, "ROS: An open-source Robot Operating System," in *ICRA workshop on open source software*, vol. 3, Kobe, Japan, 2009, p. 5.

[81] S. Chitta, E. Marder-Eppstein, W. Meeussen, V. Pradeep, A. Rodríguez Tsouroukdissian, J. Bohren, D. Coleman, B. Magyar, G. Raiola, M. Lüdtke, and E. Fernández Perdomo, "ros_control: A generic and simple control framework for ROS," *The Journal of Open Source Software*, 2017.

[82] K. M. Lynch and F. C. Park, *Modern Robotics: Mechanics, Planning, and Control*. Cambridge University Press, 2017, ISBN: 1107156300.

[83] E. Chateauroux and X. Wang, "Effects of age, gender, and target location on seated reach capacity and posture," *Human Factors*, vol. 50, no. 2, pp. 211–226, Apr. 2008.

[84] H. Taghirad, *Parallel Robots: Mechanics and Control*. CRC Press, 2013, p. 533, ISBN: 9781466555761.

[85] M. W. Spong and M. Vidyasagar, *Robot Dynamics and Control*, 3. John Wiley & Sons, 1989, vol. 28, pp. 655–656, ISBN: 978-0471612438.

[86] H. Lipkin and J. Duffy, "Sir Robert Stawell Ball and methodologies of modern screw theory," *Proceedings of the Institution of Mechanical Engineers, Part C: Journal of Mechanical Engineering Science*, vol. 216, no. 1, pp. 1–11, 2002.

[87] K. H. Hunt, *Kinematic Geometry of Mechanisms*. Clarendon Press ; Oxford University Press Oxford : New York, 1978, xvii, 465 p. : ISBN: 0198561245.

[88] C. Chen and J. Angeles, "Generalized transmission index and transmission quality for spatial linkages," *Mechanism and Machine Theory*, vol. 42, no. 9, pp. 1225–1237, Sep. 2007.

Appendix A: Newton-Raphson Jacobian

The Newton-Raphson Jacobian $\mathbf{J}_f$ can be derived by starting from a velocity Jacobian $\mathbf{J}_s$ [84] that maps the Cartesian velocities $\dot{\mathbf{X}}_s = \begin{bmatrix} \dot{x} & \dot{y} & \dot{z} & \omega_x & \omega_y & \omega_z \end{bmatrix}^T$ to the joint velocities $\dot{\mathbf{q}} = \begin{bmatrix} \dot{q}_1 & \dot{q}_2 & \dot{q}_3 & \dot{q}_4 \end{bmatrix}^T$:

$$\dot{\mathbf{q}} = \mathbf{J}_s \dot{\mathbf{X}}_s \tag{A.1}$$

where $\mathbf{J}_s = \begin{bmatrix} \hat{\mathbf{q}}_1^T & (\mathbf{R}\mathbf{b}_1 \times \hat{\mathbf{q}}_1)^T \\ \hat{\mathbf{q}}_2^T & (\mathbf{R}\mathbf{b}_2 \times \hat{\mathbf{q}}_2)^T \\ \hat{\mathbf{q}}_3^T & (\mathbf{R}\mathbf{b}_3 \times \hat{\mathbf{q}}_3)^T \\ \hat{\mathbf{q}}_4^T & (\mathbf{R}\mathbf{b}_4 \times \hat{\mathbf{q}}_4)^T \end{bmatrix}$, and $\hat{\mathbf{q}}_i = \frac{\hat{\mathbf{q}}_i}{\|\hat{\mathbf{q}}_i\|}$.

From the relationship between the angular velocities and the rate of change of the Euler angles (α, β, γ) in the current X-Y-Z sequence [85]

$$\boldsymbol{\omega} = \begin{bmatrix} \omega_x \\ \omega_y \\ \omega_z \end{bmatrix} = \begin{bmatrix} 0 & 0 & s\beta \\ 0 & c\alpha & -s\alpha c\beta \\ 1 & s\alpha & c\alpha c\beta \end{bmatrix} \begin{bmatrix} \dot{\alpha} \\ \dot{\beta} \\ \dot{\gamma} \end{bmatrix} = \mathbf{E}(\alpha, \beta, \gamma) \begin{bmatrix} \dot{\alpha} \\ \dot{\beta} \\ \dot{\gamma} \end{bmatrix}. \tag{A.2}$$

we can convert the rate of change of the Euler angles to angular velocities by

$$\dot{\mathbf{X}}_s = \mathbf{D}\dot{\mathbf{X}}_c \tag{A.3}$$

where $\mathbf{D} = \left[\begin{array}{c|c} \mathbf{I}_{3\times3} & \mathbf{0}_{3\times3} \\ \hline \mathbf{0}_{3\times3} & \mathbf{E}(\alpha, \beta, \gamma) \end{array}\right]$, and $\dot{\mathbf{X}}_s = \begin{bmatrix} \dot{x} & \dot{y} & \dot{z} & \dot{\alpha} & \dot{\beta} & \dot{\gamma} \end{bmatrix}^T$.

Therefore, Eqn. (A.1) can be written in following form

$$\dot{\mathbf{q}} = \mathbf{J}_s \mathbf{D} \dot{\mathbf{X}}_c = \mathbf{J}_c \dot{\mathbf{X}}_c \tag{A.4}$$

where $\mathbf{J}_c = \mathbf{J}_s \mathbf{D}$ is the modified velocity Jacobian which can be written in the following partial derivative forms:

$$\dot{q}_i = \sum_{j=1}^{6} \frac{\partial q_i}{\partial c_j} \dot{c}_j, \; i = 1, 2, 3, 4 \tag{A.5}$$

where $\frac{\partial q_i}{\partial c_j}$ are elements in $\mathbf{J}_c$.

Next, we have to find the relationship between the Newton-Raphson Jacobian $\mathbf{J}_f$ and the modified velocity Jacobian $\mathbf{J}_c$. By comparing between the time derivatives of Eqn. (2.8), and Eqn. (2.6), we can obtain the following relationship [42]

$$\frac{\partial f_i}{\partial c_j} = 2 q_i \frac{\partial q_i}{\partial c_j} \tag{A.6}$$

where $\frac{\partial f_i}{\partial c_j}$ are elements in $\mathbf{J}_f$.

Since $\dot{x}$ and $\dot{\gamma}$ are zeros from the kinematic constraint, we can construct a square Newton-Raphson matrix as

$$\mathbf{J}_f = \begin{bmatrix} \frac{\partial f_1}{\partial c_1} & \cdots & \frac{\partial f_1}{\partial c_4} \\ \vdots & \ddots & \vdots \\ \frac{\partial f_4}{\partial c_1} & \cdots & \frac{\partial f_4}{\partial c_4} \end{bmatrix} = \begin{bmatrix} 2q_1 \frac{\partial q_1}{\partial c_1} & \cdots & 2q_1 \frac{\partial q_1}{\partial c_4} \\ \vdots & \ddots & \vdots \\ 2q_4 \frac{\partial q_4}{\partial c_1} & \cdots & 2q_4 \frac{\partial q_4}{\partial c_4} \end{bmatrix} \tag{A.7}$$

where we define $(c_1, c_2, c_3, c_4) = (y, z, \alpha, \beta)$.

Appendix B: Screw Theory

A twist of a rigid body with respect to an inertial frame $\{O_a\}$, ${}^a\$_t$, can be written in the Plücker's ray coordinate form [86]:

$$ {}^a\$_t = \begin{bmatrix} {}^a\mathbf{v}_a \\ {}^a\boldsymbol{\omega} \end{bmatrix} = \omega \begin{bmatrix} {}^a\mathbf{r}_{a,t} \times {}^a\mathbf{s}_t + h_t {}^a\mathbf{s}_t \\ {}^a\mathbf{s}_t \end{bmatrix} = \omega \begin{bmatrix} {}^a\mathbf{s}_{a,t} \\ {}^a\mathbf{s}_t \end{bmatrix} = \omega \, {}^a\hat{\$}_t. \tag{B.1} $$

Dually, the force and moment applied on the rigid body can be described as a wrench ${}^a\$_w$ in the Plücker's axis coordinate form:

$$ {}^a\$_w = \begin{bmatrix} {}^a\mathbf{f} \\ {}^a\mathbf{m}_a \end{bmatrix} = f \begin{bmatrix} {}^a\mathbf{s}_w \\ {}^a\mathbf{r}_{a,w} \times {}^a\mathbf{s}_w + h_w {}^a\mathbf{s}_w \end{bmatrix} = f \begin{bmatrix} {}^a\mathbf{s}_w \\ {}^a\mathbf{s}_{a,w} \end{bmatrix} = f \, {}^a\hat{\$}_w, \tag{B.2} $$

where ${}^a\mathbf{r}_{a,t}$ and ${}^a\mathbf{r}_{a,w}$ denote arbitrary position vectors from the origin of $\{O_a\}$ to the screw axes (with respect to the same coordinate frame); ${}^a\mathbf{s}_t$ and ${}^a\mathbf{s}_w$ are unit vectors in direction of the screw axes; h_t and h_w are the pitches of the screws; ω and f are positive scalar twist and wrench intensities; ${}^a\hat{\$}_t = \begin{bmatrix} {}^a\mathbf{s}_{a,t}^T & {}^a\mathbf{s}_t^T \end{bmatrix}^T$ and ${}^a\hat{\$}_w = \begin{bmatrix} {}^a\mathbf{s}_w^T & {}^a\mathbf{s}_{a,w}^T \end{bmatrix}^T$ denote the unit screws of the twist and the wrench, respectively. The pitch of the screw is $h = \frac{{}^a\mathbf{s} \cdot {}^a\mathbf{s}_a}{{}^a\mathbf{s} \cdot {}^a\mathbf{s}}$, and the perpendicular vector from the origin to the screw axis is ${}^a_{\perp}\mathbf{r}_a = \frac{{}^a\mathbf{s} \times {}^a\mathbf{s}_a}{{}^a\mathbf{s} \cdot {}^a\mathbf{s}}$, where ${}^a\mathbf{s} \cdot {}^a\mathbf{s} = 1$.

In special case of a zero-pitch screw ($h = 0$) or a line vector, the rigid body is undergoing pure rotation, or a pure force is applied on it along the line axis. In the case of an infinite-pitch screw ($h = \infty$) or a free vector, the rigid body is undergoing a pure translation, or a pure couple moment is being applied on it. The unit screws of infinite pitch are ${}^a_{\infty}\hat{\$}_t = \begin{bmatrix} {}^a_{\infty}\mathbf{s}_t^T & 0 \end{bmatrix}^T$ and ${}^a_{\infty}\hat{\$}_w = \begin{bmatrix} 0 & {}^a_{\infty}\mathbf{s}_w^T \end{bmatrix}^T$, where ${}^a_{\infty}\mathbf{s}_t$ and ${}^a_{\infty}\mathbf{s}_w$ are in free vector directions of the linear velocity and the couple moment, respectively.

The reciprocal product of two screws represents the power developed from a wrench acting on a rigid body undergoing a twist [87]. From (B.1) and (B.2), the reciprocal power of two general screws can be written as follows [88]:

$$\begin{aligned} {}^{a}\$_{w} \circ {}^{a}\$_{t} &= {}^{a}\$_{w}^{T}\,{}^{a}\$_{t} \\ &= {}^{a}\mathbf{f} \cdot {}^{a}\mathbf{v}_{a} + {}^{a}\mathbf{m}_{a} \cdot {}^{a}\boldsymbol{\omega} \\ &= f\omega \left[(h_t + h_w)\,({}^{a}\mathbf{s}_{w} \cdot {}^{a}\mathbf{s}_{t}) + \left({}^{a}\mathbf{r}_{a,t} - {}^{a}\mathbf{r}_{a,w}\right) \cdot ({}^{a}\mathbf{s}_{t} \times {}^{a}\mathbf{s}_{w}) \right] \\ &= f\omega\, \tilde{w}, \end{aligned} \tag{B.3}$$

where $\tilde{w}$ is defined as the virtual coefficient or the reciprocal product of a unit wrench and a unit twist $\tilde{w} = {}^{a}\hat{\$}_{w} \circ {}^{a}\hat{\$}_{t}$. The reciprocal product of two screws is frame and origin independent. If a wrench does not produce any power on the rigid body undergoing a twist $\left({}^{a}\hat{\$}_{w} \circ {}^{a}\hat{\$}_{t} = 0\right)$, it means that the wrench and the twist are "reciprocal" to each other.

The reciprocity conditions among the zero-pitch and infinite-pitch screws can be geometrically observed in the main three cases:

1. Two zero-pitch screws are coplanar;
2. The axes of a zero-pitch screw and an infinite pitch screw are perpendicular to each other, and
3. Both are infinite pitch screws.

Appendix C: Transmission Indices

The transmission indices of a f-DOF fully-actuated non-redundant parallel mechanism determine how close each of the singularities conditions are. A zero value indicates the singularities.

1. Input Transmission Index (ITI): power transmitted from the actuator along each limb

$$\eta_{in} = \min_i \left\{ \frac{\left| \hat{\$}_{w,ra,i} \circ \hat{\$}_{t,a,i} \right|}{\left| \hat{\$}_{w,ra,i} \circ \hat{\$}_{t,a,i} \right|_{max}} \right\}, i = 1, 2, ..., f \tag{C.1}$$

2. Output Transmission Index (OTI): power transmitted from the actuator to the platform/end-effector twist

$$\eta_{out} = \min_i \left\{ \frac{\left| \hat{\$}_{w,ra,i} \circ \hat{\$}_{t,rp,i} \right|}{\left| \hat{\$}_{w,ra,i} \circ \hat{\$}_{t,rp,i} \right|_{max}} \right\}, i = 1, 2, ..., f \tag{C.2}$$

3. Constraint Transmission Index (CTI): structural rigidity (virtual power from limb constraints)

$$\eta_{const} = \min_j \left\{ \frac{\left| \hat{\$}_{w,c,j} \circ \hat{\$}_{t,rc,j} \right|}{\left| \hat{\$}_{w,c,j} \circ \hat{\$}_{t,rc,j} \right|_{max}} \right\}, j = 1, 2, ..., 6 - f \tag{C.3}$$

where $\left| \hat{\$}_w \circ \hat{\$}_t \right|_{max}$ is the maximum virtual coefficient, which characterizes the effects of corresponding transmission wrench and output twist screws [79]:

$$\begin{aligned} \left| \hat{\$}_w \circ \hat{\$}_t \right|_{max} &= \sqrt{(h_t + h_w)^2 + d_{max}^2}, \\ d_{max} &= \max \{d_{Cw}, d_{Ct}\}. \end{aligned} \tag{C.4}$$

where d_{Cw} is transmission characteristic length, the distance of a normal vector from a point in the twist screw to a point on the wrench screw that is closest to the so-called "centroid" A of the joint

connecting the corresponding limb with the platform, while output characteristic length, d_{Ct} is the distance of a normal vector from a point in the wrench screw to the point on the twist screw that is closest to the same joint centroid, defined as

$$\begin{aligned} d_{Cw} &= \left\| \mathbf{s}_t \times \left(\mathbf{p}_t - \mathbf{p}_w + (\mathbf{p}_w - \mathbf{a})^T \mathbf{s}_w \mathbf{s}_w \right) \right\|, \\ d_{Ct} &= \left\| \mathbf{s}_w \times \left(\mathbf{p}_w - \mathbf{p}_t + (\mathbf{p}_t - \mathbf{a})^T \mathbf{s}_t \mathbf{s}_t \right) \right\|. \end{aligned} \tag{C.5}$$

where $\mathbf{p}_w = \mathbf{s}_w \times \mathbf{s}_{o,w}$, $\mathbf{p}_t = \mathbf{s}_t \times \mathbf{s}_{o,t}$, and $\mathbf{a}$ is the position vector of the application point A of the actual leg. In our case of the pelvic WRAPS system, $\mathbf{a}$ is the spherical/universal joint center position on the moving platform. Note that if one of the pitches (h_t or h_w) is infinite, all other terms in (C.4) can be neglected and $\left| \hat{\$}_w \circ \hat{\$}_t \right|_{max}$ is equal to that pitch.